UNIVERSITY OF MESSINA

Department of Chemical, Biological, Pharmaceutical and Environmental Sciences

Doctoral Course in
Advanced Catalytic Processes for using Renewable Energy Sources (ACCESS)

NEW CONCEPT 3D-HIERARCHICAL NANOSTRUCTURED ELECTRODES FOR THE CONVERSION OF SMALL MOLECULES

PhD thesis of:

LUANA DE PASQUALE

Supervisors:

Prof. Gabriele Centi

Prof. Chiara Genovese

The coordinator of the Doctoral Course:

Prof. Gabriele Centi

Academic Year 2022-2023- XXXVI cycle

S.S.D. CHIM-04

To my father

Index

Abstract

To achieve net-zero emissions targets, a substantial shift away from fossil fuels to renewable energy-based systems is necessary. The development of innovative one-step catalytic routes for directly manufacturing chemicals and fuels, starting from small molecules such as H_2O, N_2, and CH_4, predominantly through sustainable photo-, electro-, and plasma-catalysis, is a strategy to achieve this goal. The challenge involves direct electrification to produce chemicals, fuels, and energy vectors, laying the groundwork for future carbon-neutral chemical production.

In this context, the primary objective of this work carried out in the framework of the ERC SCOPE project (Surface-COnfined fast-modulated Plasma for process and Energy intensification in small molecules conversion), was to design an efficient (photo) electrode to be used in various unconventional catalytic processes for the conversion of small molecules. Starting from one of the most widely used photoactive materials, novel photocatalysts based on an ordered array of TiO_2 nanotubes on a Ti mesh as support (TiO_2NTs/Ti mesh), eventually modified with different metal nanoparticles, have been efficiently developed. These materials, with novel 3D-type structural characteristics, combining a mesoporous structure (due to the ordered arrays of TiO_2 nanotubes) with the macro pores of a mesh, guarantee good light harvesting and fast charge transport so improving the photoactivity in the photo (electro)catalytic processes (i.e. water splitting and ethanol photo dehydrogenation). Additionally, the combination of this macro/meso nanostructured catalyst (based on TiO_2NTs/Ti mesh) with non-thermal plasma, has been evaluated to investigate the role of the potential synergy between plasma and (photo)catalysis in enhancing overall process efficiency.

Most of the research activities were carried out at the laboratory CASPE/INSTM (Laboratory of Catalysis for Sustainable Production and Energy) of the University of Messina (Dept. Chibiofaram). During the second year, six months were spent at the Department of Chemical Engineering and Chemistry at the Eindhoven University of Technology (Netherlands), under the supervision of Prof. Fausto Gallucci and Dr. Sirui Li, in the research group on Sustainable Process Engineering,

The Ph.D. thesis is organized into four main chapters, plus the general conclusions.

Chapter 1 explores the general implications and strategies employed to convert small molecules, analysing the latest developments in electro-, photo--, and plasma-catalysis routes, as innovative catalytic technologies implemented thus far. Additionally, attention is given to the main photoactive materials and their potential modifications.

Chapter 2 focuses on the experimental techniques employed to synthesize a hierarchical 3D macro-mesoporous structure based on highly ordered arrays of TiO_2 nanotubes (NTs) on a Ti mesh, to overcome the main drawbacks of titanium dioxide materials, i.e. the fast charge carriers recombination rate and the large band gap. The chapter provides a comprehensive analysis of the morphological, optical, and photo-electric characteristics of the catalysts. Using electrochemical impedance spectroscopy (EIS), the photoactivity associated with 3D or 2D geometries of the support, with both dark and illuminated conditions, is determined. This study demonstrates the existing correlation between the photoactivity and the specific charge transfer resistances which, in turn, led to a better comprehension of the electronic properties of TiO_2 nanotubes. The 3D structure of the nanotubes in the mesh, enhancing light absorption and facilitating faster electron transport along the nanotubes, significantly influences the catalytic

performance under illumination increasing the production of H_2 and current density in water photo-electrolysis.

Chapter 3 deals with the functionalization of the titania nanotubes on Ti mesh with metal nanoparticles with proven LSPR (localized surface plasmon resonance) behaviour (Au, Ag, Cu, Pd).

The different deposition procedures are described, followed by an extensive characterization. The effect of the metal on the performances in two different key H_2 production reactions (water photo-electrolysis and ethanol photo-dehydrogenation) is discussed. For the ethanol photo-conversion process, two different configurations of the cell, gas-phase, and liquid-phase, are employed, to investigate how gas-phase conditions can influence the performances in terms of productivity and selectivity. The results obtained show a notable enhancement in the performances of the metal-modified electrodes compared to the unmodified titanium dioxide substrate in the water photo-electrolysis reaction. In the ethanol photo-conversion process, the nature of the metal and the presence of an electrolyte influence the type and quantity of products formed at the anode. No acetic acid formation was observed in the gas phase by using an Au-modified TiO_2 catalyst, compared to Pd and Ag catalysts, (as opposed to the liquid phase configuration). The results obtained show that, a distinct reaction and, consequently, different selectivity, can be obtained by only varying cell configurations.

Finally, chapter 4 investigates the effect of the combination between TiO_2NTs/Ti mesh with non-thermal plasma in the reaction of non-oxidative coupling of methane (NOCM). The TiO_2NTs/Ti catalysts (also modified with metal nanoparticles) were tested in two different reactors: a conventional tubular DBD (dielectric barrier discharge) plasma reactor and a planar DBD reactor. In addition, the effect of light irradiation was investigated. A photoactive material TiO_2, can, in general, be excited by external light radiation to generate localized

charges on the surface which, positively interacting with the radicals generated in plasma, may increase the selectivity. A porous meso/macro 3D hierarchical structure, as the titanium dioxide nanotubes on a titanium mesh, increases both conversion and changes selectivity, and the integration of metal plasmonic NPs further enhances the performances. In particular, the gold-modified sample strongly improves the methane conversion in the DBD planar reactor, with a modulation also in the selectivity pushing towards the ethylene production, and this effect is more marked under light irradiation.

1. Introduction

1.1. Conversion of small molecules: a literature survey

The depletion of natural resources is driving up the need for efficient and sustainable manufacturing of fine chemicals[1]. One way to address this demand is through the development of new catalytic processes, which can facilitate the targeted and efficient conversion of fossil and biorenewable feedstocks with reduced energy consumption and environmental impact[2,3]. Considering these premises, the conversion of abundant small molecules, such as CO_2, H_2O, CH_4, and N_2, in value-added products is a fundamental aspect of contemporary chemistry and a prerequisite for the creation of useful substances, fuels, and materials[4–7]. Recent developments cover a wide spectrum of catalytic processes and reactions, that will be shortly described.

Because of its direct relationship to energy and environmental implications, catalytic conversion of one-carbon (C1) molecules such as CO, CO_2, and CH_4, into fuels and valuable compounds has recently received a lot of interest[5, 8–12].

Methane, for instance, is not just a popular source of renewable energy today, but also a C1 building block to produce chemicals[9]. Because of its availability and its relatively low cost, the production of compounds from methane has attracted a lot of interest in both the academic and the industrial worlds[8, 13]. Various processes, such as oxidative and non-oxidative coupling, pyrolysis, steam reforming, and biologically mediated processes, have been explored to convert methane into higher-value products, including hydrogen, syngas, and liquid fuels[14–17]. For example, using oxidative coupling of methane (OCM) is possible for the direct conversion of methane into ethylene and ethane, while with non-oxidative coupling of methane (NOCM), higher-chain hydrocarbons can be obtained without involving oxygen[14, 18–20]. Catalysts, generally based on transition metals,

have an important role in all these processes, favouring the breakage of methane's C-H bonds, generating ethylene and other valuable hydrocarbons through controlled carbon-carbon bond formation, offering a promising avenue for efficient methane conversion[21]. Steam reforming, a widely employed industrial process, utilizes methane to produce hydrogen and carbon monoxide[22]. Additionally, biological methane conversion through microbial processes and anaerobic digestion holds promise for sustainable and environmentally friendly methane utilization[23]. The industrial processes briefly described above, which involve one-step methane conversion, require harsh operating conditions, such as high temperatures and pressures, because of the stability of methane [5, 24]. Hence the need to improve and develop new catalytic routes for the conversion of methane, less expensive and less energy-intensive, involving for instance plasma catalysis, electro-catalysis, and photo-catalysis [25].

Another important C1 molecule catalytic conversion process is the carbon dioxide reduction reaction (CO_2RR) to carbonaceous compounds[26]. As part of an integrated CO_2 capture and utilization strategy, the reduction of carbon dioxide into synthetic fuels using electricity, light, or a combination of both is an effective and valuable method to decrease CO_2 emissions[27, 28].

Electroreduction emerges as an advantageous route to CO_2 conversion, due to its operation at room temperature and atmospheric pressure, and the simplicity of functionality and modularity distinguishes it from the chemical combustion processes[26]. The electrocatalytic reduction of CO_2 yields various products, such as formic acid, carbon monoxide, methanol, ethanol, ethylene, methane, acetic and oxalic acid[29]. However, challenges including low faradaic efficiencies, high overpotentials, slow kinetics, and electrocatalyst instability persist, with product distribution contingent on reaction conditions and electrocatalyst characteristics[30]. CO_2 photoreduction uses solar radiation to convert CO_2 into valuable compounds, mirroring the natural photosynthesis process in green plants[31]. Initial studies utilized Ru and Re-based complexes for homogenous

catalysis, primarily yielding formate and CO[32, 33]. Subsequent studies used oxide semiconductors (e.g., TiO_2, $SrTiO_3$, WO_3) and metal sulfides in the presence of water as heterogeneous catalysts[34].

Photo-electroreduction combines electroreduction and photoreduction approaches, yielding several advantages: i) reduced electrical consumption through lowered solar-powered voltage; ii) more effective charge separation under external voltage compared to photocatalysis; iii) prevention of product reoxidation via two separate reaction half-cells. Both photoreduction and photo-electroreduction show promise in converting CO_2 into organic compounds and artificial fuels using sunlight[35–37]. The products of this reaction might be used as alternative fuel sources and/or raw materials in industrial operations that previously relied on fossil fuels or photosynthetic products. Furthermore, since CO_2 reduction is a thermodynamically uphill process, it is also a useful energy storage technique[31, 38]. However, catalytic performances are low due to the difficulty in activating CO_2, the competition with water reduction for H_2 formation, and the complexity of products formed (requiring advanced detection technologies).

The electrolysis of water, consisting of the decomposition of water (H_2O) into its constituent gases, hydrogen (H_2) and oxygen (O_2), has received a lot of interest as an environmentally friendly source of hydrogen[39, 40]. This process is typically carried out in a water electrolyzer in which an electrical current is applied to split water molecules at the anode, producing oxygen, and at the cathode, yielding hydrogen [41]. Catalysts, often composed of precious metals like platinum or alternative materials such as nickel-based alloys, play a crucial role in accelerating the reaction rates, enhancing efficiency, and making the process economically viable[42]. The photo-electrochemical water splitting combines the electrochemical system described above with a semiconductor that can absorb sunlight and facilitate the reaction directly[35]. This approach has the potential to harness solar

energy and convert it into storable chemical fuels, addressing the intermittency of solar power.

Another route to produce hydrogen, using a relatively small molecule as a precursor, is ethanol reforming. Wood, straw, and even domestic garbage may all be profitably transformed into bioethanol[43]. Bioethanol reforming could be a way to produce hydrogen from low-value biomass materials[44, 45]. In particular, photo-reforming of ethanol produces H_2 at ambient pressure and room temperature with photoactive materials, thus it may be one of the most promising prospective among the reforming methods[46, 47]. These two important reactions for H_2 production (water splitting and ethanol photo-reforming) will be described in the next paragraphs more in detail.

Ammonia is a crucial component of fertilizers made primarily through the Haber-Bosch process, involving the reaction of nitrogen and hydrogen over an iron-based catalyst at pressures of up to 300 bar and temperatures close to 500°C[48]. Globally, there will likely be a significant rise in the demand for ammonia production due to the wide range of goods and applications that use it, as well as the growing interest in using it as an energy storage medium[49]. This is pushing the creation of less energy-intensive and more commercially feasible ammonia manufacturing alternatives, such as electro-catalytic and plasma catalytic routes[50–52].

1.2. Unconventional catalytic processes for small molecules conversion

To produce global fuels and chemicals from small molecules, in a sustainable, fossil-free way, four main sustainable catalytic approaches are emerging, schematized in Figure 1.1: photocatalysis, electrocatalysis, photo-electrocatalysis, and plasma catalysis[53]. While in use for many years on laboratory

scale, the interest in the scale-up of these technologies has increased lately[3]. The term "reactive" catalysis distinguishes photo-, electro-, and plasma-catalysis from conventional heterogeneous catalysis, which is categorized as "thermal" due to the role of heat in supplying the energy needed to overcome the activation energy barrier[54]. In contrast, "reactive" catalysis utilizes highly reactive species which could be generated by using renewable energy sources.

Although photo- electro-, and plasma catalysis are conceptually different, they share some mechanical similarities. The unifying factor of these catalytic technologies is the generation of highly reactive charged species on the catalyst surface[55]. In photocatalysis this process is accessible via charge separation induced by light or in-situ photogenerated electrical currents[56–58]; in electrocatalysis, it is the application of an electric potential that generates the reactive species, often with the integration of a photoactive element (e.g., photo-electrocatalysis)[59–62]; and in plasma catalysis these charged reactive species are generated by the interaction of the plasma-generated excited electrons, molecules, ions and radicals in the gas phase with the catalyst surface[63–68]. These in-situ produced reactants are fundamental in the reaction process, controlling both reactivity and selectivity and minimizing unfavourable side reactions. Additionally, they might cause the surface characteristics of the catalyst to vary dynamically[69].

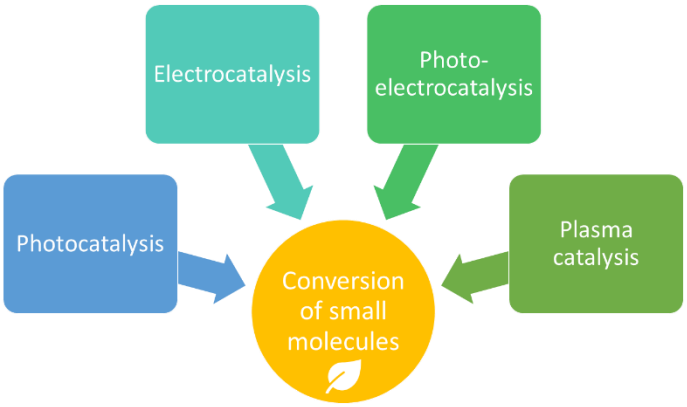

Figure 1.1 *Diagram of the different catalytic approaches for the conversion of small molecules*

A brief overview of the principles on which these technologies are based will be described in the next paragraphs.

1.2.1. Photocatalytic conversion processes

Photocatalysis is an important field in sustainable chemistry, with great potential in various environmental, energy, and industrial applications and even in organic synthesis[57, 70, 71]. A photocatalytic process involves the acceleration of a chemical reaction by the use of light energy and a photocatalyst, typically a semiconductor material. This kind of material exhibits strong oxidative and reductive properties, which play an important role in numerous chemical reactions[70]. More details about the photoactive materials will be reported in the par. 1.3.

The irradiation with light with an equal (or higher) energy than the band gap energy of the semiconductor material, causes the excitation of the electrons from the semiconductor valence band (VB) to the conduction band (CB), generating holes in the VB[72]. These electrons (e^-) and holes (h^+) are the charge carriers that take part in the oxidation and reduction reactions on the surface of the material,

generating highly reactive species, for example, hydroxyl radicals or superoxide ions[73] (see Figure 1.2).

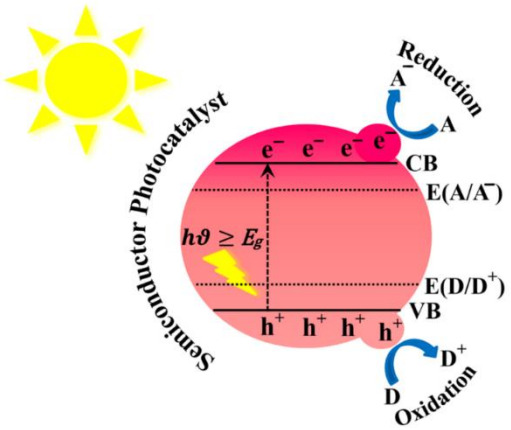

Figure 1.2 *Scheme of the mechanism of a general photocatalytic process. Reproduced with permission from ref.* [72]

In environmental applications, photocatalysis is useful for the purification of water, treatment of wastewater, and decomposition of pollutants in industrial settings, contributing to cleaner water and air[47, 70, 71]. Furthermore, photocatalysis plays a key role in the field of solar energy conversion of hydrocarbons (as already briefly described in the previous paragraphs) contributing significantly to the pursuit of renewable energy technologies [41, 74, 75]. The conversion of CO_2 into valuable chemicals and fuels through photocatalysis presents an environmentally friendly and energy-efficient alternative. This application is particularly crucial for addressing climate change and advancing a circular carbon economy. Researchers explored diverse photocatalytic materials, from metal oxides like titanium dioxide and zinc oxide to organic-inorganic hybrid perovskites, aiming to enhance the efficiency and selectivity of CO_2 reduction reactions[76–78]. This field holds great potential to change chemical and fuel production, steering industries toward more energy-efficient practices.

1.2.2. Electro and photo-electrocatalytic conversion processes

Electrocatalysis is the field of electrochemistry that deals with the catalysis of redox reactions and involves the acceleration of electrochemical reactions by using catalysts, known as electrocatalysts, to lower the energy barriers and facilitate the conversion of electrical energy into chemical energy and vice versa. These catalysts modify the kinetics of reactions by either enhancing the adsorption of reactants or providing alternative reaction pathways, thereby reducing the overpotential required for the reaction.

The interest in this topic has grown since the eighties, particularly in energy conversion and storage applications[53, 79]. The developed technologies based on electrocatalysis, such as fuel cells, electrolyzers, and batteries, displayed in Figure 1.3, have contributed significantly to the development of sustainable energy solutions [80].

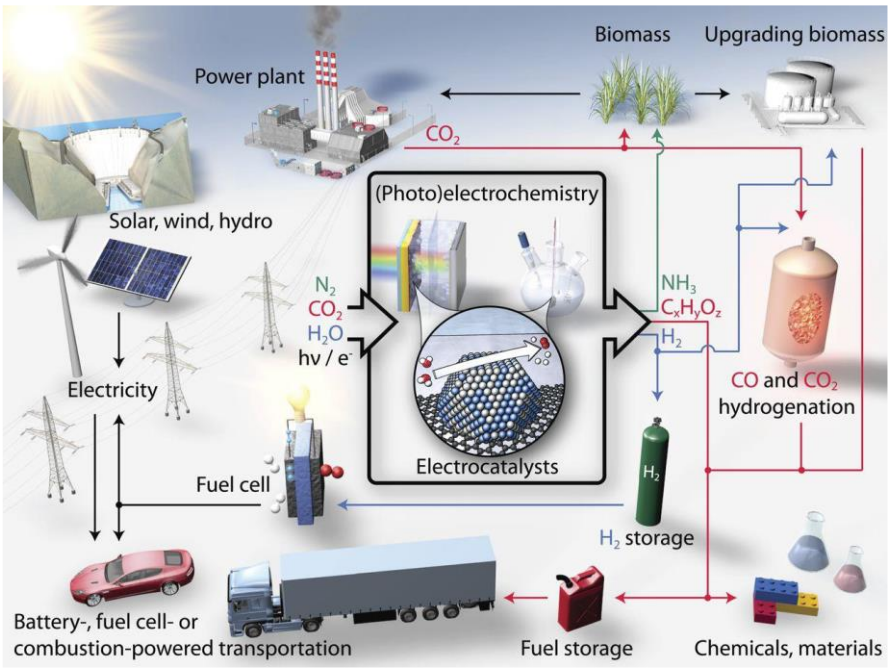

Figure 1.3 *Electrocatalysis-based sustainable energy landscape diagram, reproduced with permission from ref.*[38]

One of the prominent applications of electrocatalysis is in fuel cells, where it aids in the conversion of chemical energy, typically hydrogen, into electricity. Electrocatalysts, like platinum-based materials, play a vital role in promoting the oxygen reduction reaction (ORR) and hydrogen oxidation reaction (HOR) within the fuel cell electrodes, thus optimizing cell efficiency[80]. Moreover, electrocatalysis is fundamental in water electrolysis[81] for hydrogen production and energy storage. Specifically, electrocatalysts in water electrolysis help reduce the energy required for splitting water molecules, facilitating the production of clean hydrogen fuel. In energy storage devices like batteries and supercapacitors, electrocatalysis also contributes significantly[80]. Efficient electrocatalysts enhance the charge/discharge rates and overall performance of these devices, improving their energy density and cycle life. Furthermore, the field of electrocatalysis is evolving rapidly with the exploration of non-precious metal-based catalysts. Research is being conducted to find alternative materials that can potentially replace expensive and rare metals, such as platinum and iridium, while maintaining or even enhancing catalytic performance[82, 83].

Photo-electrocatalytic (PEC) conversion, which consists of the combination of photocatalysis and electrocatalysis (see Figure 1.4), offers a promising pathway to drive sustainable chemical reactions and fuel generation using solar energy[46]. This approach involves integrating photoactive materials with an electrochemical system, (with two or three electrodes, depending on whether a reference electrode is used or not) to allow the simultaneous capture of photons and efficient electron transfer and facilitate chemical transformations[26, 84]. The ability to separate the photoanode and cathode by a selective membrane is a fundamental convenience provided by a PEC cell. In fact, as a result of the separation, the oxidation and reduction products may be collected separately and this reduces, if not eliminates, product crossing, and significantly increases efficiency. The separation also provides the opportunity to investigate the two half-reactions independently.

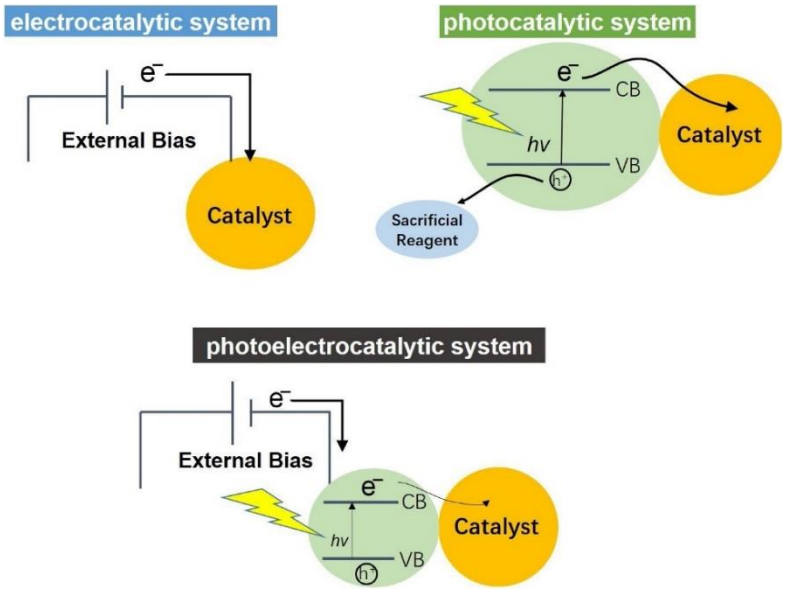

Figure 1.4 *Diagrams of electron sources and catalysts in electrocatalytic, photocatalytic, and photo-electrocatalytic systems* [31]

One prominent application of photo-electrocatalysis is the (photo)-electrocatalytic water splitting. A brief description of the most used devices for this reaction will be given below.

1.2.2.1. Electrolyzers

An electrolyzer is a device that uses electrical energy to split water or other feedstocks in their constituent element through electrolysis. In the case of water-splitting, the electrolyzer uses electricity to produce hydrogen and oxygen gases.

Electrolyzers could be classified as batch, semi-batch, and flow-type electrolyzers.

H-type Electrolyzers

The H-type cell electrolyzer, schematized in Figure 1.5, is a batch or semi-batch cell. The configuration consists of two half-cells divided by an ion exchange membrane, indicated as PEM (proton exchange membrane), and three electrodes: working, counter, and reference electrodes (Figure 1.5). The half-cells are

separated by the membrane to reduce the mixing of the anodic and cathodic products, avoid short circuits, keep the local pH, and allow the transport of protons or anions. The limitations include the large distance between the electrodes, which causes low energetic efficiency and challenges in scalability for large-scale industrial applications[85].

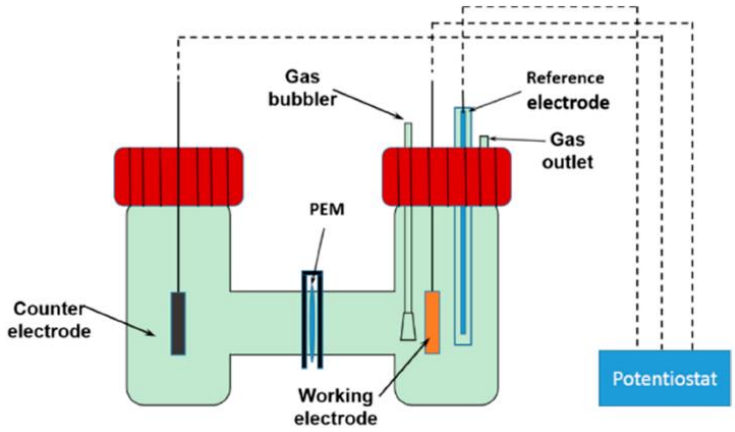

Figure 1.5 *Schematics of an H-type cell. Reproduced with permission of ref.*[86]

Flow-Cell Electrolyzers

This kind of electrolyzer utilizes a flow-through design where reactants continuously flow through porous electrodes, improving mass transport and efficiency compared to H-type cell[85]. They can operate in both acidic and alkaline environments, providing flexibility in electrolyte selection. Suited for grid-scale energy storage applications due to continuous operation, modularity, and adaptability to variable renewable energy inputs.

PEC electrolyzers

PEC electrolyzers integrate photoactive materials with traditional electrolysis processes. In this way, they combine principles of photocatalysis and electrochemistry to harness solar energy for water splitting and have the potential for direct solar-to-chemical conversion but face challenges in material stability,

efficiency, and specialized component requirements. Practically, the semiconductor materials act as photoanodes, absorbing sunlight and initiating the water-splitting reaction. These setups mimic natural photosynthesis by utilizing photoelectrons generated by the photocatalyst to drive redox reactions. Essentially, they function as an extension of electrochemical devices with the added feature of light as an energy source. A photo-electrochemical (PEC) system, like the example illustrated in Figure 1.6, comprises a photoelectrode, an electrolyte, a membrane, and an electrocatalyst (or another photoelectrode)[87]. PEC systems for water-splitting have evolved since their inception in 1968[88], considering factors like light source, reactor materials, mixing, heat exchange, and operation mode for optimal performance. Various PEC configurations, including photoanode-driven, photocathode-driven, and Z-scheme cells, are employed. However, PEC systems can be more intricate, incorporating one or two photoelectrodes, being biased or unbiased, and integrating an external photovoltaic cell for additional voltage.

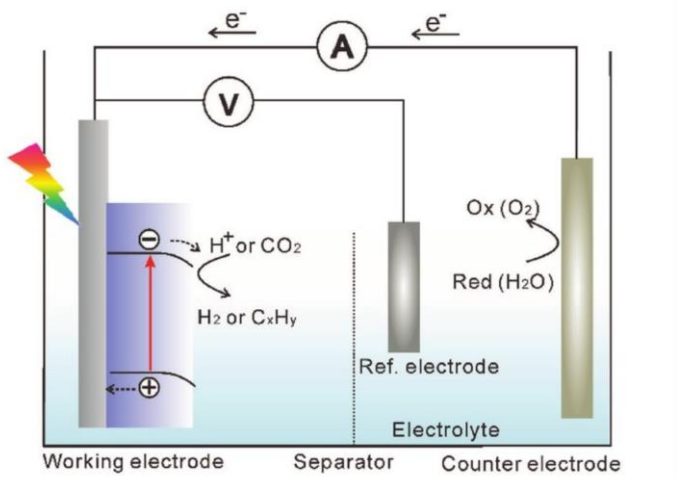

Figure 1.6 *An example of a photo-electrochemical cell. The working electrode is a photocathode. Reproduced with permission from ref.*[89]

Below will be given details about two fundamental light-assisted H_2 production reactions performed in PEC cells: water splitting and ethanol photo-conversion.

1.2.2.2. Water splitting in PEC cells

Water splitting in photo-electrochemical (PEC) cells involves the use of sunlight to drive the decomposition of water into hydrogen and oxygen through electrochemical reactions. PEC cells emulate the principles of natural photosynthesis, using semiconductor materials as photoelectrodes that absorb solar energy and initiate water-splitting reactions. At the core of a PEC system is the photoelectrode, typically composed of a semiconductor material that possesses suitable bandgaps for light absorption and also has to match the potentials of the redox couples involved in the reaction. In particular for water-splitting, the level of the valence band has to be above the redox potential of the O_2/H_2O couple, +1.2 eV vs. SHE, and the level of the conduction band has to be below the redox potential of the couple H^+/H_2, 0 eV. In Figure 1.7 the band gap energies of different materials compared to the redox potentials for water splitting are reported. Titanium dioxide, given its wide band gap, appears to be an optimal photocatalyst for this purpose[90].

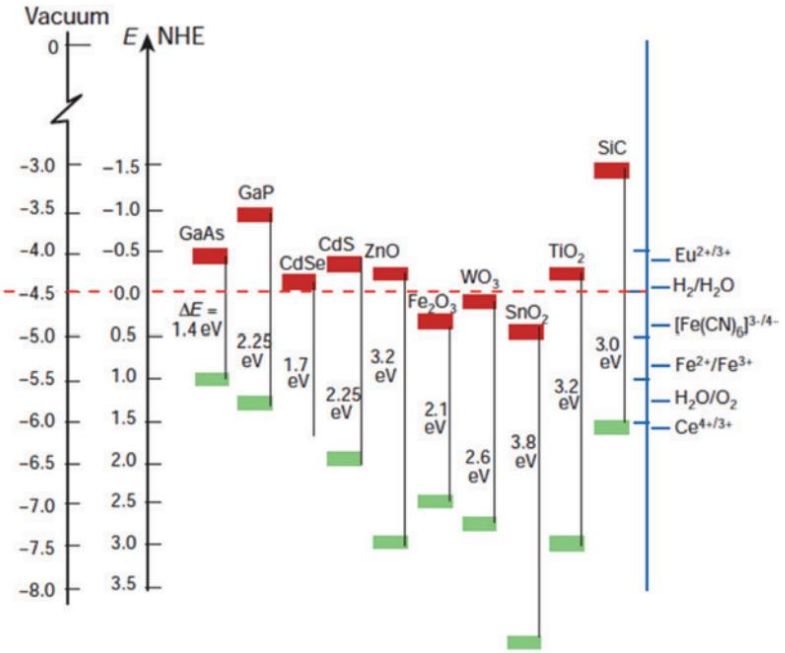

Figure 1.7 *Comparison between the band structure of different semiconductors and the redox potential of water splitting. Reproduced with permission from ref.*[90]

The mechanism of the photo-electrocatalytic water splitting is shown in Figure 1.8. The process begins with the absorption of photons by the semiconductor, causing the formation of electrons-holes pairs. After the diffusion of the charge carriers to the surface of the catalyst, the excited electrons reduce water at the cathode to produce hydrogen gas (H_2), while the holes oxidize water at the anode to release oxygen gas (O_2).

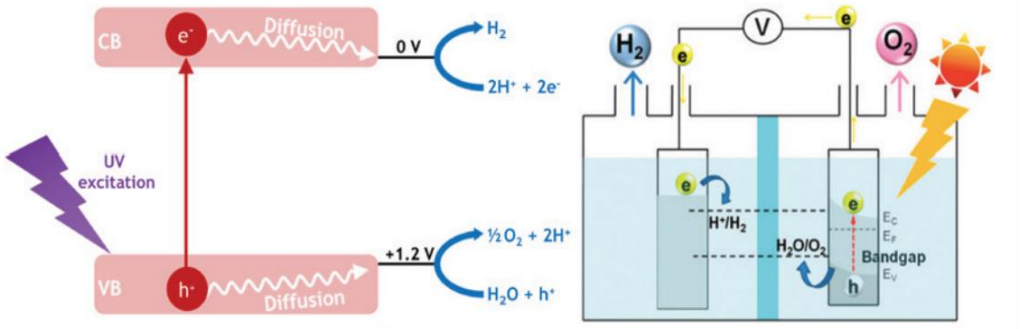

Figure 1.8 *Illustration of the main steps of the photo-electrocatalytic water-splitting. On the left the photogeneration of electron-hole pairs with the semi reactions which produce hydrogen* by *electrons and oxygen* by *holes. Reproduced with permission from* [90]

One of the key advantages of PEC water-splitting is its potential for direct solar-to-chemical conversion[41, 91] without the need for external electrical power.

This feature aligns with the broader goals of sustainable energy production and provides a clean and renewable source of hydrogen a versatile fuel with applications in fuel cells and various industrial processes [54]. However, several challenges must be addressed to optimize the efficiency and practicality of PEC water-splitting. One critical consideration is the choice of semiconductor material. The material must be stable under prolonged exposure to light and the harsh electrochemical conditions involved in water-splitting reactions[90, 92]. Additionally, the design of efficient and durable catalysts for the cathodic and anodic reactions is crucial to enhance the kinetics of water splitting. The configuration of PEC cells also plays an important role[46, 87]. Typically, a two-chamber system is employed, separating the reduction and oxidation reactions to prevent unwanted side reactions and enhance overall efficiency. Proton conductive membranes or anionic exchange membranes separate the two chambers, allowing for efficient transport of protons or anions between the anode and cathode.

1.2.2.3. Ethanol photo-conversion in PEC cells

A different approach for H_2 photoproduction is the addition of a small amount of an organic compound as a sacrificial agent for the hole sequestration that increases considerably hydrogen yield[93]. This single-step process that combines light-induced water splitting and photo-oxidation of biomass-derived organic compounds, is namely photo-reforming. Figure 1.9 shows the mechanism of biomass oxidation under aerobic conditions, with the organic substance ($C_xH_yO_z$) acting as an electron donor, generating CO_2 and H_2O through the reaction with the photo-generated holes. The electrons reduce H^+ to H_2, with hydrogen evolution.

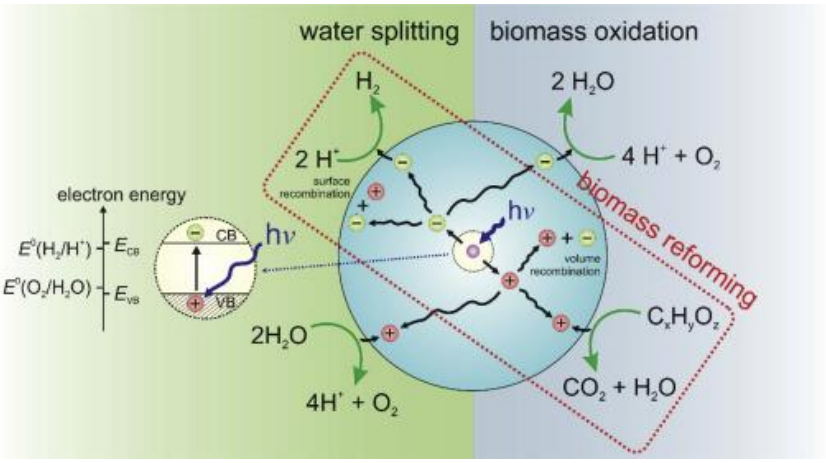

Figure 1.9 *Scheme of the reaction pathways following the irradiation of the semiconductor and the consequent excitation, on the left water-splitting reaction, on the right the biomass oxidation, and in the red rectangular section the photo-reforming. Reproduced with permission from ref.* [94]

In this context ethanol photoconversion in photo-electrochemical (PEC) cells represents a promising process in renewable energy research, for the possibility to use solar energy instead of thermo-catalytic conversion[93].

The field of ethanol photoconversion in PEC cells has seen significant advancements in recent years[44, 95–100]. Researchers have explored different semiconductor materials, novel catalysts, and improved system designs to enhance the performance of these cells. exploring the co-production of hydrogen and a valuable chemical through photoconversion, instead of carbon dioxide (as

in the photo-reforming), presents an attractive prospect with the potential to enhance process economics. A noteworthy reaction is the photocatalytic dehydrogenation of ethanol, which yields both H_2 and acetaldehyde, offering an alternative approach to ethanol photo-reforming[98]. This dual-product strategy not only has implications for the efficient utilization of resources but also introduces a valuable chemical product, such as acetaldehyde, thereby influencing the economic viability of the overall process. The presence of water, the choice of the catalysts, and the operative conditions, greatly influence the process[98].

By comparing ethanol photo-reforming and ethanol photo-dehydrogenation reactions, in terms of product value at real costs (assuming 100% selectivity in both reactions), it is possible to evidence that the ethanol photo-dehydrogenation holds an economic value of approximately 3.0-3.5 times greater than the ethanol photo-reforming, but selectivity and gas-phase operations are crucial factors to enable efficient product recovery and purification[98].

1.2.3. Plasma catalytic conversion processes

The plasma catalytic conversion of small molecules represents a dynamic and evolving field at the intersection of plasma science and catalysis, offering a promising path for sustainable chemical transformation[101–103]. The unique properties of plasma, such as the generation of reactive species and high energy, enable the activation of small molecules under mild conditions[104].

In general, exposing a gas to a significant potential difference between two electrodes can split the electrons in the gas molecules into ions and create a plasma. The plasma can be i) weakly ionized, resulting in a mixture of neutral atoms, molecules, ions, electrons, and radicals, or ii) fully ionized, in which case every species of neutral gas is entirely transformed into ions[105]. Based on their electron temperature, two types of weakly ionizing plasma can be distinguished: thermal and non-thermal plasmas (NTP). In thermal plasma, the bulk gas

molecules and electrons are in thermal equilibrium between 11600 K and 23200 K in temperature. In non-thermal plasmas, the high energy electrons (in the range of 1-10 eV) have a temperature significantly higher than that of bulk gas molecules, ions, and radicals[106, 107].

The most direct method for generating a non-thermal plasma involves the application of an external electric field between two electrodes situated within a gas volume. The minimum voltage necessary to ionize a gas, causing it to form a plasma discharge, is termed the breakdown voltage (V_b). Paschen's Law (Equation 1) describes the breakdown voltage and is influenced by both the distance between the electrodes (d) and the gas pressure (p)[108].

$$V_b = \frac{a(pd)}{\ln(pd) + b}$$

Equation 1

Here, 'a' represents the saturation ionization in the gas at a specific electric field/pressure (E/p) value, while 'b' is associated with the excitation and ionization energies. Both 'a' and 'b' are constants specific to the type of gas employed in the plasma generation process.

Non-thermal plasmas generally function at low pressures, ranging from 1 to 10^3 Pascal, or at atmospheric pressure. They consist of "cold" non-thermal discharges, including avalanches, Townsend streamers, and glow discharges. Reactors engineered for generating non-thermal plasmas are usually configured to prevent the occurrence of arc and spark discharges, as these events can cause plasma thermalization. The most commonly utilized NTPs are corona discharge, DBD (dielectric barrier discharge) and surface discharge, gliding arc plasma, microwave plasma, and electron beam irradiation plasma.

1.2.3.1. Dielectric barrier discharge (DBD) for plasma generation

Originally recognized as a silent discharge due to the absence of noisy spark formation, the dielectric barrier discharge (DBD) represents a non-thermal plasma

with versatile operation within a broad pressure range, from millibars up to atmospheric pressure. The DBD configuration usually comprises two electrodes and one or more dielectric layers, used to prevent flashover[105]. The materials employed for this purpose are quartz, ceramics, and materials characterized by a high breakdown strength and a low dielectric heating[109]. Figure 1.10 illustrates two common DBD configurations: on the left the planar configuration, in which the dielectric layer could be in contact with one electrode, with both electrodes or collocated in the middle between them; on the right the cylindrical configuration, in which the parts, electrodes and dielectric, are coaxial. The discharge gap, which is the distance between the electrodes, could be between 0.1 mm and several cm[109].

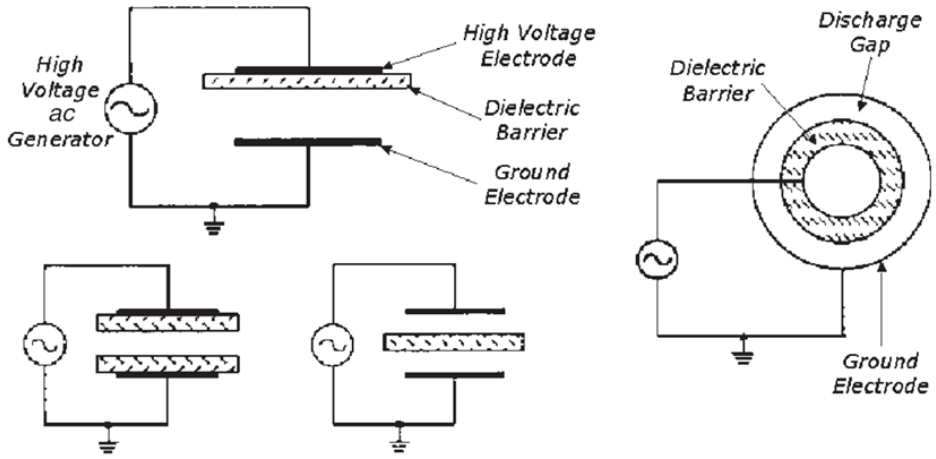

Figure 1.10 *Common DBD configuration, on the left planar DBD and the right cylindrical DBD. Reproduced with permission from ref.* [109]

The electrode system functions as a capacitor with an air gap, wherein the application of alternating current (AC) or pulsed voltages charges the capacitor. When the electric field strength surpasses the breakdown strength of the gap, a discharge occurs. The resulting plasma is non-uniform, comprising numerous micro discharges or filaments extending across the discharge gap and covering the insulating plate's entire surface. The charge accumulation on the plate's surface

restricts current flow, extinguishing the filaments and leaving a significant charge deposited on the surface in a few nanoseconds after breakdown. Reversing the polarity of the applied voltage increases the electric field across the gap, initiating discharge to equalize the voltage difference. Due to the rapidly changing electrode polarity, the breakdown voltage is reached during consecutive voltage half-waves, leading to microdischarges forming at a frequency twice that of the applied frequency (ranging from 50 Hz to 1 MHz). The brief duration of these discharges limits the transport of heavier charged particles, minimizing gas heating and classifying it as a non-thermal plasma (NTP)[105]. A substantial portion of the electron energy is utilized to excite gas atoms or molecules, initiating chemical reactions. Figure 1.11 illustrates an example of a DBD (dielectric barrier discharge) reactor with parallel plate electrodes. An example of an atmospheric plasma jet, or atmospheric pressure glow discharge, is depicted in Figure 1.11 b. It utilizes a concentric cylinder electrode system with high-voltage inner and outer electrodes. Either Ar or He serves as the feed gas and a DBD is generated in the nozzle. Energetic electrons excite feed gas molecules, and the resulting excited atoms are transported outside the electrode system through the nozzle, mixing with ambient air to produce a plasma jet.

Figure 1.11 c illustrates the surface discharge, a DBD configuration with two electrodes flanking an insulating plate. An AC voltage or pulse induces discharge along the edges of each electrode in the gas space above the plate, propagating along the surface.

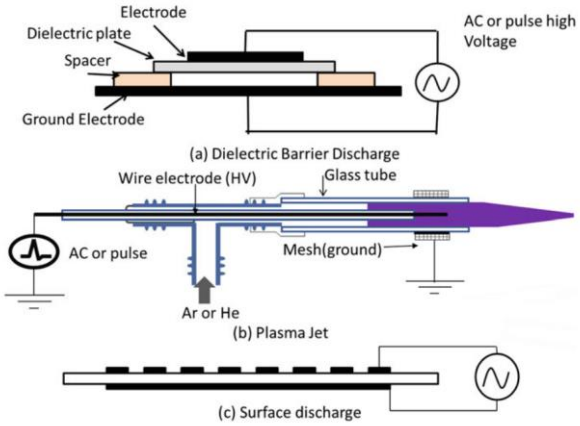

Figure 1.11 *Schematics of electrode configurations in* ***a)*** *dielectric barrier discharge,* ***b)*** *plasma jet, and* ***c)*** *surface discharge. Reproduced with permission from Ref.*[105]

1.2.3.2. Non-thermal plasma catalysis

The working mechanism of non-thermal plasma (NTP) in general allows the system to initiate chemical reactions of small molecules at low temperatures and pressures, making it energy-efficient and environmentally friendly, reducing energy consumption and enabling the treatment of thermally sensitive materials. Therefore, non-thermal plasma has emerged as a promising alternative to traditional catalysis. Because of the formation of several different species in non-thermal plasma, the desired product selectivity is rather low. For this reason, NTP is often used in conjunction with heterogeneous catalysts, to facilitate chemical reactions, and improve the selectivity and energetic efficiency[105, 110]. Figure 1.12 illustrates, for example, the enhanced methane and carbon dioxide conversion as the effect of the combination between plasma and catalysis[111].

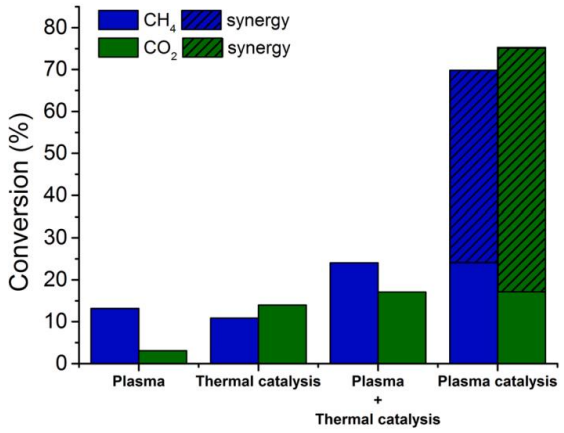

Figure 1.12 *Typical illustration of synergy in plasma catalysis: the conversion of CO_2 and CH_4 is greater in plasma catalysis than the total conversion of plasma and catalysis independently. Reproduced with permission from ref.* [111]

Plasma catalysis can operate in two modes: in-plasma catalysis (single-stage), where the catalyst is positioned inside the plasma, and post-plasma catalysis (two-stage), where the catalyst is situated after the plasma[111].

Many investigations have focused on in-plasma catalysis, particularly utilizing dielectric barrier discharge (DBD) plasmas. In this configuration, catalysts are commonly coated on dielectric beads, or catalyst powders are pelletized, with these beads or pellets, typically measuring 1–2 mm, filling the discharge gap. This arrangement allows reactive, short-lived plasma species to directly interact with the catalyst surface, maximizing the potential synergy between plasma and catalysis.

In-plasma catalysis is not feasible in warm plasma types, like gliding arc (GA), microwave (MW), atmospheric pressure glow discharge (APGD), and nanosecond (ns) pulsed plasmas. They are characterized by high temperatures, typically reaching several thousand Kelvin. Consequently, these warm plasmas are unsuitable for in-plasma processes because they could damage the catalysts, so the post-plasma configuration is more suitable in these cases[112]. For post-plasma catalysis, thermal catalysts might be appropriate, whereas in-plasma

catalysis requires materials different from typical thermal catalysts. Specifically, these materials should be tailored to the plasma composition to achieve synergistic effects.

Researchers are actively exploring the synergy between plasmas and catalytic materials, including metal oxides, zeolites, and nanoparticles, to achieve high selectivity and efficiency in various reactions. NTP offers a diverse range of applications, including air and water purification[113], VOC removal[114], and the conversion of small molecules, and it can often achieve high selectivity and efficiency in these processes[64].

The effect of the plasma on the catalysts and vice versa are summarized in Table 1.1.

Effects of catalysts on plasma

The presence of a catalyst in the discharge zone can modify the physical properties of the discharge. For example, introducing titanium dioxide pellets can modify the discharge from being a filamentary discharge to a combination of surface discharge on the pellets' surface and microdischarges between the pellets[115].

Another effect caused by the presence of a material in the plasma reactor, and also by the presence of porosity on the catalyst, is the electric field enhancement. This enhancement has a place in the contact point between the pellets and causes the modification of the electron energy distribution function, and so does the chemical composition of the plasma[115–117].

In a porous catalyst, the electric field inside the pores is very strong, which overall changes the plasma chemistry and generates microdischarges directly inside the pores, increasing the discharge per volume unit of the system and the discharge energy density and increasing the formation rates of certain ion species[117–121]. The dimensions of the pores also influence the stability of the microdischarges, with

the creation of stable microdischarges with pores with a diameter greater than 15 microns[120].

In the pollutants removal process, they must adsorb on the catalyst surface. In the presence of catalysts, it is proven that plasma has an increase in the removal efficiency, given by the increased retention time in the reactor and the increased probability of collisions between pollutants and reactive species[122, 123].

Effects of plasma on catalysts

The physicochemical properties of the catalyst may be affected by the non-thermal plasma discharge. The interaction with the discharge changes the electric surface properties of the catalyst, with the consequence of changing the adsorption-desorption equilibrium[123, 124]. Many studies have also reported surface changes after the plasma treatment, such as a decrease in the surface area of the catalyst or an increase in the number of vacancies[125, 126]. The oxidation state of the catalyst can also be affected by the plasma exposure[126, 127].

During plasma experiments, the inelastic collisions between the electrons and the molecules cause the gas temperature to rise, also raising the catalyst surface temperatures[128, 129]. However, this temperature rise is mild and does not thermally activate the catalysts but causes the formation of hot spots on the catalyst surface[130]. These hot spots can change the species distribution in the plasma[121].

The presence of vibrationally excited species in the plasma with a long lifetime can lower the activation barrier of catalyst surface reactions.

In certain conditions, it is reported that non-thermal plasma coupled with a titanium dioxide photocatalyst has higher oxidation efficiencies, stating that the UV light produced by nitrogen plasma discharges activates the photocatalyst[131–133]. Other studies demonstrated that the activation of the photocatalyst with external UV lamps and plasma results in a higher photocatalytic activity[134]. The

reason behind this phenomenon may be the presence of the plasma produced oxidizing species[135].

Catalysts on plasma effects	*Plasma on catalysts effects*
Change in discharge mode	Change in physicochemical properties of the catalyst
Electric field enhancement	Formation of hot spots
Formation of microdischarges inside catalyst pores	Lowering activation barriers
Production of reactive species	Changing the reaction pathways
Adsorption of pollutants	Activation by photon irradiation

Table 1.1 *Summary of the effects of the combination of plasma and catalysts. Adapted with permission from ref.*[117]

Three examples of relevant plasma-assisted catalytic processes are described below: CH_4 conversion, NH_3 synthesis and CO_2 conversion.

CH_4 conversion

Oxidative and non-oxidative coupling of methane through plasma catalysis represent two distinct pathways for the conversion of methane into value-added products. These processes are crucial for harnessing methane as a feedstock for chemical synthesis and reducing its environmental impact[25]. In oxidative coupling (OCM), methane reacts with oxygen or air in the presence of a catalyst, typically metal oxides such as lithium, sodium, or potassium oxides supported on various substrates [136]. The process results in the formation of higher hydrocarbons, primarily ethylene and ethane. OCM is an exothermic reaction and can be thermodynamically favourable, especially at higher temperatures. However, challenges include controlling selectivity to desired products and managing catalyst deactivation due to coke formation. Non-oxidative coupling (NOCM) occurs without the direct use of oxygen or air. This method is considered more environmentally friendly compared to OCM, as it minimizes carbon dioxide emissions. Plasma catalysis provides the necessary energy to break the strong C-

H bonds of methane and facilitates the activation of methane molecules at relatively mild conditions, producing larger hydrocarbons, so it offers several advantages in both OCM and NOCM[137]. Additionally, the non-equilibrium nature of the plasma enables better control over reaction pathways and product selectivity. Plasma catalysis offers advantages in avoiding coking and coke-related deactivation, minimizing the sintering of the catalysts, and providing alternative regeneration strategies where the plasma can remove coke deposits.

Another interesting process of methane conversion is the dry reforming of methane (DRM). In this context, achieving a high selectivity for the targeted products it's challenging, due to the diversified species formed. For this reason, the research is focused on the optimization of selectivity by the coupling of the catalyst or dielectric support and the plasma[138]. Generally, the primary products are syngas components (CO/H_2), but there is potential for the direct production of oxygenates or higher hydrocarbons[139, 141]. Despite having a lower energy efficiency compared to warm plasmas, DBD is a promising technology for plasma catalysis as it allows the integration of catalysts directly inside the plasma region, as explained previously. If catalysts can be designed to selectively produce oxygenates (or higher hydrocarbons), the lower energy efficiency could become more competitive with other non-plasma conversion technologies.

NH_3 synthesis

Research on ammonia synthesis has been predominantly conducted in DBD systems, the simplest type of plasma catalysis reactors, even though not the most energy efficient. Different catalysts are used, such as various metals and bimetallic catalysts on supports like Al_2O_3, MgO, SiO_2, $BaTiO_3$, and carbon-based materials, often in the form of powders, pellets, or spheres[142–145]. The best-reported results include an NH_3 yield of up to 9% and an energy cost as low as 1.5 MJ per mole NH_3 produced, although these record values were not from the same study or under identical conditions[142, 146]. Generally, energy costs below 20

MJ/mol have only been reported for very low yields (<<1%). When compared with typical values for the Haber–Bosch process, i.e., 15% NH_3 yield and 0.4 MJ/mol energy cost (for small-scale production compatible with renewable energy sources: ~10 tons/day), the energy cost of plasma catalysis must significantly decrease for industrial adoption, even factoring in the decreasing cost of renewable energy[142]. Energy costs in plasma catalysis reports typically neglect losses in the power supply, which can be as high as 50%. Accounting for these losses is crucial for a fair comparison. Still, existing plasma catalysis reports, are not yet competitive. Some research has been made to create an alternative for small-scale ammonia synthesis[147]. Small-scale plants have several advantages, such as easier installation and the local use of the produced ammonia, which reduces transportation costs[148].

CO_2 conversion

Considerable research has been conducted on the topic of CO_2 splitting, with emphasis not on specific product targets but rather on understanding how the catalyst influences the plasma and, consequently, CO_2 conversion and energy efficiency in dielectric barrier discharge (DBD) plasma systems[149]. For instance, some studies on CO_2 dissociation suggest that dielectric beads (catalyst supports) can significantly impact the plasma[150]. The dielectric constant plays a crucial role by inducing polarization in the beads, leading to electric field enhancements at contact points. This enhancement affects electron energy, influencing electron impact ionization, excitation, and dissociation reactions within the plasma. However, the dielectric constant is not the sole parameter influencing the plasma, as the performance trends do not precisely align with the dielectric constant. Therefore, the underlying mechanisms are more intricate[150].

Another study has demonstrated that a metallic foam electrode in a DBD plasma can notably improve CO_2 conversion and energy efficiency[151]. Consequently, plasma-catalytic CO_2 splitting serves as a valuable model reaction to gain a deeper

understanding of the effects of introducing catalysts, supports, or different metal electrodes into the plasma environment.

Plasma-catalytic CO_2 hydrogenation is also gaining increased attention due to the advantage of using low temperatures and atmospheric pressure conditions. Depending on the catalyst employed, this process can result in the formation of CO (reverse water-gas-shift reaction), CH_4 (methanation), or CH_3OH (methanol). Particularly, the formation of CH_3OH is intriguing. A study by Wang et al.[152] employed a DBD reactor packed with a Cu/Al_2O_3 catalyst, operating at 30 °C and 1 bar, reporting a CO_2 conversion of 21%, comparable to thermal catalysis. The maintenance of low temperature was achieved through a liquid-water ground electrode, promoting CH_3OH formation.

1.3. Photoactive materials

The definition provided by the International Union of Pure and Applied Chemistry (IUPAC) indicates a photocatalyst as a catalyst that induces chemical transformations between the reactants upon light absorption[153]. This light-driven process triggers the movement of charges across the photocatalyst/electrolyte interface, facilitating chemical reactions when the photocatalysts in a solution are illuminated as described in paragraph 1.2.1. The subsequent movements of these photogenerated charges involve the possibility of recombination, either within the photocatalyst or on its surfaces. A typical photocatalytic material often features a semiconductor (SC) surface, primarily composed of metal oxides such as titanium dioxide (TiO_2), zinc oxide (ZnO), or similar compounds.

In the band theory of solids, when the atoms form a solid, the discrete energy levels of the single atoms are perturbed by quantum effects and form two bands of energetic levels[154]. The valence band is occupied by all the solids electrons, and the conduction band is normally empty. Electrons may pass from the valence

band to the conduction band, as they do in single atoms. The band structure of a solid gives it particular electric characteristics. Generally, three distinct groups are defined: metals, insulators, and semiconductors, depending on their band's structures. In metals and semimetals (Figure 1.13 a, b, c), the valence band and conduction band overlap, causing the free movement of the electrons in the solids. These materials have a high conductivity. The insulator (Figure 1.13 e) has a high gap between the valence band and conduction band, and the electrons cannot be easily promoted to the conduction band, with negligible conductivity. The semiconductors (Figure 1.13 d and 1.14), instead, have a relatively low band gap and in certain circumstances the electrons can be promoted to the conduction band.

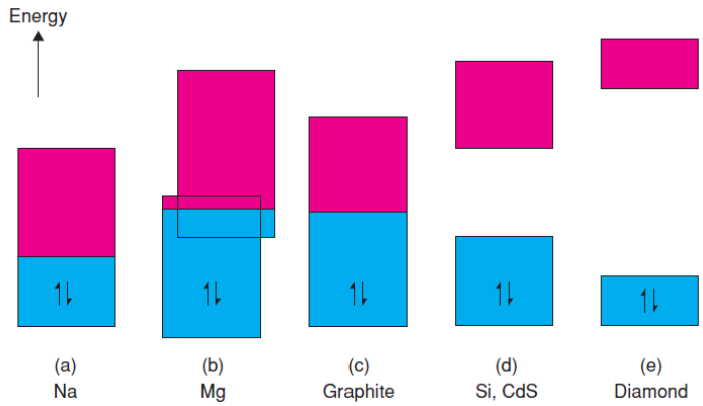

Figure 1.13 *Valence band and conduction band of different solids. In* ***(a)*** *and* ***(b)*** *metals, in* ***(c)*** *semimetal, in* ***(d)*** *semiconductor, and (e) insulator. Reproduced with permission from ref.*[154]

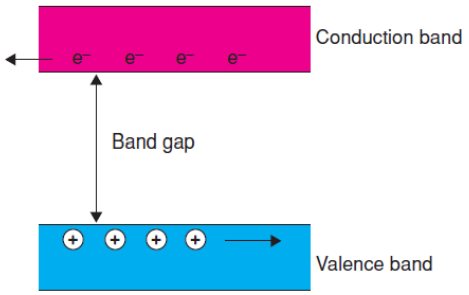

Figure 1.14 *Electronic configuration of a semiconductor. In blue is the valence band and in pink conduction band. Reproduced with permission from ref.* [154]

The energy gap between the valence and the conduction band is a forbidden gap, in which no electron energy levels are allowed.

When the semiconductor absorbs photons with an energy equal to or higher than the band gap energy, electrons are excited to a higher energy level in the conduction band (CB). The vacancy left by the electron is called a hole. Both electrons and holes are generated at the same time.

Semiconductors can be classified into extrinsic and intrinsic semiconductors: intrinsic semiconductors are pure semiconductors while extrinsic semiconductors need to be prepared by adding an impurity or dopant material.

Semiconductors can also be classified into two main categories: n-type (negative-type) and p-type (positive-type) semiconductors, each with distinct roles and characteristics described below.

n-type semiconductors have an excess of electrons as their majority charge carriers. Common examples include metal oxides like titanium dioxide (TiO_2), zinc oxide (ZnO), and tungsten trioxide (WO_3)[155]. n-type semiconductors are formed also by introducing impurities into a semiconductor, that can donate electrons to the conduction band (CB), bringing the Fermi level of the semiconductor closer to the CB. When an n-type semiconductor is immersed in an electrolyte, electrons flow from the semiconductor to the liquid if the redox potential closely aligns with the semiconductor's energy levels. This electron transfer continues until the Fermi levels reach equilibrium. Consequently, the semiconductor's Fermi level decreases, leading to a downward band shift that pushes holes towards the semiconductor/electrolyte interface (see Figure 1.15). This phenomenon explains why n-type semiconductors are often chosen for photo-oxidation reactions such as in water splitting.

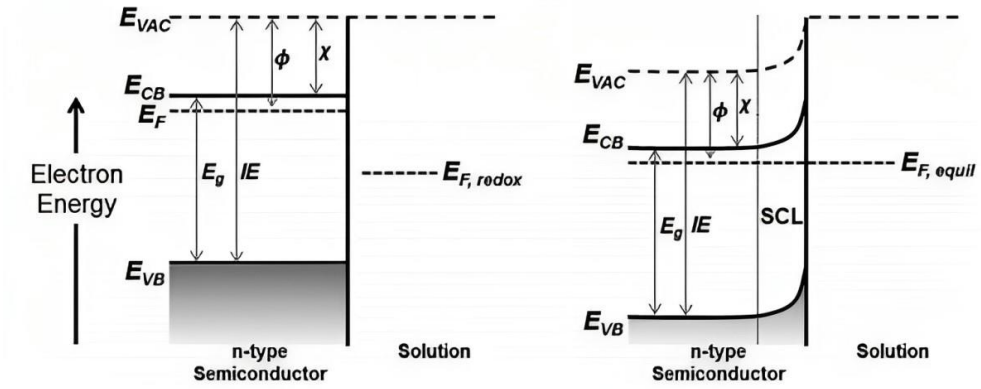

Figure 1.15 *n-type semiconductor band bending after being in contact with the electrolyte. Reproduced with permission from ref.*[156]

p-type semiconductors have an excess of positive charge carriers or "holes." Common examples include materials like copper(I) oxide (Cu_2O) and certain organic semiconductors. Through the introduction of impurities into a semiconductor is possible also to produce a p-type material which, by accepting electrons from the valence band (VB), leaves an excess of holes within the lattice. Essential characteristics of an ideal p-type semiconductor include chemical corrosion resistance, suitable band energy, efficient absorption in the visible solar spectrum, and a negatively positioned conduction band, crucial for overcoming kinetic limitations[157]. When a p-type semiconductor is immersed in an electrolyte, if the redox potential of the electrolyte falls within the semiconductor's energy band gap and differs from its Fermi level, electrons flow from the electrolyte to the semiconductor (see Figure 1.16.). This process increases the Fermi level until equilibrium is reached, creating a space-charge region near both sides of the semiconductor/electrolyte interface, identified as depletion and Helmholtz layers for the semiconductor and electrolyte sides, respectively. The Helmholtz layer comprises charge ions adsorbed on the semiconductor surface and results in a band bending effect, because the valence band (VB) and conduction band (CB) near the interface, bend upward. Although a difference is created due to the Helmholtz layer, it does not equal the Fermi level/redox potential difference. Due

to this phenomenon, p-type materials are typically employed as photocathodes (i.e. in water-splitting).

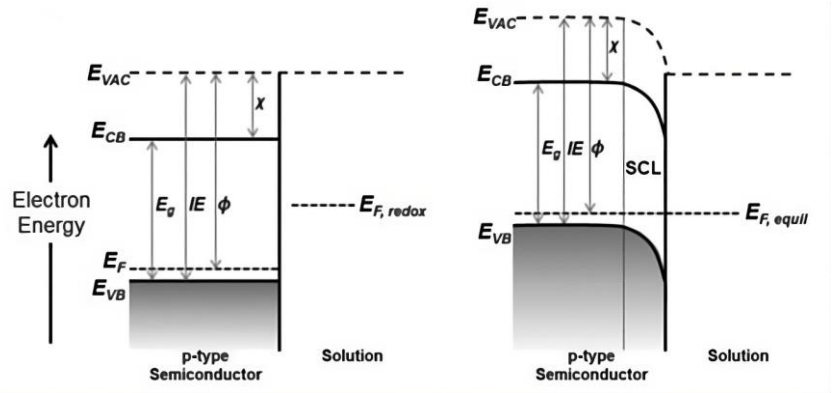

Figure 1.16 *p-type semiconductor band bending after being in contact with the electrolyte. Reproduced with permission from ref.*[156]

The combination of *n-type* and *p-type* materials in tandem configurations, known as tandem photo-electrochemical cells, is a promising approach to enhance overall efficiency[77].

Both *n-type* and *p-type* photo-electrocatalysts are integral components of photo-electrochemical cells, contributing to sustainable energy conversion processes. The challenge lies in finding and optimizing materials that exhibit desirable electronic properties, stability, and efficient charge separation. Additionally, integrating these materials into functional devices requires careful consideration of interfaces, band alignments, and overall system engineering.

Based on their composition and functionality, the photocatalysts come in different forms that may be used in a variety of applications such as environmental remediation, energy production, and organic synthesis[73, 75, 158]. In the following section, a brief description of the main types of materials used as photocatalysts is reported.

Metal Oxide Photocatalysts:

Metal oxide photocatalysts have emerged as a critical class of materials due to their ability to initiate and accelerate chemical reactions when exposed to light.

Titanium dioxide (TiO_2) is probably one of the most extensively studied metal oxide photocatalysts. Its wide bandgap energy enables it to be highly active in the ultraviolet (UV) region, facilitating the generation of electron-hole pairs upon light absorption. These charge carriers then engage in redox reactions, creating reactive oxygen species capable of breaking down organic pollutants, disinfecting water, and degrading volatile organic compounds present in the environment as described in detail in paragraph 1.2. However, its limited activity under visible light, because of its wide band gap energy, and the fast recombination rate of the charge carriers, has prompted extensive research to modify and enhance its performance[84].

Zinc oxide (ZnO), shares similarities with TiO_2 in terms of its photocatalytic properties with a similar ability to generate electron-hole pairs upon exposure to light, leading to its application in various fields, such as water treatment, air purification, and solar cells. Its high surface area, availability in various morphologies, and potential for visible light activity due to its narrower bandgap make it an attractive alternative to TiO_2 in certain applications[74].

Bismuth vanadate ($BiVO_4$) functions as an n-type semiconductor with a band gap energy (E_{bg} = 2.4 eV) lower than that of titania, enabling the absorption of visible light (wavelengths $\leq$ 515 nm) when utilized as a photoanode[159]. However, a significant drawback of this material lies in electron transport, leading to a high electron–hole pair recombination rate (between 60 and 80%) before reaching the interface. Moreover, thin $BiVO_4$ films lack the nanomorphology required for effective use as photoanodes in compact design PEC cells.

Tungsten trioxide (WO_3) is an optimal photocatalyst, due to its band gap energy varying from 2.5 to 3.0 eV, its low cost, and its stability in acidic and oxidative conditions[160]. Its main drawbacks are the fast recombination rate and the lower

conduction band edge with respect to the standard H^+/H_2 redox level, which modifies the material's fundamental[160]. It is used in many applications, such as sensors, photo-electrochemical water splitting, in dye-sensitized solar cells.

The nanomaterials derived from these semiconductors, such as nanoparticles, nanorods, nanosheets or nanotubes, display exceptional properties due to their nanoscale size that differ significantly from their bulk counterparts[74, 84, 161]. At the nanoscale, these materials often showcase quantum confinement effects and an increased surface-to-volume ratio, which enable them to absorb light and generate charge carriers efficiently. This is especially crucial in the context of photovoltaic devices and photocatalysis. These unique characteristics have sparked significant research interest, driving advancements in synthesis methods, including sol-gel processes, hydrothermal methods, anodic oxidation, and chemical vapour deposition techniques to control the size, shape, and properties of these nanomaterials[40, 74].

Carbon-Based Photocatalysts:

Carbon-based materials, such as graphitic carbon nitride (g-C_3N_4) and graphene-based materials, have garnered attention due to their capacity for visible light absorption, excellent stability, and environmental friendliness making them attractive candidates for diverse applications[162]. In graphitic carbon nitride (g-C_3N_4), the abundance of nitrogen atoms in this catalyst enhances its visible light absorption, contributing to its photocatalytic activity. Graphene, a single layer of carbon atoms arranged in a hexagonal lattice, has also emerged as a noteworthy carbon-based photoactive material, thanks to its high electrical conductivity, large surface area, and excellent electron mobility[163]. Functionalized graphene derivatives, such as graphene oxide (GO) and reduced graphene oxide (rGO), further expand the possibilities for tailoring their properties for enhanced performance in solar energy conversion. Carbon dots (CDs), which are carbon nanoparticles with sizes less than 10 nm, exhibit excellent photo-responsive

properties, including broad-spectrum light absorption and efficient photoluminescence[164]. These properties make CDs suitable for applications in solar cells, sensors, and imaging devices. Carbon-based materials like carbon nanotubes (CNTs) with their unique one-dimensional structure and excellent electrical conductivity, have been explored for enhancing charge transport in photovoltaic devices[165]. Porous carbon materials, due to their high surface area and tailored porosity, show promise in facilitating gas adsorption and catalytic reactions.

Hybrid and Composite Photocatalysts:

Despite their efficiency, ongoing research focuses on improving the photocatalytic performance of these materials by engineering their surface properties, doping with other elements, or developing novel hybrid materials.

Hybrid photocatalysts involve combinations of different materials or the integration of other elements, leading to synergistic effects that enhance catalytic activity.

In the paragraph below, an overview of the different modification methods is reported.

1.3.1 Materials modification

An effective photocatalyst should ideally possess three key characteristics simultaneously: i) efficient light absorption, particularly in the visible range, ii) strong photocatalytic activity, and iii) robust photo-corrosion stability[70]. Modification strategies aim to enhance the inherent limitations of these materials, such as their light absorption, charge separation, and catalytic activity.

Among the many strategies employed, the creation of heterojunctions, nanostructuring and the incorporation of nanoparticles, stand out as useful approaches.

Heterojunctions, formed by combining two different semiconductor materials, are a powerful modification strategy. The interface between these materials enables efficient charge separation and migration, critical processes for enhancing the performance of solar cells and photocatalytic systems. For instance, the creation of heterojunctions between titanium dioxide (TiO_2) and other semiconductors, such as zinc oxide (ZnO) or bismuth vanadate ($BiVO_4$), can significantly improve the efficiency of water splitting and pollutant degradation. The mismatch in energy levels at the heterojunction interface promotes the separation of photogenerated electron-hole pairs, preventing their recombination and promoting more effective charge utilization.

Different types of heterojunctions can be distinguished, depending on what kind of semiconductors, *n-type* or *p-type*, are coupled.

The isotype heterojunctions (n-n or p-p) are formed by coupling two different semiconductors of the same type. An example of n-n heterojunctions is TiO_2/ZnO, both *n-type* semiconductors.

The anisotype (n-p or p-n) is formed by the junction of two different types of semiconductor materials. An example could be the heterojunctions between TiO_2 and p-type silicon.

The alignment of the energy bands at the interface between the two materials affects the electric behaviour of the hybrid semiconductor.

Nanostructuration involves the deliberate design of materials at the nanoscale to exploit quantum effects and optimize their photoactive properties. This approach includes the creation of nanowire arrays, nanoporous structures, and hierarchical architectures. Nanostructured materials provide a large surface area for light

absorption and facilitate rapid charge transport. For instance, nanostructured photoanodes in dye-sensitized solar cells, enhance the light-harvesting capacity, resulting in improved photogenerated electron extraction and conversion efficiency. Similarly, nanoporous structures in photocatalysts, increase the exposure of active sites, promoting enhanced catalytic activity i.e. for water splitting and pollutant degradation. This approach to materials modification will be discussed further in Chapter 2.

Another prevalent strategy involves incorporating metal nanoparticles onto semiconductor surfaces.

Nanoparticles, with their unique size-dependent properties, favour efficient light absorption and charge separation, thereby pushing the overall performance of solar cells and photocatalytic materials. Additionally, the high surface area-to-volume ratio of nanoparticles provides more active sites for catalytic reactions, amplifying their effectiveness in photocatalysis.

Transition metals, such as Fe, Cr, Ni, V, Mn, and Cu are used for the modification of the photoactive material. A study on titanium dioxide doped with different transition metals proved the extension of the photoactivity of titania in the visible spectrum. Some of these metals can help to prevent the recombination of charge carriers[92]. In particular, Fe, Cu, and Ni can trap both electrons and holes, while Cr and Ni can trap just single charge carriers[92]. The decoration techniques commonly used are wet impregnation, sol-gel, and hydrothermal deposition.

Another possibility to increase absorption properties in the visible region and prevent undesirable charge recombination is the decoration with plasmonic nanoparticles like Au, Ag, Cu and Pd. The surface plasmonic resonance (SPR) effect can increase the energy intensity of the electrons resulting in an overall enhancement of the photocatalytic activity[166]. This particular and well-known effect will be described in detail in Chapter 3. The synergy achieved by combining these modifications, i.e. the incorporation of nanoparticles onto the surface of

nanostructured materials, often leads to remarkable improvements in photoactive material performance.

1.4. References

[1] I. Fechete, Y. Wang, and J. C. Védrine, “The past, present and future of heterogeneous catalysis,” *Catal Today*, vol. 189, no. 1, pp. 2–27, Jul. 2012, doi: 10.1016/j.cattod.2012.04.003.

[2] X. Liu, L. He, Y.-M. Liu, and Y. Cao, “Supported Gold Catalysis: From Small Molecule Activation to Green Chemical Synthesis,” *Acc Chem Res*, vol. 47, no. 3, pp. 793–804, Mar. 2014, doi: 10.1021/ar400165j.

[3] A. Bogaerts, G. Centi, V. Hessel, and E. Rebrov, “Challenges in unconventional catalysis,” *Catal Today*, vol. 420, p. 114180, Aug. 2023, doi: 10.1016/j.cattod.2023.114180.

[4] X. Sun, H. Chen, Y. Yin, M. T. Curnan, J. W. Han, Y. Chen, and Z. Ma, “Progress of Exsolved Metal Nanoparticles on Oxides as High Performance (Electro)Catalysts for the Conversion of Small Molecules,” *Small*, vol. 17, no. 10, Mar. 2021, doi: 10.1002/smll.202005383.

[5] B. Wang, S. Albarracín-Suazo, Y. Pagán-Torres, and E. Nikolla, “Advances in methane conversion processes,” *Catal Today*, vol. 285, pp. 147–158, May 2017, doi: 10.1016/j.cattod.2017.01.023.

[6] R. Lan, J. T. S. Irvine, and S. Tao, “Ammonia and related chemicals as potential indirect hydrogen storage materials,” *Int J Hydrogen Energy*, vol. 37, no. 2, pp. 1482–1494, Jan. 2012, doi: 10.1016/j.ijhydene.2011.10.004.

[7] H. Yin, Y. Dou, S. Chen, Z. Zhu, P. Liu, and H. Zhao, “2D Electrocatalysts for Converting Earth-Abundant Simple Molecules into Value-Added

Commodity Chemicals: Recent Progress and Perspectives," *Advanced Materials*, vol. 32, no. 18, May 2020, doi: 10.1002/adma.201904870.

[8] X. Meng, X. Cui, N. P. Rajan, L. Yu, D. Deng, and X. Bao, "Direct Methane Conversion under Mild Condition by Thermo-, Electro-, or Photocatalysis," *Chem*, vol. 5, no. 9, pp. 2296–2325, Sep. 2019, doi: 10.1016/j.chempr.2019.05.008.

[9] Y. Liu, D. Deng, and X. Bao, "Catalysis for Selected C1 Chemistry," *Chem*, vol. 6, no. 10, pp. 2497–2514, Oct. 2020, doi: 10.1016/j.chempr.2020.08.026.

[10] F. Zhang, Y.-H. Li, M.-Y. Qi, Y. M. A. Yamada, M. Anpo, Z.-R. Tang, and Y.-J. Xu, "Photothermal catalytic CO_2 reduction over nanomaterials," *Chem Catalysis*, vol. 1, no. 2, pp. 272–297, Jul. 2021, doi: 10.1016/j.checat.2021.01.003.

[11] H. Han, T. Han, Y. Luo, M. A. Mushtaq, Y. Jia, and C. Liu, "Recent advances in α-Fe_2O_3-based photocatalysts for CO_2 conversion to solar fuels," *Journal of Industrial and Engineering Chemistry*, vol. 128, pp. 81–94, Dec. 2023, doi: 10.1016/j.jiec.2023.07.064.

[12] T. Lu, T. Xu, S. Zhu, J. Li, J. Wang, H. Jin, X. Wang, J. Lv, Z. Wang, and S. Wang, "Electrocatalytic CO_2 Reduction to Ethylene: From Advanced Catalyst Design to Industrial Applications," *Advanced Materials*, vol. 35, no. 52, Dec. 2023, doi: 10.1002/adma.202310433.

[13] J. Xie, R. Jin, A. Li, Y. Bi, Q. Ruan, Y. Deng, Y. Zhang, S. Yao, G. Sankar, D. Ma, and J. Tang, "Highly selective oxidation of methane to methanol at ambient conditions by titanium dioxide-supported iron species," *Nat Catal*, vol. 1, no. 11, pp. 889–896, Nov. 2018, doi: 10.1038/s41929-018-0170-x.

[14] L. Sun, Y. Wang, N. Guan, and L. Li, “Methane Activation and Utilization: Current Status and Future Challenges,” *Energy Technology*, vol. 8, no. 8, Aug. 2020, doi: 10.1002/ente.201900826.

[15] S. Schneider, S. Bajohr, F. Graf, and T. Kolb, “State of the Art of Hydrogen Production via Pyrolysis of Natural Gas,” *ChemBioEng Reviews*, vol. 7, no. 5, pp. 150–158, Oct. 2020, doi: 10.1002/cben.202000014.

[16] H. Song, X. Meng, Z. Wang, H. Liu, and J. Ye, “Solar-Energy-Mediated Methane Conversion,” *Joule*, vol. 3, no. 7, pp. 1606–1636, Jul. 2019, doi: 10.1016/j.joule.2019.06.023.

[17] S. T. Wismann, J. S. Engbæk, S. B. Vendelbo, F. B. Bendixen, W. L. Eriksen, K. Aasberg-Petersen, C. Frandsen, I. Chorkendorff, and P. M. Mortensen, “Electrified methane reforming: A compact approach to greener industrial hydrogen production,” *Science (1979)*, vol. 364, no. 6442, pp. 756–759, May 2019, doi: 10.1126/science.aaw8775.

[18] T. Zhang, “Recent advances in heterogeneous catalysis for the nonoxidative conversion of methane,” *Chem Sci*, vol. 12, no. 38, pp. 12529–12545, 2021, doi: 10.1039/D1SC02105B.

[19] A. Cruellas, T. Melchiori, F. Gallucci, and M. van Sint Annaland, “Oxidative Coupling of Methane: A Comparison of Different Reactor Configurations,” *Energy Technology*, vol. 8, no. 8, Aug. 2020, doi: 10.1002/ente.201900148.

[20] Y. Xu, X. Bao, and L. Lin, “Direct conversion of methane under nonoxidative conditions,” *J Catal*, vol. 216, no. 1–2, pp. 386–395, May 2003, doi: 10.1016/S0021-9517(02)00124-0.

[21] P. Schwach, X. Pan, and X. Bao, “Direct Conversion of Methane to Value-Added Chemicals over Heterogeneous Catalysts: Challenges and

Prospects," *Chemical Reviews*, vol. 117, no. 13. American Chemical Society, pp. 8497–8520, Jul. 12, 2017. doi: 10.1021/acs.chemrev.6b00715.

[22] A. Iulianelli, S. Liguori, J. Wilcox, and A. Basile, "Advances on methane steam reforming to produce hydrogen through membrane reactors technology: A review," *Catalysis Reviews*, vol. 58, no. 1, pp. 1–35, Jan. 2016, doi: 10.1080/01614940.2015.1099882.

[23] J. D. Semrau, A. A. DiSpirito, and S. Yoon, "Methanotrophs and copper," *FEMS Microbiol Rev*, vol. 34, no. 4, pp. 496–531, Jul. 2010, doi: 10.1111/j.1574-6976.2010.00212.x.

[24] J. H. Lunsford, "Catalytic conversion of methane to more useful chemicals and fuels: a challenge for the 21st century," *Catal Today*, vol. 63, no. 2–4, pp. 165–174, Dec. 2000, doi: 10.1016/S0920-5861(00)00456-9.

[25] D. H. Lee, Y.-H. Song, K.-T. Kim, and J.-O. Lee, "Comparative Study of Methane Activation Process by Different Plasma Sources," *Plasma Chemistry and Plasma Processing*, vol. 33, no. 4, pp. 647–661, Aug. 2013, doi: 10.1007/s11090-013-9456-6.

[26] C. Ampelli, F. Tavella, D. Giusi, A. M. Ronsisvalle, S. Perathoner, and G. Centi, "Electrode and cell design for CO_2 reduction: A viewpoint," *Catal Today*, vol. 421, p. 114217, Sep. 2023, doi: 10.1016/j.cattod.2023.114217.

[27] C. Genovese, C. Ampelli, S. Perathoner, and G. Centi, "Electrocatalytic conversion of CO_2 to liquid fuels using nanocarbon-based electrodes," *Journal of Energy Chemistry*, vol. 22, no. 2, pp. 202–213, Mar. 2013, doi: 10.1016/S2095-4956(13)60026-1.

[28] G. Centi and S. Perathoner, "Catalytic Technologies for the Conversion and Reuse of CO_2," in *Handbook of Climate Change Mitigation and Adaptation*, Cham: Springer International Publishing, 2022, pp. 1803–1852. doi: 10.1007/978-3-030-72579-2_119.

[29] B. C. Marepally, C. Ampelli, C. Genovese, T. Saboo, S. Perathoner, F. M. Wisser, L. Veyre, J. Canivet, E. A. Quadrelli, and G. Centi, “Enhanced formation of >C1 Products in Electroreduction of CO_2 by Adding a CO_2 Adsorption Component to a Gas-Diffusion Layer-Type Catalytic Electrode,” *ChemSusChem*, vol. 10, no. 22, pp. 4442–4446, Nov. 2017, doi: 10.1002/cssc.201701506.

[30] C. Ampelli, C. Genovese, D. Cosio, S. Perathoner, and G. Centi, “Effect of Current Density on Product Distribution for the Electrocatalytic Reduction of CO_2,” *Chem Eng Trans*, vol. 74, pp. 1285–1290, 2019.

[31] Y. Wang, D. He, H. Chen, and D. Wang, “Catalysts in electro-, photo- and photoelectrocatalytic CO_2 reduction reactions,” *Journal of Photochemistry and Photobiology C: Photochemistry Reviews*, vol. 40, pp. 117–149, Sep. 2019, doi: 10.1016/j.jphotochemrev.2019.02.002.

[32] H. Ishida, “Electrochemical/Photochemical CO_2 Reduction Catalyzed by Transition Metal Complexes,” in *Carbon Dioxide Chemistry, Capture and Oil Recovery*, InTech, 2018. doi: 10.5772/intechopen.75199.

[33] H. Nasrallah, P. Lyu, G. Maurin, and M. El-Roz, “Highly efficient CO_2 reduction under visible-light on non-covalent Ru···Re assembled photocatalyst: Evidence on the electron transfer mechanism,” *J Catal*, vol. 404, pp. 46–55, Dec. 2021, doi: 10.1016/j.jcat.2021.09.007.

[34] W. A. Thompson, A. Olivo, D. Zanardo, G. Cruciani, F. Menegazzo, M. Signoretto, and M. M. Maroto-Valer, “Systematic study of TiO_2 /ZnO mixed metal oxides for CO_2 photoreduction,” *RSC Adv*, vol. 9, no. 38, pp. 21660–21666, 2019, doi: 10.1039/C9RA03435H.

[35] C. Ampelli, C. Genovese, F. Tavella, S. Perathoner, and G. Centi, “Nano-Engineered Electrodes for the Generation of Solar Fuels: Benefits and

Drawbacks of Adopting a Photo-Electrocatalytic (PECa) Approach," *Chem Eng Trans*, vol. 57, pp. 1597–1602, 2017.

[36] C. Ampelli, R. Passalacqua, C. Genovese, S. Perathoner, and G. Centi, "A Novel Photo-electrochemical Approach for the Chemical Recycling of Carbon Dioxide to Fuels," *Chem Eng Trans*, vol. 25, pp. 683–688, 2011.

[37] C. Ampelli, C. Genovese, G. Centi, R. Passalacqua, and S. Perathoner, "Nanoscale Engineering in the Development of Photoelectrocatalytic Cells for Producing Solar Fuels," *Top Catal*, vol. 59, no. 8–9, pp. 757–771, May 2016, doi: 10.1007/s11244-016-0547-5.

[38] Z. W. Seh, J. Kibsgaard, C. F. Dickens, I. Chorkendorff, J. K. Nørskov, and T. F. Jaramillo, "Combining theory and experiment in electrocatalysis: Insights into materials design," *Science (1979)*, vol. 355, no. 6321, Jan. 2017, doi: 10.1126/science.aad4998.

[39] Y. Jiao, Y. Zheng, M. Jaroniec, and S. Z. Qiao, "Design of electrocatalysts for oxygen- and hydrogen-involving energy conversion reactions," *Chem Soc Rev*, vol. 44, no. 8, pp. 2060–2086, 2015, doi: 10.1039/C4CS00470A.

[40] J. D. Benck, T. R. Hellstern, J. Kibsgaard, P. Chakthranont, and T. F. Jaramillo, "Catalyzing the Hydrogen Evolution Reaction (HER) with Molybdenum Sulfide Nanomaterials," *ACS Catal*, vol. 4, no. 11, pp. 3957–3971, Nov. 2014, doi: 10.1021/cs500923c.

[41] B. You and Y. Sun, "Innovative Strategies for Electrocatalytic Water Splitting," *Acc Chem Res*, vol. 51, no. 7, pp. 1571–1580, Jul. 2018, doi: 10.1021/acs.accounts.8b00002.

[42] X. Fang, Q. Shang, Y. Wang, L. Jiao, T. Yao, Y. Li, Q. Zhang, Y. Luo, and H. Jiang, "Single Pt Atoms Confined into a Metal–Organic Framework for Efficient Photocatalysis," *Advanced Materials*, vol. 30, no. 7, Feb. 2018, doi: 10.1002/adma.201705112.

[43] A. DEMIRBAS, “Progress and recent trends in biofuels,” *Prog Energy Combust Sci*, vol. 33, no. 1, pp. 1–18, Feb. 2007, doi: 10.1016/j.pecs.2006.06.001.

[44] T. Hou, S. Zhang, Y. Chen, D. Wang, and W. Cai, “Hydrogen production from ethanol reforming: Catalysts and reaction mechanism,” *Renewable and Sustainable Energy Reviews*, vol. 44, pp. 132–148, Apr. 2015, doi: 10.1016/j.rser.2014.12.023.

[45] T. Yamazaki, N. Kikuchi, M. Katoh, T. Hirose, H. Saito, T. Yoshikawa, and M. Wada, “Behavior of steam reforming reaction for bio-ethanol over Pt/ZrO_2 catalysts,” *Appl Catal B*, vol. 99, no. 1–2, pp. 81–88, Aug. 2010, doi: 10.1016/j.apcatb.2010.06.003.

[46] C. Ampelli, G. Centi, R. Passalacqua, and S. Perathoner, “Synthesis of solar fuels by a novel photoelectrocatalytic approach,” *Energy Environ Sci*, vol. 3, no. 3, p. 292, 2010, doi: 10.1039/b925470f.

[47] A. Gasparotto, D. Barreca, D. Bekermann, A. Devi, R. A. Fischer, P. Fornasiero, V. Gombac, O. I. Lebedev, C. Maccato, T. Montini, G. Van Tendeloo, and E. Tondello, “F-Doped Co_3O_4 Photocatalysts for Sustainable H_2 Generation from Water/Ethanol,” *J Am Chem Soc*, vol. 133, no. 48, pp. 19362–19365, Dec. 2011, doi: 10.1021/ja210078d.

[48] S. Giddey, S. P. S. Badwal, and A. Kulkarni, “Review of electrochemical ammonia production technologies and materials,” *Int J Hydrogen Energy*, vol. 38, no. 34, pp. 14576–14594, Nov. 2013, doi: 10.1016/j.ijhydene.2013.09.054.

[49] A. Valera-Medina, F. Amer-Hatem, A. K. Azad, I. C. Dedoussi, M. de Joannon, R. X. Fernandes, P. Glarborg, H. Hashemi, X. He, S. Mashruk, J. McGowan, C. Mounaim-Rouselle, A. Ortiz-Prado, A. Ortiz-Valera, I. Rossetti, B. Shu, M. Yehia, H. Xiao, and M. Costa, “Review on Ammonia

as a Potential Fuel: From Synthesis to Economics," *Energy & Fuels*, vol. 35, no. 9, pp. 6964–7029, May 2021, doi: 10.1021/acs.energyfuels.0c03685.

[50] S. Chen, S. Perathoner, C. Ampelli, C. Mebrahtu, D. Su, and G. Centi, "Electrocatalytic Synthesis of Ammonia at Room Temperature and Atmospheric Pressure from Water and Nitrogen on a Carbon-Nanotube-Based Electrocatalyst," *Angewandte Chemie International Edition*, vol. 56, no. 10, pp. 2699–2703, Mar. 2017, doi: 10.1002/anie.201609533.

[51] M. L. Carreon, "Plasma catalytic ammonia synthesis: state of the art and future directions," *J Phys D Appl Phys*, vol. 52, no. 48, p. 483001, Nov. 2019, doi: 10.1088/1361-6463/ab3b2c.

[52] F. Tavella, D. Giusi, and C. Ampelli, "Nitrogen reduction reaction to ammonia at ambient conditions: A short review analysis of the critical factors limiting electrocatalytic performance," *Curr Opin Green Sustain Chem*, vol. 35, p. 100604, Jun. 2022, doi: 10.1016/j.cogsc.2022.100604.

[53] S. Perathoner and G. Centi, "Catalysis for solar-driven chemistry: The role of electrocatalysis," *Catal Today*, vol. 330, pp. 157–170, Jun. 2019, doi: 10.1016/j.cattod.2018.03.005.

[54] G. Centi and S. Perathoner, "Catalysis for an electrified chemical production," *Catal Today*, vol. 423, p. 113935, Nov. 2023, doi: 10.1016/j.cattod.2022.10.017.

[55] J. Wordsworth, T. M. Benedetti, S. V. Somerville, W. Schuhmann, R. D. Tilley, and J. J. Gooding, "The Influence of Nanoconfinement on Electrocatalysis," *Angewandte Chemie International Edition*, vol. 61, no. 28, Jul. 2022, doi: 10.1002/anie.202200755.

[56] X. Sun, S. Jiang, H. Huang, H. Li, B. Jia, and T. Ma, “Solar Energy Catalysis,” *Angewandte Chemie International Edition*, vol. 61, no. 29, Jul. 2022, doi: 10.1002/anie.202204880.

[57] L. Candish, K. D. Collins, G. C. Cook, J. J. Douglas, A. Gómez-Suárez, A. Jolit, and S. Keess, “Photocatalysis in the Life Science Industry,” *Chem Rev*, vol. 122, no. 2, pp. 2907–2980, Jan. 2022, doi: 10.1021/acs.chemrev.1c00416.

[58] J. Z. Bloh and R. Marschall, “Heterogeneous Photoredox Catalysis: Reactions, Materials, and Reaction Engineering,” *European J Org Chem*, vol. 2017, no. 15, pp. 2085–2094, Apr. 2017, doi: 10.1002/ejoc.201601591.

[59] H. Li, C. Guo, J. Long, X. Fu, and J. Xiao, “Theoretical understanding of electrocatalysis beyond thermodynamic analysis,” *Chinese Journal of Catalysis*, vol. 43, no. 11, pp. 2746–2756, Nov. 2022, doi: 10.1016/S1872-2067(22)64090-7.

[60] G. Centi, G. Iaquaniello, and S. Perathoner, “Chemical engineering role in the use of renewable energy and alternative carbon sources in chemical production,” *BMC Chemical Engineering*, vol. 1, no. 1, p. 5, Dec. 2019, doi: 10.1186/s42480-019-0006-8.

[61] A. P. O’Mullane, M. Escudero-Escribano, I. E. L. Stephens, and K. Krischer, “The Role of Electrocatalysis in a Sustainable Future: From Renewable Energy Conversion and Storage to Emerging Reactions,” *ChemPhysChem*, vol. 20, no. 22, pp. 2900–2903, Nov. 2019, doi: 10.1002/cphc.201901058.

[62] Y. Pei, H. Zhong, and F. Jin, “A brief review of electrocatalytic reduction of CO_2—Materials, reaction conditions, and devices,” *Energy Sci Eng*, vol. 9, no. 7, pp. 1012–1032, Jul. 2021, doi: 10.1002/ese3.935.

[63] E. C. Neyts, K. (Ken) Ostrikov, M. K. Sunkara, and A. Bogaerts, “Plasma Catalysis: Synergistic Effects at the Nanoscale,” *Chem Rev*, vol. 115, no. 24, pp. 13408–13446, Dec. 2015, doi: 10.1021/acs.chemrev.5b00362.

[64] A. Bogaerts, X. Tu, J. C. Whitehead, G. Centi, L. Lefferts, O. Guaitella, F. Azzolina-Jury, H.-H. Kim, A. B. Murphy, W. F. Schneider, T. Nozaki, J. C. Hicks, A. Rousseau, F. Thevenet, A. Khacef, and M. Carreon, “The 2020 plasma catalysis roadmap,” *J Phys D Appl Phys*, vol. 53, no. 44, p. 443001, Oct. 2020, doi: 10.1088/1361-6463/ab9048.

[65] S. Liu, L. R. Winter, and J. G. Chen, “Review of Plasma-Assisted Catalysis for Selective Generation of Oxygenates from CO_2 and CH_4,” *ACS Catal*, vol. 10, no. 4, pp. 2855–2871, Feb. 2020, doi: 10.1021/acscatal.9b04811.

[66] P. Hinde, V. Demidyuk, A. Gkelios, and C. Tipton, “Plasma Catalysis: A Review of the Interdisciplinary Challenges Faced : Realising the potential of plasma catalysis on a commercial scale,” *Johnson Matthey Technology Review*, vol. 64, no. 2, pp. 138–147, Apr. 2020, doi: 10.1595/205651320X15759961130711.

[67] H. Puliyalil, D. Lašič Jurković, V. D. B. C. Dasireddy, and B. Likozar, “A review of plasma-assisted catalytic conversion of gaseous carbon dioxide and methane into value-added platform chemicals and fuels,” *RSC Adv*, vol. 8, no. 48, pp. 27481–27508, 2018, doi: 10.1039/C8RA03146K.

[68] J. C. Whitehead, “Plasma-catalysis: Is it just a question of scale?,” *Front Chem Sci Eng*, vol. 13, no. 2, pp. 264–273, Jun. 2019, doi: 10.1007/s11705-019-1794-3.

[69] C. Genovese, M. E. Schuster, E. K. Gibson, D. Gianolio, V. Posligua, R. Grau-Crespo, G. Cibin, P. P. Wells, D. Garai, V. Solokha, S. Krick Calderon, J. J. Velasco-Velez, C. Ampelli, S. Perathoner, G. Held, G. Centi, and R. Arrigo, “Operando spectroscopy study of the carbon dioxide

electro-reduction by iron species on nitrogen-doped carbon," *Nat Commun*, vol. 9, no. 1, p. 935, Mar. 2018, doi: 10.1038/s41467-018-03138-7.

[70] S. Zhu and D. Wang, "Photocatalysis: Basic Principles, Diverse Forms of Implementations and Emerging Scientific Opportunities," *Adv Energy Mater*, vol. 7, no. 23, Dec. 2017, doi: 10.1002/aenm.201700841.

[71] M. R. Hoffmann, S. T. Martin, W. Choi, and D. W. Bahnemann, "Environmental Applications of Semiconductor Photocatalysis," *Chem Rev*, vol. 95, no. 1, pp. 69–96, Jan. 1995, doi: 10.1021/cr00033a004.

[72] N. Goodarzi, Z. Ashrafi-Peyman, E. Khani, and A. Z. Moshfegh, "Recent Progress on Semiconductor Heterogeneous Photocatalysts in Clean Energy Production and Environmental Remediation," *Catalysts*, vol. 13, no. 7, p. 1102, Jul. 2023, doi: 10.3390/catal13071102.

[73] J.-R. Chen, X.-Q. Hu, L.-Q. Lu, and W.-J. Xiao, "Exploration of Visible-Light Photocatalysis in Heterocycle Synthesis and Functionalization: Reaction Design and Beyond," *Acc Chem Res*, vol. 49, no. 9, pp. 1911–1923, Sep. 2016, doi: 10.1021/acs.accounts.6b00254.

[74] C. B. Ong, L. Y. Ng, and A. W. Mohammad, "A review of ZnO nanoparticles as solar photocatalysts: Synthesis, mechanisms and applications," *Renewable and Sustainable Energy Reviews*, vol. 81, pp. 536–551, Jan. 2018, doi: 10.1016/j.rser.2017.08.020.

[75] H. Wang, X. Li, X. Zhao, C. Li, X. Song, P. Zhang, P. Huo, and X. Li, "A review on heterogeneous photocatalysis for environmental remediation: From semiconductors to modification strategies," *Chinese Journal of Catalysis*, vol. 43, no. 2, pp. 178–214, Feb. 2022, doi: 10.1016/S1872-2067(21)63910-4.

[76] D. Giusi, C. Ampelli, C. Genovese, S. Perathoner, and G. Centi, "A novel gas flow-through photocatalytic reactor based on copper-functionalized

nanomembranes for the photoreduction of CO_2 to C1-C2 carboxylic acids and C1-C3 alcohols," *Chemical Engineering Journal*, vol. 408, p. 127250, Mar. 2021, doi: 10.1016/j.cej.2020.127250.

[77] H. Deng, X. Fei, Y. Yang, J. Fan, J. Yu, B. Cheng, and L. Zhang, "S-scheme heterojunction based on p-type $ZnMn_2O_4$ and n-type ZnO with improved photocatalytic CO_2 reduction activity," *Chemical Engineering Journal*, vol. 409, p. 127377, Apr. 2021, doi: 10.1016/j.cej.2020.127377.

[78] S. Zeng, P. Kar, U. K. Thakur, and K. Shankar, "A review on photocatalytic CO_2 reduction using perovskite oxide nanomaterials," *Nanotechnology*, vol. 29, no. 5, p. 052001, Feb. 2018, doi: 10.1088/1361-6528/aa9fb1.

[79] C. Tang, Y. Zheng, M. Jaroniec, and S. Qiao, "Electrocatalytic Refinery for Sustainable Production of Fuels and Chemicals," *Angewandte Chemie International Edition*, vol. 60, no. 36, pp. 19572–19590, Sep. 2021, doi: 10.1002/anie.202101522.

[80] M. Winter and R. J. Brodd, "What Are Batteries, Fuel Cells, and Supercapacitors?," *Chem Rev*, vol. 104, no. 10, pp. 4245–4270, Oct. 2004, doi: 10.1021/cr020730k.

[81] A. Fujishima and K. Honda, "Electrochemical Photolysis of Water at a Semiconductor Electrode," *Nature*, vol. 238, no. 5358, pp. 37–38, Jul. 1972, doi: 10.1038/238037a0.

[82] M. Shao, Q. Chang, J.-P. Dodelet, and R. Chenitz, "Recent Advances in Electrocatalysts for Oxygen Reduction Reaction," *Chem Rev*, vol. 116, no. 6, pp. 3594–3657, Mar. 2016, doi: 10.1021/acs.chemrev.5b00462.

[83] W. T. Hong, M. Risch, K. A. Stoerzinger, A. Grimaud, J. Suntivich, and Y. Shao-Horn, "Toward the rational design of non-precious transition metal oxides for oxygen electrocatalysis," *Energy Environ Sci*, vol. 8, no. 5, pp. 1404–1427, 2015, doi: 10.1039/C4EE03869J.

[84] T. Saboo, F. Tavella, C. Ampelli, S. Perathoner, C. Genovese, B. C. Marepally, L. Veyre, E. A. Quadrelli, and G. Centi, “Water splitting on 3D-type meso/macro porous structured photoanodes based on Ti mesh,” *Solar Energy Materials and Solar Cells*, vol. 178, pp. 98–105, May 2018, doi: 10.1016/j.solmat.2018.01.007.

[85] D. Gao, P. Wei, H. Li, L. Lin, G. Wang, and X. Bao, “Designing Electrolyzers for Electrocatalytic CO_2 Reduction,” *Acta Physico Chimica Sinica*, vol. 0, no. 0, pp. 2009021–0, 2020, doi: 10.3866/PKU.WHXB202009021.

[86] X. Zhao, M. Du, and F. Liu, “Operando Synthesis of High-Curvature Copper Thin Films for CO_2 Electroreduction,” *Materials*, vol. 12, no. 4, p. 602, Feb. 2019, doi: 10.3390/ma12040602.

[87] C. Ampelli, C. Genovese, G. Centi, R. Passalacqua, and S. Perathoner, “Nanoscale Engineering in the Development of Photoelectrocatalytic Cells for Producing Solar Fuels,” *Top Catal*, vol. 59, no. 8–9, pp. 757–771, May 2016, doi: 10.1007/s11244-016-0547-5.

[88] P. J. Boddy, “Oxygen Evolution on Semiconducting TiO_2,” *J Electrochem Soc*, vol. 115, no. 2, p. 199, 1968, doi: 10.1149/1.2411080.

[89] J. Chen, C. Dong, H. Idriss, O. F. Mohammed, and O. M. Bakr, “Metal Halide Perovskites for Solar-to-Chemical Fuel Conversion,” *Adv Energy Mater*, vol. 10, no. 13, Apr. 2020, doi: 10.1002/aenm.201902433.

[90] A. Gellé and A. Moores, “Water splitting catalyzed by titanium dioxide decorated with plasmonic nanoparticles,” *Pure and Applied Chemistry*, vol. 89, no. 12, pp. 1817–1827, Nov. 2017, doi: 10.1515/pac-2017-0711.

[91] H. Eidsvåg, S. Bentouba, P. Vajeeston, S. Yohi, and D. Velauthapillai, “TiO_2 as a Photocatalyst for Water Splitting—An Experimental and

Theoretical Review," *Molecules*, vol. 26, no. 6, p. 1687, Mar. 2021, doi: 10.3390/molecules26061687.

[92] R. Dholam, N. Patel, M. Adami, and A. Miotello, "Hydrogen production by photocatalytic water-splitting using Cr- or Fe-doped TiO_2 composite thin films photocatalyst," *Int J Hydrogen Energy*, vol. 34, no. 13, pp. 5337–5346, Jul. 2009, doi: 10.1016/j.ijhydene.2009.05.011.

[93] A. V. Puga, "Photocatalytic production of hydrogen from biomass-derived feedstocks," *Coord Chem Rev*, vol. 315, pp. 1–66, May 2016, doi: 10.1016/j.ccr.2015.12.009.

[94] C.-W. Huang, B.-S. Nguyen, J. C.-S. Wu, and V.-H. Nguyen, "A current perspective for photocatalysis towards the hydrogen production from biomass-derived organic substances and water," *Int J Hydrogen Energy*, vol. 45, no. 36, pp. 18144–18159, Jul. 2020, doi: 10.1016/j.ijhydene.2019.08.121.

[95] D. Sannino, V. Vaiano, P. Ciambelli, M. C. Hidalgo, J. J. Murcia, and J. A. Navío, "Oxidative Dehydrogenation of Ethanol over Au/TiO_2 Photocatalysts," *Journal of Advanced Oxidation Technologies*, vol. 15, no. 2, Jan. 2012, doi: 10.1515/jaots-2012-0206.

[96] T. Reztsova, C.-H. Chang, J. Koresh, and H. Idriss, "Dark- and Photoreactions of Ethanol and Acetaldehyde over TiO_2/Carbon Molecular Sieve Fibers," *J Catal*, vol. 185, no. 1, pp. 223–235, Jul. 1999, doi: 10.1006/jcat.1999.2520.

[97] C. Ampelli, C. Genovese, R. Passalacqua, S. Perathoner, and G. Centi, "A gas-phase reactor powered by solar energy and ethanol for H_2 production," *Appl Therm Eng*, vol. 70, no. 2, pp. 1270–1275, Sep. 2014, doi: 10.1016/j.applthermaleng.2014.04.013.

[98] C. Ampelli, R. Passalacqua, C. Genovese, S. Perathoner, G. Centi, T. Montini, V. Gombac, J. J. Delgado Jaen, and P. Fornasiero, "H_2 production by selective photo-dehydrogenation of ethanol in gas and liquid phase on CuO_x/TiO_2 nanocomposites," *RSC Adv*, vol. 3, no. 44, p. 21776, 2013, doi: 10.1039/c3ra22804e.

[99] E. Behravesh, M. M. Melander, J. Wärnå, T. Salmi, K. Honkala, and D. Yu. Murzin, "Oxidative dehydrogenation of ethanol on gold: Combination of kinetic experiments and computation approach to unravel the reaction mechanism," *J Catal*, vol. 394, pp. 193–205, Feb. 2021, doi: 10.1016/j.jcat.2020.07.022.

[100] M. A. Nadeem, M. Murdoch, G. I. N. Waterhouse, J. B. Metson, M. A. Keane, J. Llorca, and H. Idriss, "Photoreaction of ethanol on Au/TiO_2 anatase: Comparing the micro to nanoparticle size activities of the support for hydrogen production," *J Photochem Photobiol A Chem*, vol. 216, no. 2–3, pp. 250–255, Dec. 2010, doi: 10.1016/j.jphotochem.2010.07.007.

[101] N. Bouchoul, H. Touati, E. Fourré, J. M. Clacens, I. Batonneau-Gener, and C. Batiot-Dupeyrat, "Plasma-catalysis coupling for CH_4 and CO_2 conversion over mesoporous macroporous Al_2O_3: Influence of the physico-chemical properties," *Appl Catal B*, vol. 295, Oct. 2021, doi: 10.1016/j.apcatb.2021.120262.

[102] H. H. Kim, A. A. Abdelaziz, Y. Teramoto, T. Nozaki, K. Hensel, Y. S. Mok, S. Saud, D. B. Nguyen, D. H. Lee, and W. S. Kang, "Interim report of plasma catalysis: Footprints in the past and blueprints for the future," *International Journal of Plasma Environmental Science and Technology*, vol. 15. Institute of Electrostatics, 2021. doi: 10.34343/ijpest.2021.15.e01004.

[103] X. Tu and J. C. Whitehead, "Plasma-catalytic dry reforming of methane in an atmospheric dielectric barrier discharge: Understanding the synergistic

effect at low temperature," *Appl Catal B*, vol. 125, pp. 439–448, Aug. 2012, doi: 10.1016/j.apcatb.2012.06.006.

[104] C. Tendero, C. Tixier, P. Tristant, J. Desmaison, and P. Leprince, "Atmospheric pressure plasmas: A review," *Spectrochimica Acta - Part B Atomic Spectroscopy*, vol. 61, no. 1. Elsevier, pp. 2–30, 2006. doi: 10.1016/j.sab.2005.10.003.

[105] X. Tu, *Plasma Catalysis*, vol. 106. Cham: Springer International Publishing, 2019. doi: 10.1007/978-3-030-05189-1.

[106] B. Eliasson and U. Kogelschatz, "Nonequilibrium volume plasma chemical processing," *IEEE Transactions on Plasma Science*, vol. 19, no. 6, pp. 1063–1077, 1991, doi: 10.1109/27.125031.

[107] H.-H. Kim, Y. Teramoto, N. Negishi, and A. Ogata, "A multidisciplinary approach to understand the interactions of nonthermal plasma and catalyst: A review," *Catal Today*, vol. 256, pp. 13–22, Nov. 2015, doi: 10.1016/j.cattod.2015.04.009.

[108] M. A. Lieberman and A. J. Lichtenberg, *Principles of Plasma Discharges and Materials Processing*. Wiley, 2005. doi: 10.1002/0471724254.

[109] A. Fridman, A. Chirokov, and A. Gutsol, "Non-thermal atmospheric pressure discharges," in *Journal of Physics D: Applied Physics*, Jan. 2005. doi: 10.1088/0022-3727/38/2/R01.

[110] H.-H. Kim, Y. Teramoto, A. Ogata, H. Takagi, and T. Nanba, "Plasma Catalysis for Environmental Treatment and Energy Applications," *Plasma Chemistry and Plasma Processing*, vol. 36, no. 1, pp. 45–72, Jan. 2016, doi: 10.1007/s11090-015-9652-7.

[111] R. Snoeckx and A. Bogaerts, “Plasma technology – a novel solution for CO_2 conversion?,” *Chem Soc Rev*, vol. 46, no. 19, pp. 5805–5863, 2017, doi: 10.1039/C6CS00066E.

[112] J. Van Durme, J. Dewulf, C. Leys, and H. Van Langenhove, “Combining non-thermal plasma with heterogeneous catalysis in waste gas treatment: A review,” *Appl Catal B*, vol. 78, no. 3–4, pp. 324–333, Feb. 2008, doi: 10.1016/j.apcatb.2007.09.035.

[113] M. A. Malik, A. Ghaffar, and S. A. Malik, “Water purification by electrical discharges,” *Plasma Sources Sci Technol*, vol. 10, no. 1, pp. 82–91, Feb. 2001, doi: 10.1088/0963-0252/10/1/311.

[114] A. M. Vandenbroucke, R. Morent, N. De Geyter, and C. Leys, “Non-thermal plasmas for non-catalytic and catalytic VOC abatement,” *J Hazard Mater*, vol. 195, pp. 30–54, Nov. 2011, doi: 10.1016/j.jhazmat.2011.08.060.

[115] X. Tu, H. J. Gallon, and J. C. Whitehead, “Electrical and spectroscopic diagnostics of a single-stage plasma-catalysis system: effect of packing with TiO $_2$,” *J Phys D Appl Phys*, vol. 44, no. 48, p. 482003, Dec. 2011, doi: 10.1088/0022-3727/44/48/482003.

[116] F. Thevenet, L. Sivachandiran, O. Guaitella, C. Barakat, and A. Rousseau, “Plasma–catalyst coupling for volatile organic compound removal and indoor air treatment: a review,” *J Phys D Appl Phys*, vol. 47, no. 22, p. 224011, Jun. 2014, doi: 10.1088/0022-3727/47/22/224011.

[117] E. C. Neyts and A. Bogaerts, “Understanding plasma catalysis through modelling and simulation—a review,” *J Phys D Appl Phys*, vol. 47, no. 22, p. 224010, Jun. 2014, doi: 10.1088/0022-3727/47/22/224010.

[118] F. Holzer, “Combination of non-thermal plasma and heterogeneous catalysis for oxidation of volatile organic compounds Part 1. Accessibility

of the intra-particle volume," *Appl Catal B*, vol. 38, no. 3, pp. 163–181, Sep. 2002, doi: 10.1016/S0926-3373(02)00040-1.

[119] U. Roland, F. Holzer, and F.-D. Kopinke, "Combination of non-thermal plasma and heterogeneous catalysis for oxidation of volatile organic compounds," *Appl Catal B*, vol. 58, no. 3–4, pp. 217–226, Jun. 2005, doi: 10.1016/j.apcatb.2004.11.024.

[120] K. Hensel, S. Katsura, and A. Mizuno, "DC microdischarges inside porous ceramics," *IEEE Transactions on Plasma Science*, vol. 33, no. 2, pp. 574–575, Apr. 2005, doi: 10.1109/TPS.2005.845389.

[121] F. Holzer, F. D. Kopinke, and U. Roland, "Influence of Ferroelectric Materials and Catalysts on the Performance of Non-Thermal Plasma (NTP) for the Removal of Air Pollutants," *Plasma Chemistry and Plasma Processing*, vol. 25, no. 6, pp. 595–611, Dec. 2005, doi: 10.1007/s11090-005-6804-1.

[122] D.-Z. Zhao, X.-S. Li, C. Shi, H.-Y. Fan, and A.-M. Zhu, "Low-concentration formaldehyde removal from air using a cycled storage–discharge (CSD) plasma catalytic process," *Chem Eng Sci*, vol. 66, no. 17, pp. 3922–3929, Sep. 2011, doi: 10.1016/j.ces.2011.05.019.

[123] H. L. Chen, H. M. Lee, S. H. Chen, M. B. Chang, S. J. Yu, and S. N. Li, "Removal of Volatile Organic Compounds by Single-Stage and Two-Stage Plasma Catalysis Systems: A Review of the Performance Enhancement Mechanisms, Current Status, and Suitable Applications," *Environ Sci Technol*, vol. 43, no. 7, pp. 2216–2227, Apr. 2009, doi: 10.1021/es802679b.

[124] N. Blin-Simiand, P. Tardiveau, A. Risacher, F. Jorand, and S. Pasquiers, "Removal of 2-Heptanone by Dielectric Barrier Discharges – The Effect of a Catalyst Support," *Plasma Processes and Polymers*, vol. 2, no. 3, pp. 256–262, Mar. 2005, doi: 10.1002/ppap.200400088.

[125] A. E. Wallis, J. C. Whitehead, and K. Zhang, “The removal of dichloromethane from atmospheric pressure nitrogen gas streams using plasma-assisted catalysis,” *Appl Catal B*, vol. 74, no. 1–2, pp. 111–116, Jun. 2007, doi: 10.1016/j.apcatb.2006.11.020.

[126] Y.-F. Guo, D.-Q. Ye, K.-F. Chen, J.-C. He, and W.-L. Chen, “Toluene decomposition using a wire-plate dielectric barrier discharge reactor with manganese oxide catalyst in situ,” *J Mol Catal A Chem*, vol. 245, no. 1–2, pp. 93–100, Feb. 2006, doi: 10.1016/j.molcata.2005.09.013.

[127] A. E. Wallis, J. C. Whitehead, and K. Zhang, “Plasma-assisted catalysis for the destruction of CFC-12 in atmospheric pressure gas streams using TiO_2,” *Catal Letters*, vol. 113, no. 1–2, pp. 29–33, Jan. 2007, doi: 10.1007/s10562-006-9000-x.

[128] Th. Hammer, Th. Kappes, and M. Baldauf, “Plasma catalytic hybrid processes: gas discharge initiation and plasma activation of catalytic processes,” *Catal Today*, vol. 89, no. 1–2, pp. 5–14, Feb. 2004, doi: 10.1016/j.cattod.2003.11.001.

[129] B. Lu, X. Zhang, X. Yu, T. Feng, and S. Yao, “Catalytic oxidation of benzene using DBD corona discharges,” *J Hazard Mater*, vol. 137, no. 1, pp. 633–637, Sep. 2006, doi: 10.1016/j.jhazmat.2006.02.012.

[130] J. Van Durme, J. Dewulf, W. Sysmans, C. Leys, and H. Van Langenhove, “Efficient toluene abatement in indoor air by a plasma catalytic hybrid system,” *Appl Catal B*, vol. 74, no. 1–2, pp. 161–169, Jun. 2007, doi: 10.1016/j.apcatb.2007.02.006.

[131] T. Sano, N. Negishi, E. Sakai, and S. Matsuzawa, “Contributions of photocatalytic/catalytic activities of TiO_2 and γ-Al_2O_3 in nonthermal plasma on oxidation of acetaldehyde and CO,” *J Mol Catal A Chem*, vol. 245, no. 1–2, pp. 235–241, Feb. 2006, doi: 10.1016/j.molcata.2005.10.002.

[132] K. Demeestere, J. Dewulf, T. Ohno, P. H. Salgado, and H. Van Langenhove, "Visible light mediated photocatalytic degradation of gaseous trichloroethylene and dimethyl sulfide on modified titanium dioxide," *Appl Catal B*, vol. 61, no. 1–2, pp. 140–149, Oct. 2005, doi: 10.1016/j.apcatb.2005.04.017.

[133] M. Kang, Y.-R. Ko, M.-K. Jeon, S.-C. Lee, S.-J. Choung, J.-Y. Park, S. Kim, and S.-H. Choi, "Characterization of Bi/TiO_2 nanometer sized particle synthesized by solvothermal method and CH_3CHO decomposition in a plasma-photocatalytic system," *J Photochem Photobiol A Chem*, vol. 173, no. 2, pp. 128–136, Jul. 2005, doi: 10.1016/j.jphotochem.2004.12.030.

[134] O. Guaitella, F. Thevenet, E. Puzenat, C. Guillard, and A. Rousseau, "C_2H_2 oxidation by plasma/TiO_2 combination: Influence of the porosity, and photocatalytic mechanisms under plasma exposure," *Appl Catal B*, vol. 80, no. 3–4, pp. 296–305, May 2008, doi: 10.1016/j.apcatb.2007.11.032.

[135] A. Maciuca, C. Batiot-Dupeyrat, and J.-M. Tatibouët, "Synergetic effect by coupling photocatalysis with plasma for low VOCs concentration removal from air," *Appl Catal B*, vol. 125, pp. 432–438, Aug. 2012, doi: 10.1016/j.apcatb.2012.06.012.

[136] T. Liu, C. Wang, Y. Song, W. Ou, R. Xiao, and D. Zeng, "Enhanced C_{2+} selectivity in plasma-assisted chemical looping oxidative coupling of methane using (Na, Li, and K) doped $LaMnO_3$," *Sustain Energy Fuels*, vol. 7, no. 10, pp. 2455–2461, 2023, doi: 10.1039/D3SE00292F.

[137] J. Kim, J. Jeoung, J. Jeon, J. Kim, Y. S. Mok, and K.-S. Ha, "Effects of dielectric particles on non-oxidative coupling of methane in a dielectric barrier discharge plasma reactor," *Chemical Engineering Journal*, vol. 377, p. 119896, Dec. 2019, doi: 10.1016/j.cej.2018.09.057.

[138] Y. Uytdenhouwen, K. M. Bal, E. C. Neyts, V. Meynen, P. Cool, and A. Bogaerts, “On the kinetics and equilibria of plasma-based dry reforming of methane,” *Chemical Engineering Journal*, vol. 405, p. 126630, Feb. 2021, doi: 10.1016/j.cej.2020.126630.

[139] Y. X. Zeng, L. Wang, C. F. Wu, J. Q. Wang, B. X. Shen, and X. Tu, “Low temperature reforming of biogas over K-, Mg- and Ce-promoted Ni/Al_2O_3 catalysts for the production of hydrogen rich syngas: Understanding the plasma-catalytic synergy,” *Appl Catal B*, vol. 224, pp. 469–478, May 2018, doi: 10.1016/j.apcatb.2017.10.017.

[140] L. Wang, Y. Yi, C. Wu, H. Guo, and X. Tu, “One-Step Reforming of CO_2 and CH_4 into High-Value Liquid Chemicals and Fuels at Room Temperature by Plasma-Driven Catalysis,” *Angewandte Chemie International Edition*, vol. 56, no. 44, pp. 13679–13683, Oct. 2017, doi: 10.1002/anie.201707131.

[141] A. N. Biswas, L. R. Winter, B. Loenders, Z. Xie, A. Bogaerts, and J. G. Chen, “Oxygenate Production from Plasma-Activated Reaction of CO_2 and Ethane,” *ACS Energy Lett*, vol. 7, no. 1, pp. 236–241, Jan. 2022, doi: 10.1021/acsenergylett.1c02355.

[142] L. Hollevoet, F. Jardali, Y. Gorbanev, J. Creel, A. Bogaerts, and J. A. Martens, “Towards Green Ammonia Synthesis through Plasma-Driven Nitrogen Oxidation and Catalytic Reduction,” *Angewandte Chemie International Edition*, vol. 59, no. 52, pp. 23825–23829, Dec. 2020, doi: 10.1002/anie.202011676.

[143] Z. Chen, S. Jaiswal, A. Diallo, S. Sundaresan, and B. E. Koel, “Effect of Porous Catalyst Support on Plasma-Assisted Catalysis for Ammonia Synthesis,” *J Phys Chem A*, vol. 126, no. 46, pp. 8741–8752, Nov. 2022, doi: 10.1021/acs.jpca.2c05023.

[144] X. Hu, S. Zhang, L. Dou, Y. Gao, C. Zhang, and T. Shao, “Plasma-enabled sustainable ammonia synthesis at atmospheric pressure: The role of catalysts on synergistic effect,” *Catal Today*, vol. 422, p. 114245, Oct. 2023, doi: 10.1016/j.cattod.2023.114245.

[145] J. Liu, X. Zhu, S. Jiang, H. Zhang, Y. Hong, G. Chen, and X. Tu, “Plasma-catalytic synthesis of ammonia over Ru/$BaTiO_3$-based bimetallic catalysts: Synergistic effect from dual-metal active sites,” *Fuel Processing Technology*, vol. 250, p. 107851, Nov. 2023, doi: 10.1016/j.fuproc.2023.107851.

[146] G. Akay and K. Zhang, “Process Intensification in Ammonia Synthesis Using Novel Coassembled Supported Microporous Catalysts Promoted by Nonthermal Plasma,” *Ind Eng Chem Res*, vol. 56, no. 2, pp. 457–468, Jan. 2017, doi: 10.1021/acs.iecr.6b02053.

[147] K. H. R. Rouwenhorst, Y. Engelmann, K. van ‘t Veer, R. S. Postma, A. Bogaerts, and L. Lefferts, “Plasma-driven catalysis: green ammonia synthesis with intermittent electricity,” *Green Chemistry*, vol. 22, no. 19, pp. 6258–6287, 2020, doi: 10.1039/D0GC02058C.

[148] L. Hollevoet, E. Vervloessem, Y. Gorbanev, A. Nikiforov, N. De Geyter, A. Bogaerts, and J. A. Martens, “Energy-Efficient Small-Scale Ammonia Synthesis Process with Plasma-Enabled Nitrogen Oxidation and Catalytic Reduction of Adsorbed NO_x,” *ChemSusChem*, vol. 15, no. 10, May 2022, doi: 10.1002/cssc.202102526.

[149] D. Ray, P. Ye, J. C. Yu, and C. Song, “Recent progress in plasma-catalytic conversion of CO_2 to chemicals and fuels,” *Catal Today*, vol. 423, p. 113973, Nov. 2023, doi: 10.1016/j.cattod.2022.12.004.

[150] I. Michielsen, Y. Uytdenhouwen, J. Pype, B. Michielsen, J. Mertens, F. Reniers, V. Meynen, and A. Bogaerts, “CO_2 dissociation in a packed bed

DBD reactor: First steps towards a better understanding of plasma catalysis," *Chemical Engineering Journal*, vol. 326, pp. 477–488, Oct. 2017, doi: 10.1016/j.cej.2017.05.177.

[151] S. Zhu, A. Zhou, F. Yu, B. Dai, and C. Ma, "Enhanced CO_2 decomposition via metallic foamed electrode packed in self-cooling DBD plasma device," *Plasma Science and Technology*, vol. 21, no. 8, p. 085504, Aug. 2019, doi: 10.1088/2058-6272/ab15e5.

[152] L. Wang, Y. Yi, H. Guo, and X. Tu, "Atmospheric Pressure and Room Temperature Synthesis of Methanol through Plasma-Catalytic Hydrogenation of CO_2," *ACS Catal*, vol. 8, no. 1, pp. 90–100, Jan. 2018, doi: 10.1021/acscatal.7b02733.

[153] *The IUPAC Compendium of Chemical Terminology*. Research Triangle Park, NC: International Union of Pure and Applied Chemistry (IUPAC), 2019. doi: 10.1351/goldbook.

[154] A. R. West, *Solid State Chemistry and Its Applications*. 2014.

[155] A. Trenczek-Zajac, J. Banas-Gac, and M. Radecka, "TiO_2@Cu_2O n-n Type Heterostructures for Photochemistry," *Materials*, vol. 14, no. 13, p. 3725, Jul. 2021, doi: 10.3390/ma14133725.

[156] H. L. Tan, F. F. Abdi, and Y. H. Ng, "Heterogeneous photocatalysts: an overview of classic and modern approaches for optical, electronic, and charge dynamics evaluation," *Chem Soc Rev*, vol. 48, no. 5, pp. 1255–1271, 2019, doi: 10.1039/C8CS00882E.

[157] E. Kalamaras, M. M. Maroto-Valer, M. Shao, J. Xuan, and H. Wang, "Solar carbon fuel via photoelectrochemistry," *Catal Today*, vol. 317, pp. 56–75, Nov. 2018, doi: 10.1016/j.cattod.2018.02.045.

[158] Y. Li, Z. Fu, and B. Su, “Hierarchically Structured Porous Materials for Energy Conversion and Storage,” *Adv Funct Mater*, vol. 22, no. 22, pp. 4634–4667, Nov. 2012, doi: 10.1002/adfm.201200591.

[159] J. A. L. Perini, F. Tavella, E. P. Ferreira Neto, M. V. B. Zanoni, S. J. L. Ribeiro, D. Giusi, G. Centi, S. Perathoner, and C. Ampelli, “Role of nanostructure in the behaviour of $BiVO_4$–TiO_2 nanotube photoanodes for solar water splitting in relation to operational conditions,” *Solar Energy Materials and Solar Cells*, vol. 223, p. 110980, May 2021, doi: 10.1016/j.solmat.2021.110980.

[160] P. Dong, G. Hou, X. Xi, R. Shao, and F. Dong, “WO_3 -based photocatalysts: morphology control, activity enhancement and multifunctional applications,” *Environ Sci Nano*, vol. 4, no. 3, pp. 539–557, 2017, doi: 10.1039/C6EN00478D.

[161] N. Bao, L. Shen, T. Takata, and K. Domen, “Self-Templated Synthesis of Nanoporous CdS Nanostructures for Highly Efficient Photocatalytic Hydrogen Production under Visible Light,” *Chemistry of Materials*, vol. 20, no. 1, pp. 110–117, Jan. 2008, doi: 10.1021/cm7029344.

[162] Y. Zheng, J. Liu, J. Liang, M. Jaroniec, and S. Z. Qiao, “Graphitic carbon nitride materials: controllable synthesis and applications in fuel cells and photocatalysis,” *Energy Environ Sci*, vol. 5, no. 5, p. 6717, 2012, doi: 10.1039/c2ee03479d.

[163] S. Stankovich, D. A. Dikin, G. H. B. Dommett, K. M. Kohlhaas, E. J. Zimney, E. A. Stach, R. D. Piner, S. T. Nguyen, and R. S. Ruoff, “Graphene-based composite materials,” *Nature*, vol. 442, no. 7100, pp. 282–286, Jul. 2006, doi: 10.1038/nature04969.

[164] S. Y. Lim, W. Shen, and Z. Gao, “Carbon quantum dots and their applications,” *Chem Soc Rev*, vol. 44, no. 1, pp. 362–381, 2015, doi: 10.1039/C4CS00269E.

[165] R. H. Baughman, A. A. Zakhidov, and W. A. de Heer, “Carbon Nanotubes--the Route Toward Applications,” *Science (1979)*, vol. 297, no. 5582, pp. 787–792, Aug. 2002, doi: 10.1126/science.1060928.

[166] A. Kumar, P. Choudhary, A. Kumar, P. H. C. Camargo, and V. Krishnan, “Recent Advances in Plasmonic Photocatalysis Based on TiO_2 and Noble Metal Nanoparticles for Energy Conversion, Environmental Remediation, and Organic Synthesis,” *Small*, vol. 18, no. 1, Jan. 2022, doi: 10.1002/smll.202101638.

2. Nanostructured photoactive materials for conversion of small molecules: 3D vs. 2D structure

2.1. Introduction and scope of the chapter

Titanium dioxide is a *n-type* semiconductor material with a long history of use in various applications, (illustrated in Figure 2.1), which include pigments, plastics, paper, textiles, photocatalytic applications, such as purification of water and air, decomposition of organic compounds, photovoltaic applications, energy storage applications, gas sensor and catalyst[1–5]. Its qualities, like chemical stability, durability, non-toxicity, and economic viability have made it one of the most used photoactive materials[6].

There can be different polymorph structures of TiO_2, illustrated in Figure 2.2: anatase (2.2 c), rutile (2.2 a), which are tetragonal, brookite (2.2 b), which is orthorhombic, and TiO_2 (B) (2.2 d) [7, 8]. Anatase and rutile can be easily prepared in the laboratory, on the contrary brookite is difficult to synthesize. Usually, anatase and rutile have been used in photocatalytic applications. In particular, anatase is the most active, probably because of the presence of surface hydroxyl groups in the low-temperature anatase structure and also because of the difference in the Fermi level, which is 0.1 eV higher in the anatase phase than in rutile[9].

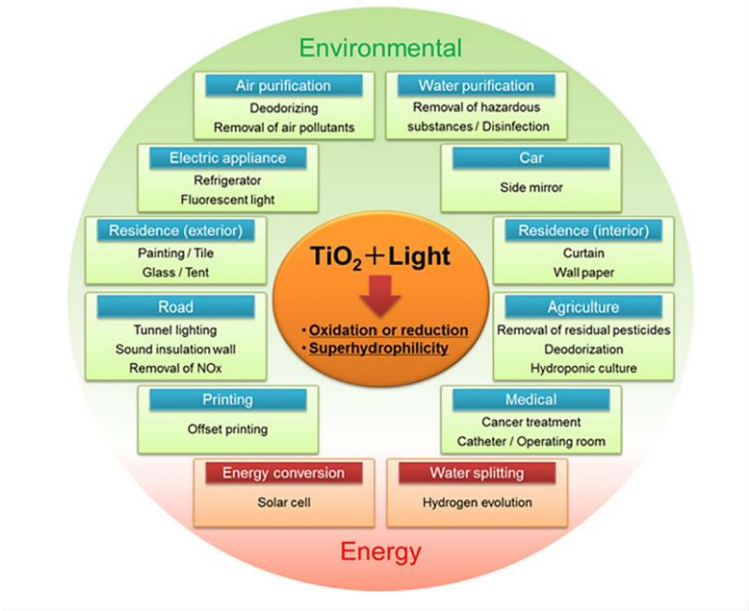

Figure 2.1 *Application of Titanium dioxide in photocatalysis. Reproduced with permission from ref.* [6]

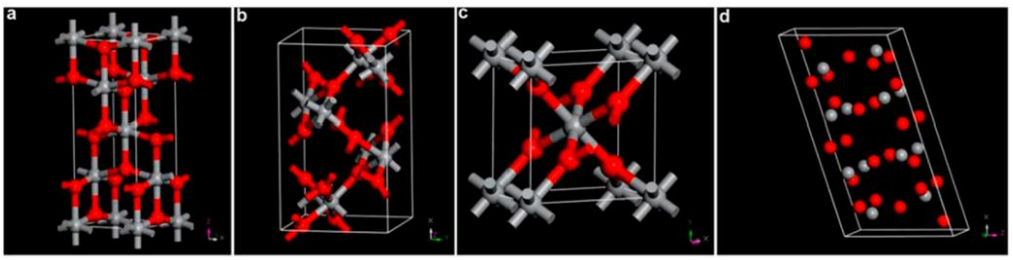

Figure 2.2 *Crystal structure of TiO_2 polymorphs: (**a**) rutile; (**b**) brookite; (**c**) anatase; (**d**) TiO_2(B). Reproduced with permission from ref.*[12]

Illustrated in Figure 2.3 (a) is the general mechanism of the electrons excitation from the valence band to the conduction band, forming positive holes in the valence band of TiO_2, caused by the absorption of ultraviolet (UV) light with an energy equal or higher than the band gap energy[5]. After this excitation, electrons and holes can radiatively or non-radiatively recombine or be trapped and

subsequently react with the species adsorbed on the surface of TiO_2[10]. These two processes are competitive.

The photocatalytic water-splitting process, in Figure 2.3 (b), involves the photogenerated electrons and holes of TiO_2, in the reactions of oxygen and hydrogen formations. For spontaneous water-splitting, these reactions must be between the valence band maximum and the conduction band minimum, and the bands of TiO_2 satisfy this requirement[11].

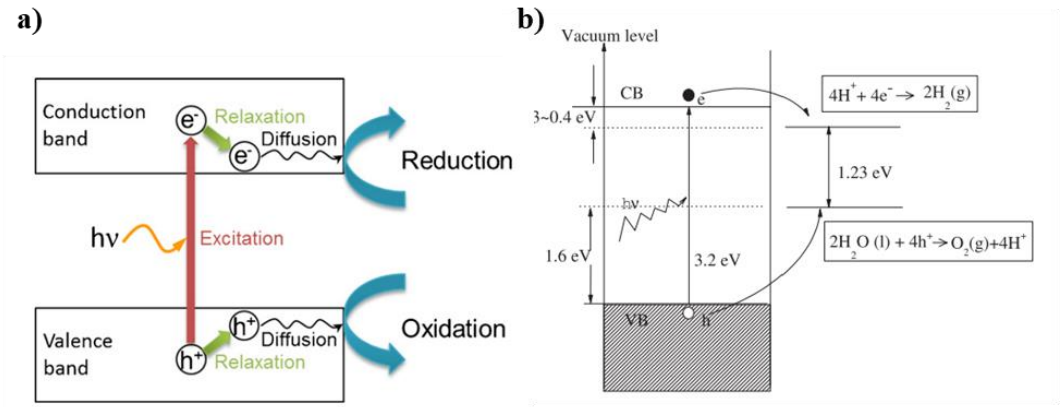

Figure 2.3 *In (**a**) the scheme of the mechanism of the photogeneration of the charge carriers after the ultraviolet light absorption. Reproduced with permission from ref.* [6] *. In (b) the scheme of TiO_2 bands relative to the standard levels of water oxidation and hydrogen production reactions. Reproduced with permission from ref.* [11]

Nevertheless, titanium dioxide has some disadvantages: a wide band gap energy, 3.0-3.2 eV, which limits the application to UV light absorption[8, 13, 14] reducing the energy conversion efficiency, and a fast recombination of the photogenerated electron-hole [8, 15, 16].

For these reasons, the research has been focused on the modification and functionalization of titanium dioxide structure to[6]:

1) reduce the band gap and thus enhance the light absorption
2) maximize the catalyst adsorption capacity for the reactant molecules

3) boost the charge transfer rate with consequent reduced recombination rates

One strategy is the creation of TiO_2 nano- or micro-structures with modified morphologies and characteristics[6]. For example, lithium-ion batteries, electrochromic displays, dye-sensitized solar cells (DSSCs), and photocatalysis are only a few applications of nanostructured TiO_2 materials[17–19]. Figure 2.4 shows a schematic classification of the different nanostructured materials with the corresponding dimensional characteristics and the expected properties[6].

0D materials, such as TiO_2 nano-spheres, are characterized by high specific surface area, which enhances their photocatalytic performances and light harvesting properties[20–22].

1D TiO_2 materials, such as tubes and fibres, have high surface-to-volume ratios, which allow a high interfacial charge carrier transfer rate and a decrease in the hole-electron recombination rate, both of which, as it was discussed, are advantageous for photocatalytic processes. TiO_2 nanotube arrays can be also tailored in terms of length, inner diameter and spacing between them, using the controlled anodic oxidation technique on a titanium substrate (foil, mesh), which makes them versatile and easily synthetized[23–28]. Also, the nanotubes grown on a Ti wire were shown to absorb incoming, reflected, and refracted light in all directions, reducing the scattering effects of the liquid and boosting photoactivity[29, 30].

2D TiO_2 nanosheets are characterized by having a small thickness (1-100 nm) and a flat surface. This conformation combined with high adhesion, gives these materials excellent performances for example in self-cleaning coating [31].

3D complex hierarchical structures generated by the interconnection of a macroscopic shape and a porous structure can influence greatly the physical properties and the performances of the titanium dioxide material[32]. The modification of the empty and solid spaces of the material could generate, among

other properties, specific interactions with light, scattering and photonic effects, leading to the enhancement of visible light harvesting and overall photoactivity[6]. Specifically, combining the already tuneable nanotube array with a macropore structure, as a mesh, could not only improve the light-harvesting and thus the photoactivity but also reduce the diffusion limitations [28].

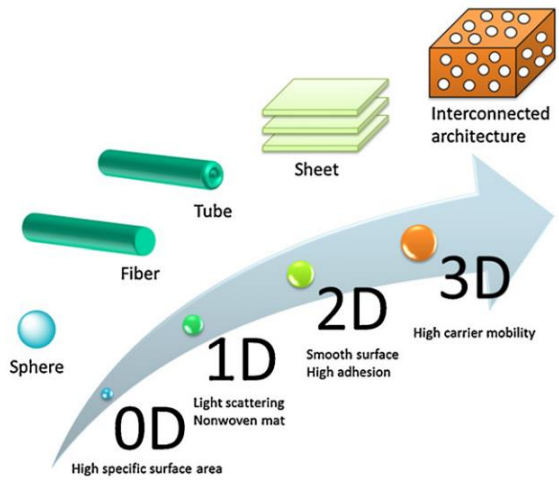

Figure 2.4 *Schematics of the different structural dimensions with the expected properties. Reproduced with permission from ref.*[6]

Nanostructured titanium dioxide through anodic oxidation

Titanium dioxide nanotubes, synthesized through anodic oxidation (AO) of titanium foils in an electrolyte containing fluoride ions, were first reported by Grimes' group in 2001[33]. This kind of technique allows the precise control of their dimensions, but the morphology and specific structure of the titania layers grown on the titanium metallic support, are highly influenced by the experimental conditions, so the length, pore size and wall thickness of the tubes can be tailored properly adjusting the electrochemical parameters [27, 34]. In Figure 2.5 the key processes of the nanotubes formation are reported.

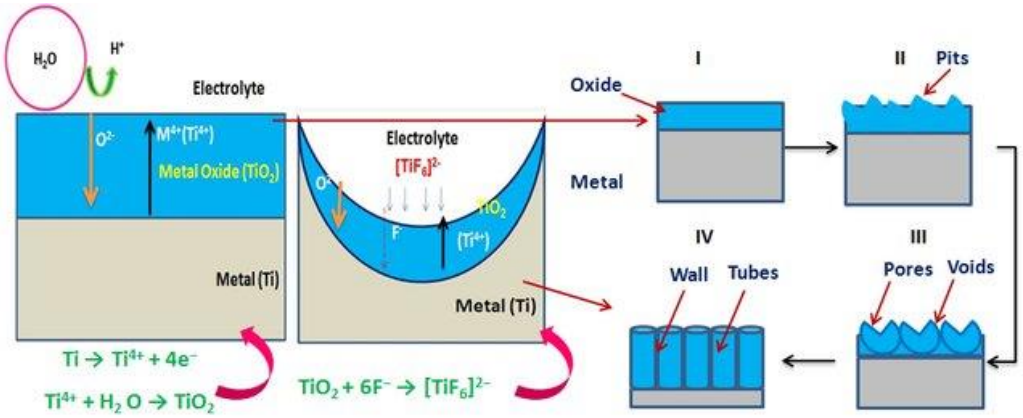

Figure 2.5 *Scheme of titanium dioxide nanotube formation mechanism, reproduced with permission from. In* ***(I)*** *the early formation of the oxide layer; in* ***(II)*** *the formation of the pits; in* ***(III)*** *the void formation between the pores; in* ***(IV)*** *the titanium dioxide nanotube formation. On the left are the detailed reactions which take place in the nanotube formation. Reproduced with permission from ref.* [35]

a. *Initial oxidation step*

At the anode, the reaction which takes place is the metal oxidation (Equation 1).

$$Ti \rightarrow Ti^{4+} + 4e^{-}$$

Equation 1

The Ti^{4+} ions react with OH^- and O^{2-}, supplied by water. The dissociation of water is promoted by the electric field present in the system. This leads to the formation of hydrated oxides (Equation 2) and oxides (Equation 3). Then, the hydroxide is further oxidized into the hydrated anode layer (Equation 4) and at the cathode the hydrogen is formed (Equation 5).

$$Ti^{4+} + 4OH^{-} \rightarrow Ti(OH)_4$$

Equation 2

$$Ti^{4+} + 2O^{2-} \rightarrow TiO_2$$

Equation 3

$$Ti(OH)_4 \rightarrow TiO_2 + 2H_2O$$

Equation 4

$$4H^+ + 4e^- \rightarrow 2H_2$$

Equation 5

The reactions 1-5 can be summarized with the following equation, which describe the initial formation of the oxide film on the anode surface:

$$Ti + 2H_2O \rightarrow TiO_2 + 2H_2$$

Equation 6

b. *Porous oxide film formation*

The fluoride ions weaken the Ti-O bonds and react to form a fluorine stable complex $[TiF_6]^{2-}$ (Equation 7, Equation 8, Equation 9).

$$TiO_2 + 6F^- + 4H^+ \rightarrow [TiF_6]^{2-} + 2H_2O$$

Equation 7

$$Ti(OH)_4 + 6F^- \rightarrow [TiF_6]^{2-} + 4OH^-$$

Equation 8

$$Ti^{4+} + 6F^- \rightarrow [TiF_6]^{2-}$$

Equation 9

The fluoride ions are not evenly distributed in the solution but are accumulated along the surface of the oxide film, and due to a strong electric field, locally dissolve the oxide creating porous cores that expand into micropores then forming a porous structure oxide film.

c. *Oxidation film growth*

As the micropores grow, the not-oxidized titanium between the holes forms a peak shape, enhancing the electric field. In this way the upper part of the oxide film increases the rate of dissolution, resulting in small

cavities (Figure 2. III). These become gradually deeper, and the continuous pores are separated to form an independent nanotube structure (Figure 2. IV). As the equilibrium between the oxide formation reaction and the chemical dissolution reaction is reached, the length of the nanotubes stays constant.

The side reaction of oxygen formation (Equation 10) during the titanium anodic oxidation process affects the morphology of the anode layer and the growth efficiency of nanotubes. The oxygen production is generally more pronounced in aqueous solutions but can also be observed in organic media containing a small amount of water (up to 5 vol%).

$$2H_2O \rightarrow O_2 + 4e^- + 4H^+$$

Equation 10

Many parameters, such as the applied voltage, the pH, and the concentration of fluorite and water, strongly affect this process favouring the dissolution and/or the oxidation steps changing the nanotube growth rate and the morphology of the titania porous nanostructured film. For this reason, this chapter outlines the process of synthesizing electrodes based on titanium dioxide nanotubes grown over a titanium mesh or foil, by controlled anodic oxidation, where various parameters have been manipulated to achieve diverse morphological, electrical, and optical characteristics of the materials. Specifically, adjustments were made to the electrolyte solution, anodization time and voltage, to create the most suitable nanotube substrate in terms of morphology and photoactivity. The results are given in detail in the first part of the chapter (section 2.3). In the second part of the chapter (section 2.4) is reported an extensive study performed to analyse the impact of the substrate geometry (titanium mesh or foil) on the photocatalytic behaviour of the material. The TiO_2 nanotubes grown on a Ti mesh, have a mesostructure (nanotubes arrays) on a three-dimensional macroporous structure

(the mesh), which may improve the light harvesting and diffusion properties and the overall photoconversion efficiencies. Specifically, electrochemical impedance spectroscopy (EIS) was employed (with cyclic voltammetry, CV and chronoamperometry, CA) in both dark and illuminated conditions to establish correlations between photoactivity and charge transfer resistances due to the specific geometry of the support: 2D (foil) vs 3D (mesh). The different substrates, mesh and foil, were then tested in the reaction of photo-electrolysis of the water, to correlate the effect of a specific structure on its photoactivity.

2.2. Experimental: titanium dioxide nanotubes synthesis

Titanium dioxide nanotubes (TiO_2NTs) were synthesized on a titanium gauze substrate consisting of 80 mesh woven from a 0.13 mm diameter wire, provided by Alfa Aesar. This synthesis was achieved through a controlled anodic oxidation process. Before anodization, the samples were subjected to a 30-minute sonication in isopropyl alcohol to eliminate any organic impurities and then allowed to air-dry. Subsequently, the clean substrate was positioned within a two-electrode electrochemical cell made in Teflon, serving as the working electrode, while a platinum (Pt) electrode was employed as the counter electrode. A potentiostat (Agilent E3612A) and a multimeter (Keithley 2000) were employed to maintain a constant potential between the two electrodes, in the range of 10-70 V (see Table 2.) for a variable time from 0.5 to 5 hours (see Table 2.), while recording the current density. A picture of the setup is shown in Figure 2.6. The electrolyte bath was prepared with 2.0 wt% distilled H_2O and 0.3 wt% ammonium fluoride in ethylene glycol. Other electrolyte bath compositions were employed varying the organic solvent, therefore replacing the ethylene glycol with diethylene glycol and glycerol (see Table 2.). After the anodization, the samples were annealed at 450°C for 3 hours, with a heating and cooling rate of 2°C/min, to induce crystallization of the amorphous oxide nanotube arrays.

The same anodization procedure (at 50V for 1h) was employed using as support a titanium (Ti) disc (Ti 99.96%, thickness of 0.025 mm, diameter of 35 mm, Alfa Aesar), instead of the mesh.

Figure 2.6 *Anodic oxidation experimental set-up*

2.2.1. Anodization parameters: potential, time, and bath composition

For a better understanding of the anodization voltage and time effects on the growth and pattern of nanotubes, many samples were prepared i) increasing the anodization potential from 10 to 70 volts and maintaining constant the time of the process (1h) or ii) changing the anodization time, from 0.5 h to 5 h at a fixed voltage (50V), using the ethylene glycol-based electrolyte bath.

The experimental parameters for each synthesis are summarized in Table 2.1.

Sample	Potential	Time	Electrolyte
TG_1	10 V	1 h	Ethylene glycol - 0.3 wt% NH_4F - 2 wt% H_2O
TG_2	30 V	1 h	Ethylene glycol - 0.3 wt% NH_4F - 2 wt% H_2O
TG_3	50 V	1 h	Ethylene glycol - 0.3 wt% NH_4F - 2 wt% H_2O

TG_4	70 V	1 h	Ethylene glycol - 0.3 wt% NH_4F - 2 wt% H_2O
TG_5	50 V	0.5 h	Ethylene glycol - 0.3 wt% NH_4F - 2 wt% H_2O
TG_6	50 V	1 h	Ethylene glycol - 0.3 wt% NH_4F - 2 wt% H_2O
TG_7	50 V	3 h	Ethylene glycol - 0.3 wt% NH_4F - 2 wt% H_2O
TG_8	50 V	5 h	Ethylene glycol - 0.3 wt% NH_4F - 2 wt% H_2O

Table 2.1 *Experimental parameters of titanium mesh anodization, indicating the potential, time, and electrolyte bath*

The effect of changing the electrolyte bath's composition was also investigated. Many studies reported in the literature suggested that a different bath composition could promote the formation of spaced nanotubes[34, 36, 37]; for this reason, diethylene glycol and glycerol were employed instead of ethylene glycol, also changing the anodization potentials; all the details about the experimental conditions are reported in Table 2.2.

Sample	Potential	Time	Electrolyte
TG_9	10 V	1 h	Diethylene glycol - 0.3 wt% NH_4F - 2 wt% H_2O
TG_10	30 V	1 h	Diethylene glycol - 0.3 wt% NH_4F - 2 wt% H_2O
TG_11	50 V	1 h	Diethylene glycol - 0.3 wt% NH_4F - 2 wt% H_2O
TG_12	70 V	1 h	Diethylene glycol - 0.3 wt% NH_4F - 2 wt% H_2O
TG_13	50 V	1 h	Glycerol - 0.3 wt% NH_4F - 2 wt% H_2O
TG_14	50 V	1 h	Ethylene glycol : Diethylene glycol 1:1 (vol.) - 0.3 wt% NH_4F - 2 wt% H_2O
TG_15	70 V	1 h	Ethylene glycol : Diethylene glycol 1:1 (vol.) - 0.3 wt% NH_4F - 2 wt% H_2O

Table 2.2 *Experimental parameters of titanium mesh anodization, indicating the potential, time, and electrolyte bath.*

2.3. Results: optimization of the anodization parameters

2.3.1. Morphological and photo-electrochemical characterization

The morphology of the TiO_2NTs-based photocatalysts was studied using a Phenom ProX Scanning Electron Microscope (SEM) equipped with EDS.

The SEM images of TG_3 synthesized at 50 V for one hour of anodization, are displayed in Figure 2.7. Additionally, a picture of the Ti mesh is presented (refer to Figure 2.7 a), which illustrates how the substrate after oxidation changed colour. Due to the development of titania nanotubes on the rounded surface of the woven Ti wires, the surface resulted unsmooth. The TiO_2NTs cross-section SEM images, displayed at varying magnifications in Figure 2.7 c and d, demonstrated their vertical alignment and average length of 1.4 μm. Based on a direct measurement from the top-view picture, the inner diameter of the TiO_2NTs was between 60 and 70 nm (see the inset in Figure 2.7 d). The resultant TiO_2NTs on the Ti mesh had an open area of approximately 33% because of the macro holes in the meshed structure. In Figure 2.8 is reported the elemental analysis of TG_3 obtained by EDX, which confirmed the presence of the titanium dioxide.

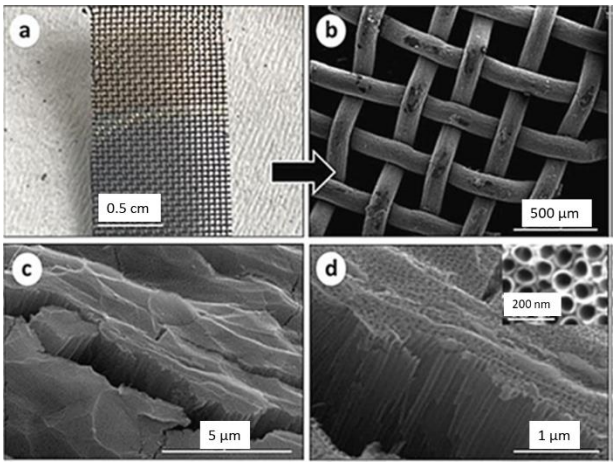

***Figure 2.7** (**a**) TG_3 before (upper part) and after (bottom part) the anodization; (**b**) SEM image of TG_3 after the anodization at 50 V for 1 h ; (**c**) SEM image of the cross-section of TG_3 at low magnification and (**d**) high magnification, with the top view in the upper right part. Reproduced with permission from ref.*[38]

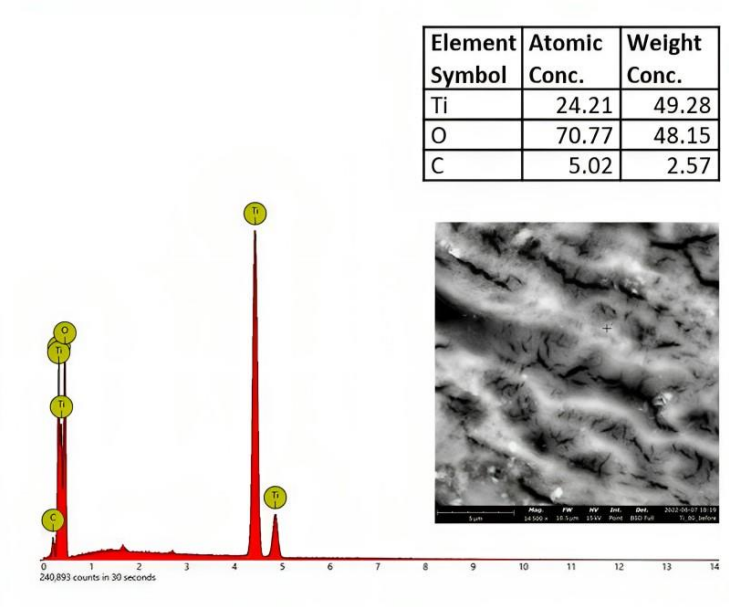

Figure 2.8 *Elemental analysis by EDX of TG_3. Reproduced with permission from ref.* [38]

The effect of the applied voltage (affecting the electric field during the anodization process), was well evidenced from the SEM images of the samples anodized at 10V, 30V and 70V reported in Figures 2.9 and 2.10. The images illustrate the varying degrees of nanotube development, with noticeable differences in surface characteristics and degree of nanotube formation.

Figure 2.9 presents the top view image of the sample subjected to anodization at 10 V for 1 hour (TG_1). A comparison with Figure 2.7 (d) distinctly revealed that the nanotubes were not fully developed, resulting in an uneven and rough surface. For the sample anodized at 30 V for the same time, some nanotubes were visible (Figure 2.10). However, at the top of the array, the surface maintained its rough texture despite the beginning of certain nanotube formations. In general, the formation of nanotubes seemed to be linearly dependent on the applied voltage as reported in literature [33]. The cross-section of the sample anodized at 70V (TG_4), (Figure 2.11) showed instead nanotubes completely formed, but not perfectly homogeneous due to the higher anodization potential. As already reported[14, 16, 28],

a relatively high anodization potential could lead to a diminishing nanotube diameter, probably due to the higher electromagnetic fields in the first stage of the pits formation, and to a detachment of the nanotube array.

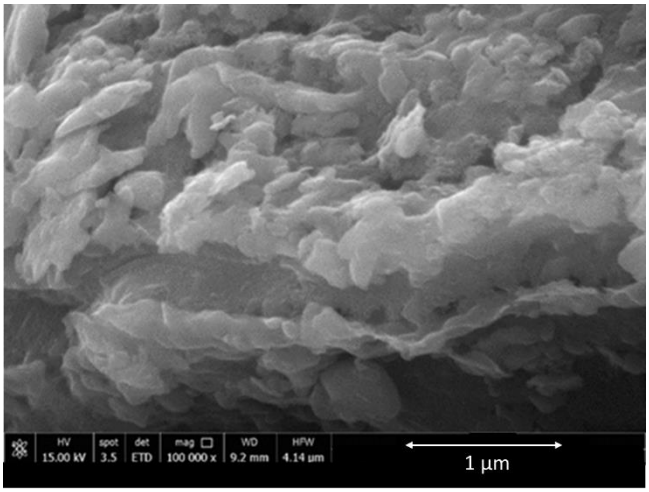

Figure 2.9 *SEM image of the top view of the sample TG_1, anodized at 10 V for 1 h*

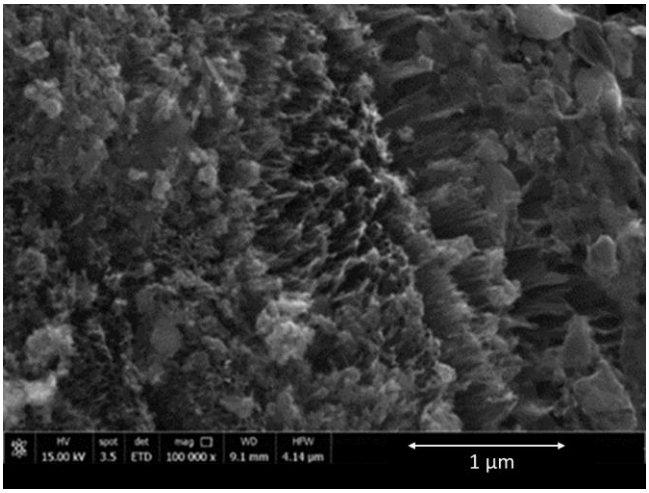

Figure 2.10 *SEM image of the top view of the sample TG_2, anodized at 30 V for 1 h*

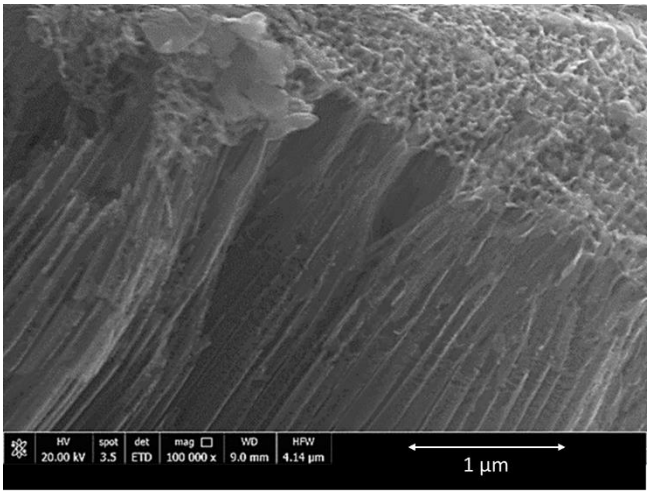

Figure 2.11 *SEM image of the cross-section of TG_4, anodized at 70 V for 1 h, at low magnification.*

The photocurrent behaviour was evaluated by chronoamperometry using a three-electrode photo-electrochemical cell, illustrated in Figure 2.12, consisting of a Pyrex flask modified with a quartz window for illumination. The reference electrode was a saturated Ag/AgCl (KCl ≈ 3 M) electrode, and the counter-electrode consisted of a Pt wire, while the TiO_2NTs-based catalyst (with square dimensions 1 × 1 cm) acted as the working electrode. Using a 2049 AMEL potentiostat-galvanostat, all experiments were run at room temperature in a 1 M KOH solution at +1.136 V vs RHE (+0.1 V vs. Ag/AgCl). The potential values referred to the Ag/AgCl electrode were translated to RHE using the formula specified in the Annex section.

A solar simulator (Lot-Oriel 300 W Xe-arc lamp) equipped with various filters to cut out different ranges of wavelengths, was used for the irradiation of the samples. The filters used in this study were: the AM 1.5 G filter, which simulates the standard solar irradiation on Earth (with the UV part only about 4 % of the entire spectrum), the UV-C blocking filter, and the UV B/C blocking filter. The samples were exposed to 30-second ON and OFF cycles of irradiation, during which the current density increased and then quickly returned to its initial value when the light was turned off showing high reproducibility. If not specified, in all

experiments three cycles at open spectrum (and the last) were performed at the beginning.

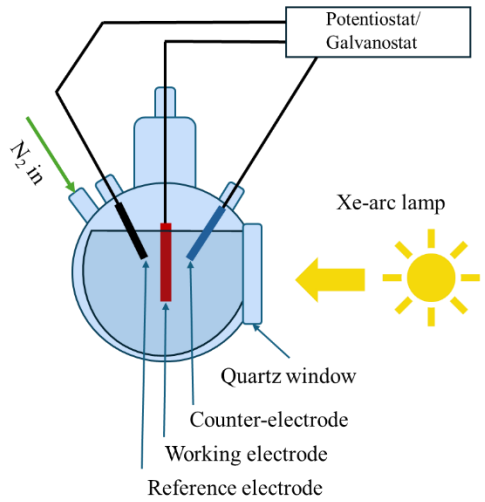

Figure 2.12 *Schematics of the set-up used for the chronoamperometric measurements.*

Figure 2.13 shows the photocurrent behaviour of the samples anodized at various potentials from 10 V to 70 V respectively (see table 2.1 for details). Notably, there is an upward trend in photocurrent values from samples anodized from 10 (TG_1) to 50 V (TG_3), indicating a direct correlation between the anodization potential and the resulting photocurrent density. This trend aligns with the evolving state of nanotube development, as evidenced by the SEM images, wherein the growth of a homogenous layer of nanotubes corresponds to the increasing anodization potentials. In the presence of an AM1.5G filter (with visible light), all the TiO_2NTs electrodes showed partial activity, confirming the importance of nanostructures in this process, and in this case, the sample anodized at 50V showed the best photocurrent. An inversion in the trend was observed with the sample TG_4 anodized at the highest voltage (70V) that displayed the lowest photocurrent density (at full spectrum irradiation and with the UV-C cut-off filter) confirming the not perfect homogeneity of the nanotubes layer that probably did not allow a fast charge mobility favouring charge recombination phenomena.

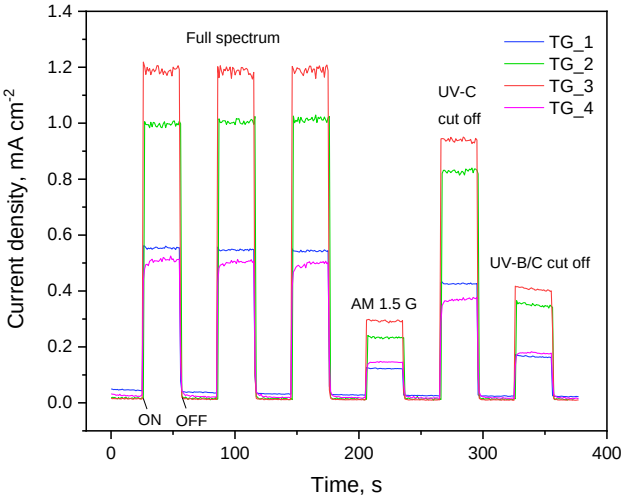

Figure 2.13 *Chronoamperometric measurements (1.136 V vs. RHE, 1 M KOH) for TiO_2NTs/Ti mesh anodized at different potentials using open UV-visible lamp spectrum (no light filter) and with light filter (AM1.5G, UVC, and UVB/C blocking filter)*

Figure 2.14 exhibits the photocurrent density of the samples prepared with varying anodization times (see Table 2.1 for details). Generally, as already shown in a previous study[27], a direct correlation between anodization time and thickness of the nanotube layer was observed, while the diameter and crystallinity were similar. From the data reported in Figure 2.13, it was evidenced that by increasing the anodization time (from 1h to 5 h) the photocurrent value decreased (at open spectrum and with filters), and this could be potentially attributed to increased probabilities of charge recombination.

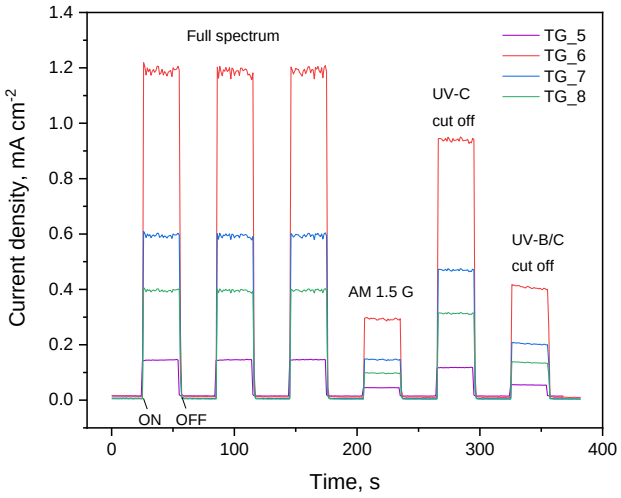

Figure 2.14 *Chronoamperometric measurements (1.136 V vs. RHE, 1 M KOH) for TiO_2NTs/Ti mesh anodized for different times using open UV-visible lamp spectrum (no light filter) and with light filter (AM1.5G, UVC, and UVB/C blocking filter)*

Figure 2.15 shows the effect of the electrolyte bath composition (see Table 2.2) on the photocurrent response of each sample. Notably, TG_11, anodized in diethylene glycol, exhibited a better photocurrent response when exposed to the full spectrum of the lamp and with the UV-C cut-off filter. Whereas, when the AM1.5G filter was applied to the lamp, the photocurrent response of TG_11 and TG_14 was the same. The sample TG_14, anodized in glycerol, showed instead the lowest photocurrent values when irradiated with the full spectrum of the lamp and the filtered light. The overall photocurrent responses of the samples were inferior to TG_3 photocurrent density, probably due to the different nanotubes conformations and superficial densities given by the electrolytes: hexagonal close-packed nanotubes conformation when using ethylene glycol based-electrolytes and spaced nanotubes when using glycerol and diethylene glycol as electrolytes[34].

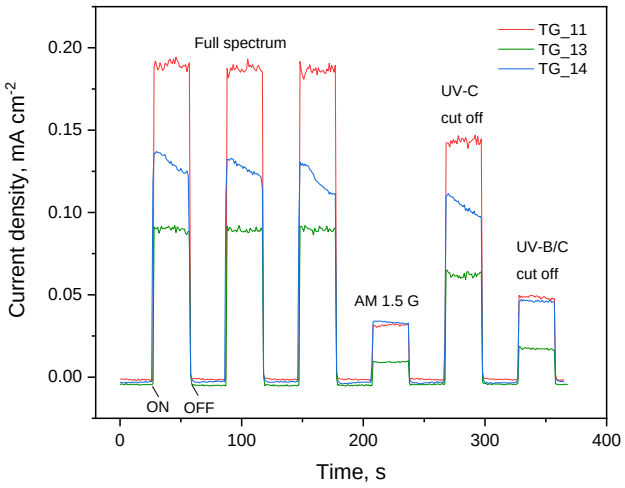

Figure 2.15 *Chronoamperometric measurements for TiO_2NTs/Ti mesh anodized with different electrolytes (1.136 V vs. RHE, 1 M KOH) using open UV-visible lamp spectrum (no light filter) and with light filter (AM1.5G, UVC, and UVB/C blocking filter)*

Table A2.4 in the annex section summarizes the average photocurrent density of the samples analysed.

Based on these results, it was possible to modulate the experimental parameters to create the best nanoarchitecture in terms of morphology and photoactivity. If not differently specified, from now all the reported TiO_2NTs samples were prepared using the following optimized conditions: 50 V, 1 h and ethylene glycol - 0.3 wt% NH_4F - 2 wt% H_2O as electrolyte bath.

2.4. Results: 3D vs. 2D hierarchical structures

As commented in the introduction, a catalyst with a well-defined hierarchical 3D structure, like the material studied in this thesis, can significantly boost the catalytic activity, using enhanced light harvesting properties and charge transportation and diminishing the scattering effect of liquid [38-44]. In this section, the TiO_2 nanotube arrays on Ti foil and Ti mesh electrodes, prepared in the

optimized conditions described previously, will be called respectively TiO_2NTs/Ti foil and TiO_2NTs/Ti mesh.

2.4.1. Structural and optical characterization

The phase composition of the catalysts was analysed using a Bruker D2 Phaser diffractometer equipped with a Ni β-filtered Cu-Kα radiation source in a 2θ range of 20° to 60°, using a scanning rate of 0.025° s^{-1}. Diffraction peaks were identified using the JCPDS database of reference compounds. The XRD analysis investigated the phase composition of the TiO_2NTs-based photocatalysts. The reported diffraction patterns in Figure 2.16 indicated that all diffraction peaks corresponded to the crystal structure of anatase TiO_2 (JCPDS 00-021-1272). These results suggested a high degree of crystallinity for TiO_2NTs on both Ti foil and mesh. No rutile or other titania phases were detected in either sample. The X-ray diffraction (XRD) patterns revealed the presence of metallic titanium, as a conductive metallic layer remained non-oxidized after the anodization process acting as an electron collector and maintaining the robustness of the electrode.

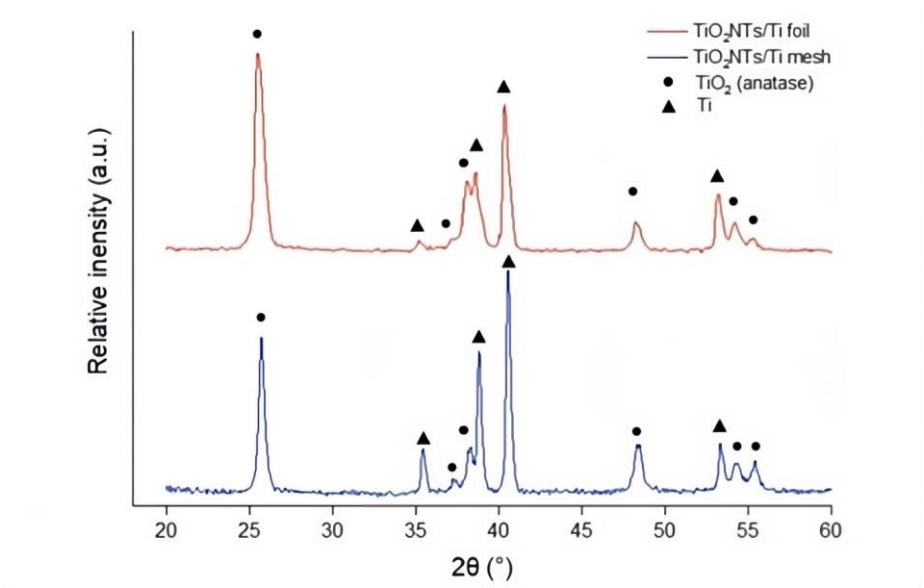

Figure 2.16 *XRD patterns of TiO_2NTs/Ti mesh and Ti foil electrodes.*

UV-Vis diffuse reflectance spectroscopy was used to characterize the optical absorption properties of the TiO_2NTs/Ti mesh and foil electrodes. A Thermo Fisher Evolution (220) spectrometer with an integrating sphere for solid samples was used to record ultraviolet–visible diffuse reflectance spectra, displayed in Figure 2.17. The TiO_2 P25 spectrum, a widely used reference, was also recorded. Both the mesh and foil profiles showed an absorption peak below 400 nm due to the typical UV response of TiO_2, correlated with the lowest energy charge transfer O^{2-}/Ti^{4+}. In addition, due to light diffraction and scattering caused by nanotube arrays and defects, it was visible an intense, broad light absorption in the visible region (between 500 and 1200 nm). Compared to the planar type TiO_2NTs/Ti film, this absorption band is broader for the TiO_2NTs deposited on Ti mesh because of a more complex nanoarchitecture in a 3D structure[28].

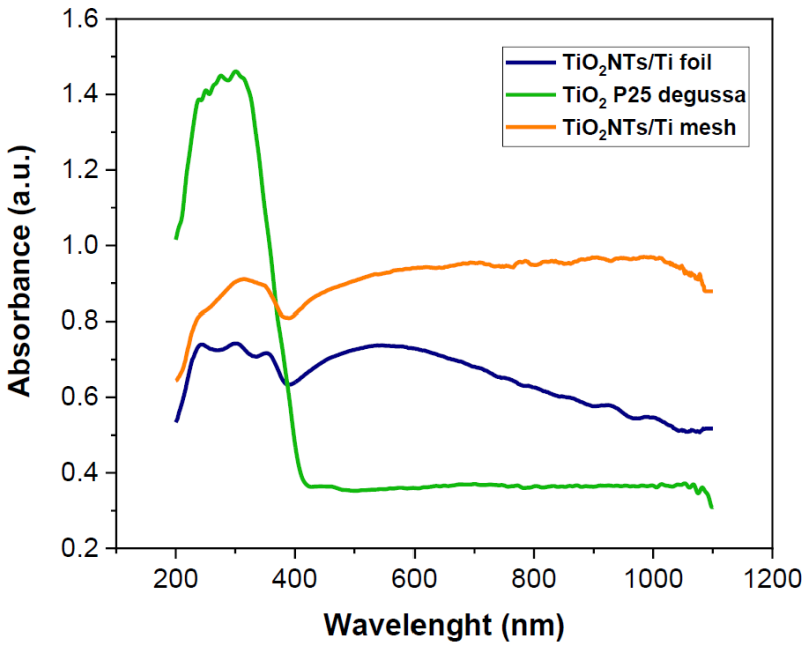

Figure 2.17 *UV-visible diffuse reflectance spectra of the TiO_2NTs/Ti mesh and TiO_2NTs/Ti foil electrodes. The spectrum of TiO_2 P25 (Evonik, former Degussa) is shown for comparison.*

2.4.2. Photo-electrochemical characterization

The photo-electrochemical characterization (CA, CV, EIS), was performed in a three-electrode cell, shown in Figure 2.18 made of two compartments, anodic and cathodic, separated by a Nafion N 324 membrane (supplied by Ion Power EU, Munich, Germany). A quartz window allowed the irradiation of the catalyst with a solar simulator (Lot-Oriel, 300W Xe lamp, Quantum Design Europe, Darmstadt, Germany). The TiO_2NTs-based catalyst (a square of dimensions 1 × 1 cm) acted as the working electrode, with a Pt foil (1 × 1 cm) as the counter electrode and an Ag/AgCl (KCl 3M) electrode (supplied by Amel S.r.l., Milano, Italy) as reference. A potentiostat/galvanostat (Autolab pgstat 204, Metrohm Italia S.r.l., Origgio, Varese, Italy) was used to apply the voltage.

The voltage values were converted to RHE using the formula in the annex section. All the experimental results were normalized, considering the difference in the geometrical area of the mesh with respect to the foil. The same cell was used for water photo-electrolysis experiments (see the scheme in Figure 2.19).

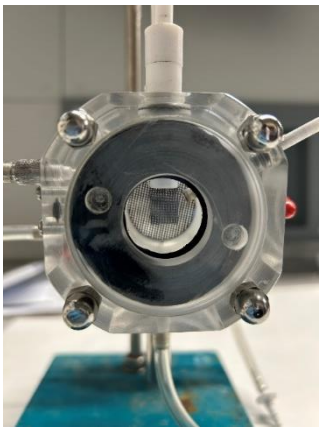

Figure 2.18 *Front-view of the photo-electrochemical cell used for photo-electrochemical characterization, in the centre the 1 cm^2 sample can be seen.*

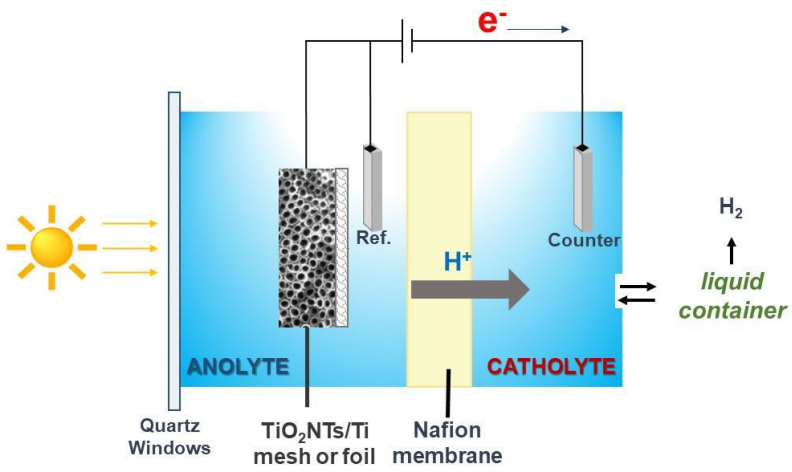

Figure 2.19 *Schematic side view of the reactor for water photo-electrolysis reaction*

Chronoamperometric (CA) experiments were performed in a 1 M KOH aqueous solution at the anode, and an aqueous solution of 0.5 M H_2SO_4 at +1.136 V vs. RHE to evaluate the photocurrent performance of TiO_2NTs/Ti mesh compared to TiO_2NTs/Ti foil. The tests included the application of ON/OFF illumination cycles under different cut-off light filters (specifically, AM1.5G, UV C blocking filter, and UV B/C blocking filter), as explained in 2.3.1. The results are shown in Figure 2.20.

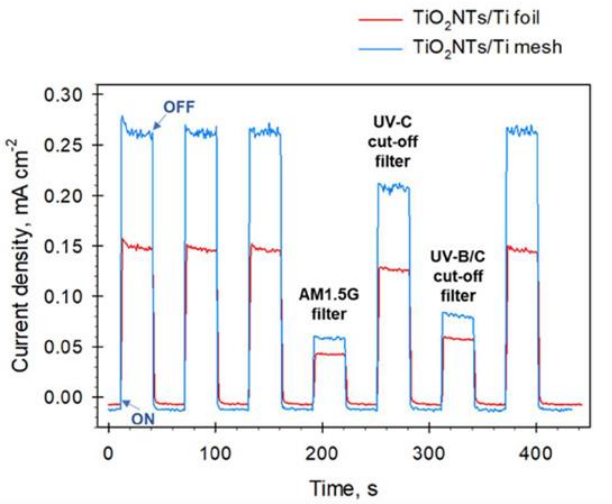

Figure 2.20 *Chronoamperometric profiles of TiO_2NTs/Ti mesh and TiO_2NTs/Ti foil (1.136 V vs. RHE, 1 M KOH) using open UV-visible lamp irradiation (no light filter) and with light filter (AM1.5G, UVC, and UVB/C blocking filter)*

The photocurrent density response of the TiO_2NTs/Ti mesh was 1.7 times higher than the TiO_2NTs/Ti foil response, under open spectrum conditions. This could be linked to reduced charge recombination. Both photo-electrodes remained active after filtering out parts B and C of the UV spectrum and simulating the standard terrestrial solar irradiation with the AM1.5G filter. On the contrary, the unstructured TiO_2 anatase films, made from TiO_2 powder, exhibited almost negligible photocurrent when subjected to the AM 1.5 G filter irradiation, in which the UV component is 4% [45, 46]. Thus, it can be stated that the TiO_2NTs nanostructure enabled a substantial reaction under visible light, as the reduction in photocurrent is not as significant as if charge separation only happened via the 4% UV component, as in the case of TiO_2 powder. In addition, it could be noticed that the baseline (i.e. dark values) was marginally lower for the mesh (less than 0.01 points) compared to the planar foil, due to the greater resistance of the woven wires of the gauze.

Cyclic Voltammetry (CV) measurements were performed at a scan rate of 10 mV s^{-1} with a continuous flow of N_2 (5 mL min^{-1}) and an aqueous solution of KOH 1

M and an aqueous solution of H_2SO_4 0.5 M, as the anolyte and catholyte, respectively.

Figure 2.21 illustrates the results of the cyclic voltammetry (CV) analysis carried out on TiO_2NTs/Ti mesh and foil. The peak intensities confirmed the higher photocurrent generated by the TiO_2NTs/Ti mesh compared to the foil as observed in the CA investigation. The water oxidation onset was observed at approximately 1.5 V vs. RHE for both electrodes. Additionally, there was an increase in the negative peak intensity with maximum values of about 0.6 V, not present in pure titania[47], and linked to the reaction of TiO_2 with the electron/proton that formed TiOOH on defective sites. Additionally, it should be noted that within the TiO_2NTs/Ti mesh, there was a decrease in the voltage gap between the onset of hydrogen and oxygen evolution reactions, when compared to TiO_2NTs/Ti foil. This gap fell from around 1.8 V to 1.2 V, indicating a significant reduction in the overpotential for water electrolysis.

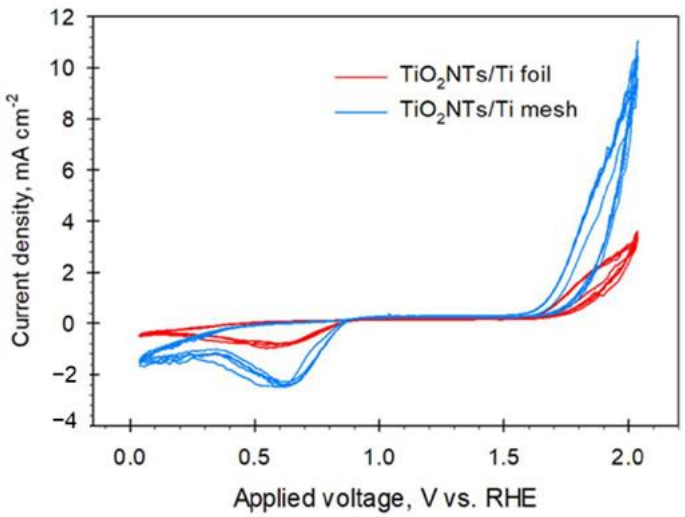

Figure 2.21 *Cyclic voltammetry profiles of TiO_2NTs/Ti mesh and TiO_2NTs/Ti foil in 1 M KOH. Data were normalized with respect to the surface area of the catalysts.*

2.4.3. Electrochemical Impedance Spectroscopy (EIS) measurements

Electrochemical Impedance Spectroscopy (EIS) is a powerful analytical technique used in electrochemistry to study the behaviour of electrochemical systems[48]. It involves the application of a small amplitude alternating current to a system over a range of frequencies. The response of the system in terms of impedance, a measure of opposition to the flow of an alternating current, is then analysed as a function of frequency[49]. This technique provides valuable insights into the electrochemical properties of materials, interfaces, and processes. EIS data are usually fitted, using a dedicated software, with an equivalent electrical circuit, which simulates the electrical behaviour of the studied system, constituted by electrical components (resistances, capacitances, etc.). Each of them gives quantitative information about the processes involved in the reaction, such as charge transfer resistance, double-layer capacitance, diffusion coefficients, and other characteristics of the system under investigation[50].

The measurements were conducted with Na_2SO_4 0.1 M as the electrolyte in both compartments, with a constant gas flow of N_2 (5 mL·min^{-1}). The EIS experimental parameters used consisted of a frequency range of $1 \cdot 10^5$ Hz to 0.01 Hz, an amplitude of 0.01 Vrms, and an applied potential varying from 0.9 to 1.5 V vs. RHE.

The data were obtained with and without light irradiation to better understand the influence of light on the electrochemical system and the subsequent charge transfer resistances. Zview® software (Scribner Associates, Southern Pines, NC, USA) was used to fit impedance data, using a two-constant fitting circuit shown in Figure 2.22. This circuit included a resistor, Rs, mostly related to the electrical connections of the cell and the distance between the system's working and reference electrodes. Rs was put in series with two parallel circuits, which consist of the resistors, Rct and Rct', and the constant phase elements, CPE and CPE'.

The CPE elements were related to the double layer. The resistors Rct and Rct' as two alternative charge transfer resistances were evaluated, whose existences were visible in the Bode graphs in Figure 2.23, in which two distinct peaks were present in all the experimental conditions employed. The high-frequency Rct' was attributed to charge transfer phenomena in the liquid phase (such as ionic migration at the electrode interface[28]), whereas the Rct (at low frequency) referred to the entire electrochemical process, including both half-reactions on working and counter electrodes. Figure 2.24 and Figure 2.25 display the Nyquist plots in dark conditions and under light irradiation at different applied potentials for TiO_2NTs/Ti foil, in (a), and for TiO_2NTs/Ti mesh, in (b). In the plots, the experimental data are represented by points, while the lines indicate the fitting curves processed through the software.

From these results, it can be noticed that the applied potential had a significant impact on the Rct at low frequency.

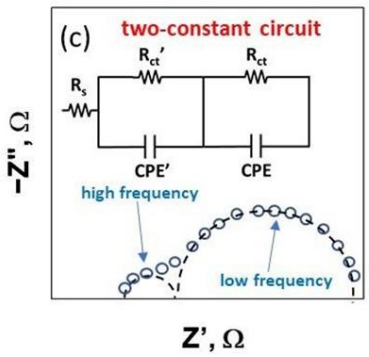

Figure 2.22 *Two-constant circuit model used to fit all the EIS data.*

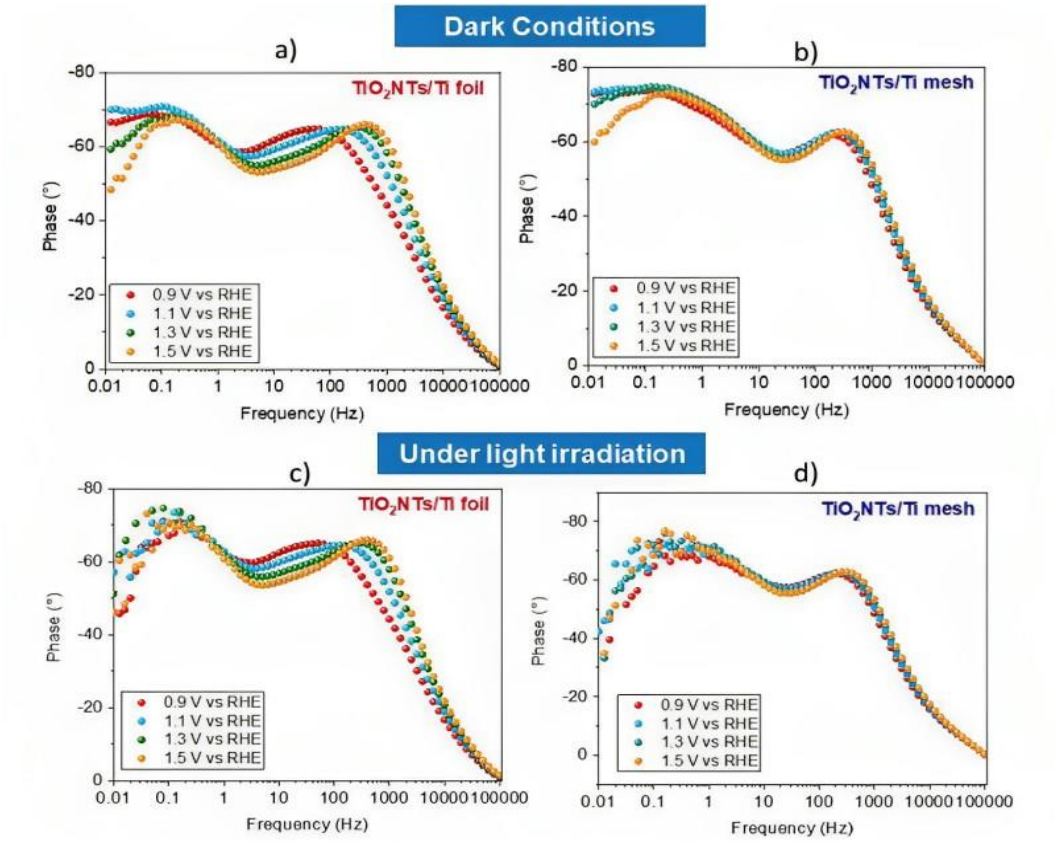

Figure 2.23 *Bode plots for TiO_2NTs/Ti foil and TiO_2NTs/Ti mesh in dark conditions* ***(a)*** ***(b)*** *and under light irradiation* ***(c)*** ***(d)*** *at different applied potentials*

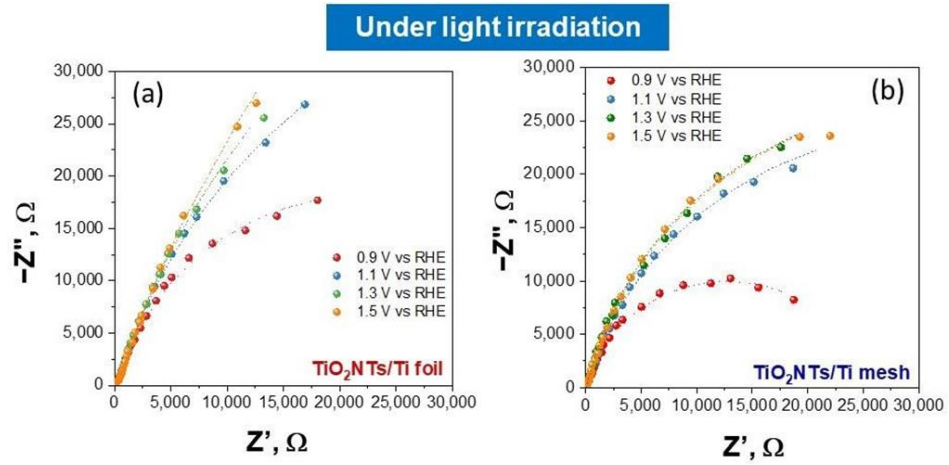

Figure 2.24 *Nyquist plots for TiO_2NTs/Ti foil (**a**) and TiO_2NTs/Ti mesh (**b**) measured under light irradiation applying different potential values. Filled circles are the experimental data, whereas the lines represent the fitting using the equivalent circuit model of Figure 2.21*

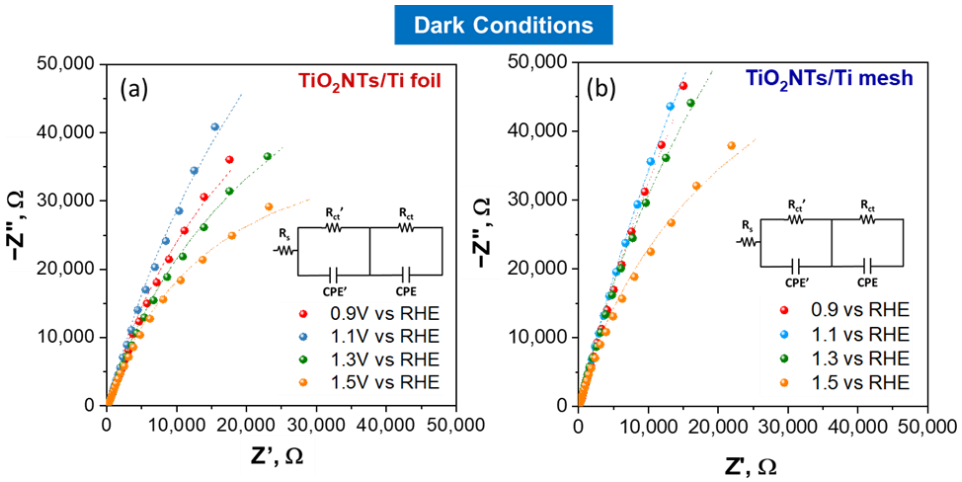

Figure 2.25 *Nyquist plots for TiO_2NTs/Ti foil (**a**) and TiO_2NTs/Ti mesh (**b**) measured in dark conditions applying different potential values. Filled circles are the experimental data, whereas the lines represent the fitting using the equivalent circuit model of Figure 2.21*

Figure 2.26 (a, b) reports the charge transfer resistances vs. applied voltage measured in the dark, for TiO_2NTs/Ti foil and TiO_2NTs/Ti mesh, whereas Figure 2.27 (a, b) reports the charge transfer resistances vs. applied potential under light irradiation. When exposed to light, TiO_2NTs/Ti mesh exhibited a significant decrease in resistance in comparison with TiO_2NTs/Ti foil. When switching from dark to light, the Rct value for the mesh decreased by one order of magnitude at

1.1 V vs. RHE. However, the effect was considerably less noticeable for the TiO_2NTs/Ti foil sample under the same conditions (Rct from $2.77 \cdot 10^5$ Ω in the dark to $1.02 \cdot 10^5$ Ω with light). The resistances linked to ionic migration were not significant in both cases, as seen by the high-frequency Rct' profiles vs the applied potential that did not reveal any noticeable variations in charge transfer resistance under light irradiation. The EIS results also pointed to quicker electron transportation along the nanotubes towards the metallic non-anodized component of the TiO_2NTs/Ti mesh (the internal metallic wires of the mesh). This was likely connected to the stresses due to the transition from a rounded to a planar state, which speeded up electron transfer at the interface.

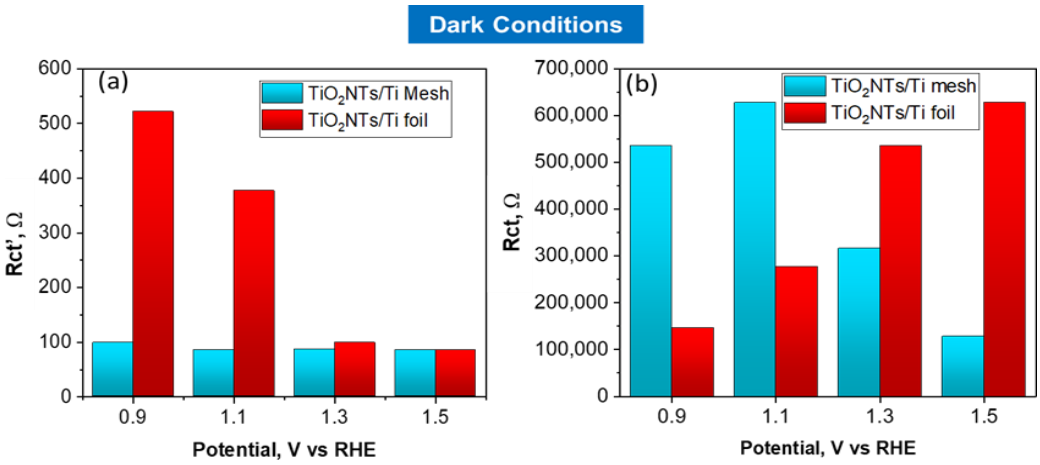

Figure 2.26 *Charge transfer resistances, Rct' (**a**) and Rct (**b**) obtained by fitting EIS data, vs. applied potential for TiO_2NTs/Ti foil and mesh electrodes in dark conditions*

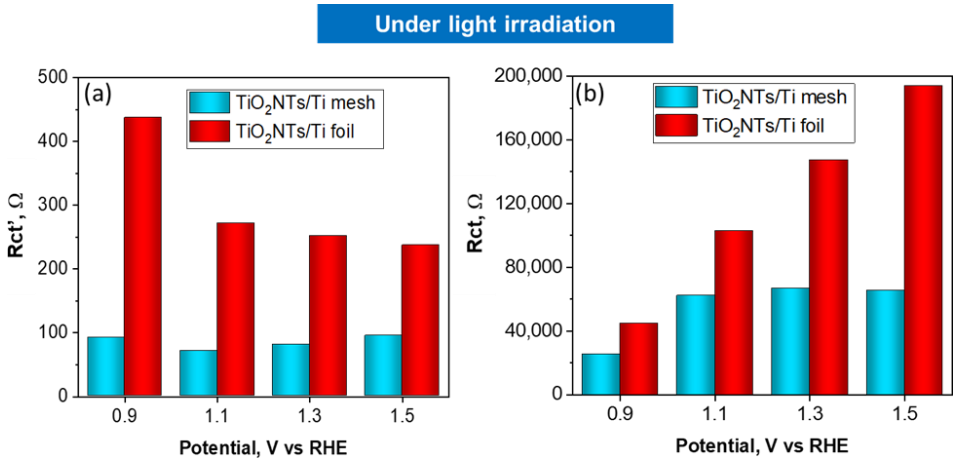

Figure 2.27 *Charge transfer resistances, Rct' (**a**) and Rct (**b**) obtained by fitting EIS data, vs. applied potential for TiO_2NTs/Ti foil and mesh electrodes under light irradiation*

All the values resulting from the EIS fitting are reported in Table A2.5 and Table A2.6 in the annex section.

2.4.4. Water splitting in PEC cell

Using the same system used for electrochemical characterization (described in section 2.4.2), photo-electrochemical water splitting experiments have been carried out to study the effect of the specific support on the catalytic performances. The reactor consisted of two compartments, which allowed the production of H_2 and O_2 in isolation. A Gas Chromatographer (7890A, Agilent Technologies Italia Spa) with a thermal conductivity detector (TCD) connected to the cathodic reservoir to determine the quantity of H_2 produced in the water photo electrolysis reaction. The experiments were conducted for 90 minutes with two different electrolytes: (i) Na_2SO_4 0.1 M in both compartments and (ii) H_2SO_4 0.5 M in the cathodic compartment and KOH 1 M in the anodic compartment.

In Table 2.3 is reported the hydrogen production rate and current density, (normalized taking into account the different geometrical areas of the mesh and

foil) for TiO_2NTs/Ti mesh and TiO_2NTs/Ti foil at three applied voltages (+2.036, +2.536 and +2.623 V vs. RHE). The formula for the calculation of H_2 production is reported in the annex.

Catalyst	Electrolyte *	Applied Potential (V vs. RHE)	H_2 production (μmol h^{-1} cm^{-2})	Average Current Density (mA cm^{-2})
TiO_2NTs/Ti mesh	Na_2SO_4	+2.623 V	24.4	5.08
	H_2SO_4-KOH	+2.036 V	9.4	3.03
	H_2SO_4-KOH	+2.536 V	182.3	18.69
TiO_2NTs/Ti foil	Na_2SO_4	+2.623 V	10.5	1.88
	H_2SO_4-KOH	+2.036 V	5.5	1.16
	H_2SO_4-KOH	+2.536 V	46.5	5.24

Table 2.3 *Hydrogen production, in μmol h^{-1} cm^{-2}, and average current density, in mA cm^{-2}, for TiO_2NTs/Ti foil and TiO_2NTs/Ti mesh samples at different applied voltages and different electrolytes.*

The structural properties of Ti meshes had a significant impact on performances at all pH values investigated. For TiO_2NTs/Ti mesh under neutral pH conditions (with 0.1 M Na_2SO_4), the rate of H_2 production and current density have more than doubled. In the presence of an acidic/basic electrolyte (in the cathode and anode compartments, respectively), this trend was reinforced, with the H_2 production and current density being more than three times higher for the TiO_2NTs/Ti mesh as compared to the foil under similar conditions. When the TiO_2NTs/Ti mesh was exposed to light, excited electrons in the valence band (VB) of TiO_2 moved to the conduction band (CB), generating electron-hole pairs. The defects, associated with the 3D geometry of the mesh, facilitated the transfer of photogenerated holes, thus promoting oxygen evolution. Meanwhile, protons and electrons migrated to the cathode side for hydrogen evolution. Additionally, the hierarchical porous and circular TiO_2 structure in the mesh provided a substantial

contact area and accelerated charge carrier transport when compared to the planar structure in the foil, which ultimately enhanced the performance of photo-electrocatalytic reactions[51, 52].

The synthesis conditions were individually tuned for TiO_2NTs film and mesh to obtain similar nanotubes with equivalent morphological structures (in terms of length and tube diameter), to be directly compared. Consequently, the significant increase in performance, concerning both photocurrent and photocatalytic water splitting, seen on the TiO_2NTs mesh when irradiated, could not be related to aspects such as a relevant change in the thickness or nanomorphology of the TiO_2NTs layer. Additionally, there were no variations in the composition or purity of the Ti substrate utilized for the growth of the TiO_2NTs layer. Besides, considering only the illumination of the geometrical area, the foil configuration should be more favourable. Thus, it might be assumed that the TiO_2NTs layer's characteristics were influenced by the curvature of the mesh wires. The CV data demonstrated that the performance of TiO_2NTs diverged from that of pure TiO_2 and that the overpotential of TiO_2NTs/Ti mesh in water electrolysis was lower than that of TiO_2NTs/Ti foil. This is likely due to the presence of more defective Ti sites, as suggested by CV and supported by diffuse reflectance spectra. Generally, defects lead to charge recombination, even if CA results showed an improved photocurrent.

The nanostructure of NTs facilitated the formation of defects that improved the efficiency of photocatalytic water splitting, without significantly affecting the charge separation enhancing the activity also in visible light, as demonstrated by CA tests.

Additionally, several studies can be found in the literature that primarily examined the impact of increased roughness or structural complexity on EIS plots. Significant variations in the low-frequency region of the EIS plot were noted for samples with disorder on a microscopic scale or which were mesoporous, as

evident from these experiments. Furthermore, a general deviation from ideal capacitive behaviour, directly linked to the degree of nanoscale irregularity/roughness of the electrode, was observed[53–56]. Although the direct correlation of a three-dimensional geometry on EIS has been scarcely investigated, this hypothesis has received strong support from a study of Dyatkin's research group[57] . They studied the impact of structural disorder on electric conductivity and capacitance for porous electrodes based on carbide-derived carbons and reported that annealing, and removing surface defects, reduced the capacitance and the ion movement into the pores, thus corroborating our observations. Other studies indicated that the intricate 3D porous structures had the potential to significantly enhance the capacitance, increasing the electric field present at the electrode's curvature and surface edges, as evidenced in conductive carbon nanotube electrodes[58, 59]. Another recent study evidenced, using CV and EIS analysis, the direct correlation between the surface defects in MnO_2 nanosheets, and the improved capacitance and decreased charge transfer resistances[60]. This confirmed the initial hypothesis. In addition, it could be possible that the charge transfer resistance, Rct', was linked to a higher rate of oxygen bubbles detaching from a round-shaped surface during water photo-electrolysis, compared to a planar surface.

2.5. Conclusions

This chapter was focused on synthesizing titanium dioxide nanotubes using titanium mesh as support, optimizing the controlled anodic oxidation synthesis. This technique allowed the adjustment of various parameters (electrolyte solution composition, anodization time, and anodization voltage) to obtain materials with different morphological, electrical, and optical properties, crucial factors in enhancing photoactivity.

Among the many parameters modified during anodic oxidation, specific combinations emerged as particularly promising in achieving a homogeneous

nanotube array with favourable optical properties. Specifically, an anodization potential of 50 V maintained for 1 hour in an ethylene glycol-based electrolyte, exhibited superior optical and photo-electrical properties. This combination of parameters not only contributed to enhancing the morphological and optical attributes of the nanotubes but also underlined the importance of this synthesis method in tailoring the material for a diverse range of applications. The EIS technique was employed to understand how different geometric substrates, in this case, mesh and foil, on which the TiO_2 nanotube arrays were grown, could influence the electronic properties and the photocatalytic behaviour of the material. The 3D structure of the nanotubes in the mesh, which enhances light absorption and facilitates faster electron transport along the nanotubes, significantly influenced the catalytic performance under illumination. In fact, in the same conditions, the production of H_2 and current density in water photo-electrolysis were over three times higher with the TiO_2NTs/Ti mesh compared to the foil. A good correspondence between EIS data and catalytic results was also noticed. In conclusion, the results of this study could give new insight into the process of designing an optimized photocatalytic material, correlating the peculiar substrate geometry with the electrical behaviour of the material and its photocatalytic activity.

2.6. References

[1] A. Fujishima, T. N. Rao, and D. A. Tryk, 'Titanium dioxide photocatalysis', *Journal of Photochemistry and Photobiology C: Photochemistry Reviews*, vol. 1, no. 1, pp. 1–21, Jun. 2000, doi: 10.1016/S1389-5567(00)00002-2.

[2] M. R. Al-Mamun, S. Kader, M. S. Islam, and M. Z. H. Khan, 'Photocatalytic activity improvement and application of UV-TiO_2 photocatalysis in textile wastewater treatment: A review', *J Environ Chem Eng*, vol. 7, no. 5, p. 103248, Oct. 2019, doi: 10.1016/j.jece.2019.103248.

[3] H. Anwer, A. Mahmood, J. Lee, K.-H. Kim, J.-W. Park, and A. C. K. Yip, ‘Photocatalysts for degradation of dyes in industrial effluents: Opportunities and challenges’, *Nano Res*, vol. 12, no. 5, pp. 955–972, May 2019, doi: 10.1007/s12274-019-2287-0.

[4] D. Ziental, B. Czarczynska-Goslinska, D. T. Mlynarczyk, A. Glowacka-Sobotta, B. Stanisz, T. Goslinski, and L. Sobotta, ‘Titanium Dioxide Nanoparticles: Prospects and Applications in Medicine’, *Nanomaterials*, vol. 10, no. 2, p. 387, Feb. 2020, doi: 10.3390/nano10020387.

[5] O. CARP, ‘Photoinduced reactivity of titanium dioxide’, *Progress in Solid State Chemistry*, vol. 32, no. 1–2, pp. 33–177, 2004, doi: 10.1016/j.progsolidstchem.2004.08.001.

[6] K. Nakata and A. Fujishima, ‘TiO_2 photocatalysis: Design and applications’, *Journal of Photochemistry and Photobiology C: Photochemistry Reviews*, vol. 13, no. 3, pp. 169–189, Sep. 2012, doi: 10.1016/j.jphotochemrev.2012.06.001.

[7] A. Wold, ‘Photocatalytic properties of titanium dioxide (TiO_2)’, *Chemistry of Materials*, vol. 5, no. 3, pp. 280–283, Mar. 1993, doi: 10.1021/cm00027a008.

[8] H. Eidsvåg, S. Bentouba, P. Vajeeston, S. Yohi, and D. Velauthapillai, ‘TiO_2 as a Photocatalyst for Water Splitting—An Experimental and Theoretical Review’, *Molecules*, vol. 26, no. 6, p. 1687, Mar. 2021, doi: 10.3390/molecules26061687.

[9] H. P. Maruska and A. K. Ghosh, ‘Photocatalytic decomposition of water at semiconductor electrodes’, *Solar Energy*, vol. 20, no. 6, pp. 443–458, 1978, doi: 10.1016/0038-092X(78)90061-0.

[10] X. Chen and S. S. Mao, ‘Titanium Dioxide Nanomaterials: Synthesis, Properties, Modifications, and Applications’, *Chem Rev*, vol. 107, no. 7, pp. 2891–2959, Jul. 2007, doi: 10.1021/cr0500535.

[11] Y. Gai, J. Li, S.-S. Li, J.-B. Xia, and S.-H. Wei, ‘Design of Narrow-Gap TiO_2 : A Passivated Codoping Approach for Enhanced Photoelectrochemical Activity’, *Phys Rev Lett*, vol. 102, no. 3, p. 036402, Jan. 2009, doi: 10.1103/PhysRevLett.102.036402.

[12] H. N. C. Dharma, J. Jaafar, N. Widiastuti, H. Matsuyama, S. Rajabsadeh, M. H. D. Othman, M. A. Rahman, N. N. M. Jafri, N. S. Suhaimin, A. M. Nasir, and N. H. Alias, ‘A Review of Titanium Dioxide (TiO_2)-Based Photocatalyst for Oilfield-Produced Water Treatment’, *Membranes (Basel)*, vol. 12, no. 3, p. 345, Mar. 2022, doi: 10.3390/membranes12030345.

[13] B. Wang, S. Shen, and S. S. Mao, ‘Black TiO_2 for solar hydrogen conversion’, *Journal of Materiomics*, vol. 3, no. 2, pp. 96–111, Jun. 2017, doi: 10.1016/j.jmat.2017.02.001.

[14] C. Ampelli, C. Genovese, F. Tavella, M. Favaro, S. Agnoli, G. Granozzi, S. Perathoner, and G. Centi, ‘Assembling of TiO_2 Nanotube Photoelectrodes with Enhanced Visible Properties for a Sustainable Production of H_2’, *Chem Eng Trans*, vol. 43, pp. 667–672, 2015.

[15] D. Zhang and S. Dong, ‘Challenges in band alignment between semiconducting materials: A case of rutile and anatase TiO_2’, *Progress in Natural Science: Materials International*, vol. 29, no. 3, pp. 277–284, Jun. 2019, doi: 10.1016/j.pnsc.2019.03.012.

[16] R. Passalacqua, C. Ampelli, S. Perathoner, and G. Centi, ‘Anodically Formed TiO_2; Thin Films: Evidence for a Multiparameter Dependent

Photocurrent-Structure Relationship', *Nanoscience and Nanotechnology Letters*, vol. 4, no. 2, pp. 142–148, Feb. 2012, doi: 10.1166/nnl.2012.1303.

[17] W.-G. Yang, F.-R. Wan, Q.-W. Chen, J.-J. Li, and D.-S. Xu, 'Controlling synthesis of well-crystallized mesoporous TiO_2 microspheres with ultrahigh surface area for high-performance dye-sensitized solar cells', *J Mater Chem*, vol. 20, no. 14, p. 2870, 2010, doi: 10.1039/b923105f.

[18] S. Ding, J. S. Chen, Z. Wang, Y. L. Cheah, S. Madhavi, X. Hu, and X. W. Lou, 'TiO_2 hollow spheres with large amount of exposed (001) facets for fast reversible lithium storage', *J. Mater. Chem.*, vol. 21, no. 6, pp. 1677–1680, 2011, doi: 10.1039/C0JM03650A.

[19] P. Periyat, N. Leyland, D. E. McCormack, J. Colreavy, D. Corr, and S. C. Pillai, 'Rapid microwave synthesis of mesoporous TiO_2 for electrochromic displays', *J Mater Chem*, vol. 20, no. 18, p. 3650, 2010, doi: 10.1039/b924341k.

[20] W. Ho, J. C. Yu, and S. Lee, 'Synthesis of hierarchical nanoporous F-doped TiO_2 spheres with visible light photocatalytic activity', *Chemical Communications*, no. 10, p. 1115, 2006, doi: 10.1039/b515513d.

[21] Y. Kondo, H. Yoshikawa, K. Awaga, M. Murayama, T. Mori, K. Sunada, S. Bandow, and S. Iijima, 'Preparation, Photocatalytic Activities, and Dye-Sensitized Solar-Cell Performance of Submicron-Scale TiO_2 Hollow Spheres', *Langmuir*, vol. 24, no. 2, pp. 547–550, Jan. 2008, doi: 10.1021/la702157r.

[22] H. Li, Z. Bian, J. Zhu, D. Zhang, G. Li, Y. Huo, H. Li, and Y. Lu, 'Mesoporous Titania Spheres with Tunable Chamber Stucture and Enhanced Photocatalytic Activity', *J Am Chem Soc*, vol. 129, no. 27, pp. 8406–8407, Jul. 2007, doi: 10.1021/ja072191c.

[23] K. Indira, U. K. Mudali, T. Nishimura, and N. Rajendran, ‘A Review on TiO_2 Nanotubes: Influence of Anodization Parameters, Formation Mechanism, Properties, Corrosion Behavior, and Biomedical Applications’, *J Bio Tribocorros*, vol. 1, no. 4, p. 28, Dec. 2015, doi: 10.1007/s40735-015-0024-x.

[24] C. A. Grimes, ‘Synthesis and application of highly ordered arrays of TiO_2 nanotubes’, *J Mater Chem*, vol. 17, no. 15, p. 1451, 2007, doi: 10.1039/b701168g.

[25] P. Xiao, B. B. Garcia, Q. Guo, D. Liu, and G. Cao, ‘TiO_2 nanotube arrays fabricated by anodization in different electrolytes for biosensing’, *Electrochem commun*, vol. 9, no. 9, pp. 2441–2447, Sep. 2007, doi: 10.1016/j.elecom.2007.07.020.

[26] F. Tavella, C. Ampelli, L. Frusteri, F. Frusteri, S. Perathoner, and G. Centi, ‘Development of photoanodes for photoelectrocatalytic solar cells based on copper-based nanoparticles on titania thin films of vertically aligned nanotubes’, *Catal Today*, vol. 304, pp. 190–198, Apr. 2018, doi: 10.1016/j.cattod.2017.08.036.

[27] C. Ampelli, F. Tavella, S. Perathoner, and G. Centi, ‘Engineering of photoanodes based on ordered TiO_2 -nanotube arrays in solar photo-electrocatalytic (PECa) cells’, *Chemical Engineering Journal*, vol. 320, pp. 352–362, Jul. 2017, doi: 10.1016/j.cej.2017.03.066.

[28] T. Saboo, F. Tavella, C. Ampelli, S. Perathoner, C. Genovese, B. C. Marepally, L. Veyre, E. A. Quadrelli, and G. Centi, ‘Water splitting on 3D-type meso/macro porous structured photoanodes based on Ti mesh’, *Solar Energy Materials and Solar Cells*, vol. 178, pp. 98–105, May 2018, doi: 10.1016/j.solmat.2018.01.007.

[29] J. Kapusta-Kołodziej, A. Chudecka, and G. D. Sulka, ‘3D nanoporous titania formed by anodization as a promising photoelectrode material’, *Journal of Electroanalytical Chemistry*, vol. 823, pp. 221–233, Aug. 2018, doi: 10.1016/j.jelechem.2018.06.014.

[30] Z. Liu, Q. Zhang, T. Zhao, J. Zhai, and L. Jiang, ‘3-D vertical arrays of TiO_2 nanotubes on Ti meshes: Efficient photoanodes for water photoelectrolysis’, *J Mater Chem*, vol. 21, no. 28, p. 10354, 2011, doi: 10.1039/c1jm11072a.

[31] T. Shichi and K. Katsumata, ‘Development of Photocatalytic Self-cleaning Glasses Utilizing Metal Oxide Nanosheets’, *Journal of The Surface Finishing Society of Japan*, vol. 61, no. 1, pp. 30–35, 2010, doi: 10.4139/sfj.61.30.

[32] D. Fattakhova-Rohlfing, A. Zaleska, and T. Bein, ‘Three-Dimensional Titanium Dioxide Nanomaterials’, *Chem Rev*, vol. 114, no. 19, pp. 9487–9558, Oct. 2014, doi: 10.1021/cr500201c.

[33] D. Gong, C. A. Grimes, O. K. Varghese, W. Hu, R. S. Singh, Z. Chen, and E. C. Dickey, ‘Titanium oxide nanotube arrays prepared by anodic oxidation’, *J Mater Res*, vol. 16, no. 12, pp. 3331–3334, Dec. 2001, doi: 10.1557/JMR.2001.0457.

[34] S. Yoriya and C. A. Grimes, ‘Self-assembled anodic TiO_2 nanotube arrays: electrolyte properties and their effect on resulting morphologies’, *J. Mater. Chem.*, vol. 21, no. 1, pp. 102–108, 2011, doi: 10.1039/C0JM02421J.

[35] K. Indira, U. K. Mudali, T. Nishimura, and N. Rajendran, ‘A Review on TiO_2 Nanotubes: Influence of Anodization Parameters, Formation Mechanism, Properties, Corrosion Behavior, and Biomedical Applications’, *J Bio Tribocorros*, vol. 1, no. 4, p. 28, Dec. 2015, doi: 10.1007/s40735-015-0024-x.

[36] S. Yoriya, ‘Effect of Inter-Electrode Spacing on Electrolyte Properties and Morphologies of Anodic TiO_2 Nanotube Array Films’, *Int J Electrochem Sci*, vol. 7, no. 10, pp. 9454–9464, Oct. 2012, doi: 10.1016/S1452-3981(23)16210-9.

[37] J. M. Macak and P. Schmuki, ‘Anodic growth of self-organized anodic TiO_2 nanotubes in viscous electrolytes’, *Electrochim Acta*, vol. 52, no. 3, pp. 1258–1264, Nov. 2006, doi: 10.1016/j.electacta.2006.07.021.

[38] L. De Pasquale, F. Tavella, V. Longo, M. Favaro, S. Perathoner, G. Centi, C. Ampelli, and C. Genovese, ‘The Role of Substrate Surface Geometry in the Photo-Electrochemical Behaviour of Supported TiO_2 Nanotube Arrays: A Study Using Electrochemical Impedance Spectroscopy (EIS)’, *Molecules*, vol. 28, no. 8, p. 3378, Apr. 2023, doi: 10.3390/molecules28083378.

[39] Z. Liu, Q. Zhang, T. Zhao, J. Zhai, and L. Jiang, ‘3-D vertical arrays of TiO_2 nanotubes on Ti meshes: Efficient photoanodes for water photoelectrolysis’, *J Mater Chem*, vol. 21, no. 28, p. 10354, 2011, doi: 10.1039/c1jm11072a.

[40] J. Kapusta-Kołodziej, A. Chudecka, and G. D. Sulka, ‘3D nanoporous titania formed by anodization as a promising photoelectrode material’, *Journal of Electroanalytical Chemistry*, vol. 823, pp. 221–233, Aug. 2018, doi: 10.1016/j.jelechem.2018.06.014.

[41] W. He, J. Qiu, F. Zhuge, X. Li, J.-H. Lee, Y.-D. Kim, H.-K. Kim, and Y.-H. Hwang, ‘Advantages of using Ti-mesh type electrodes for flexible dye-sensitized solar cells’, *Nanotechnology*, vol. 23, no. 22, p. 225602, Jun. 2012, doi: 10.1088/0957-4484/23/22/225602.

[42] M. Sihor, S. Gowrisankaran, A. Martaus, M. Motola, G. Mailhot, M. Brigante, and O. Monfort, ‘Anodic TiO_2 Nanotube Layers for Wastewater

and Air Treatments: Assessment of Performance Using Sulfamethoxazole Degradation and N_2O Reduction', *Molecules*, vol. 27, no. 24, p. 8959, Dec. 2022, doi: 10.3390/molecules27248959.

[43] E. Konstantinova, T. Savchuk, O. Pinchuk, E. Kytina, E. Ivanova, L. Volkova, V. Zaitsev, A. Pavlikov, and E. Elizarova, 'Photoelectron Properties and Organic Molecules Photodegradation Activity of Titania Nanotubes with Cu_xO Nanoparticles Heat Treated in Air and Argon', *Molecules*, vol. 27, no. 22, p. 8080, Nov. 2022, doi: 10.3390/molecules27228080.

[44] Y. Zhang, Y. Li, J. Yu, B. Sun, and H. Shang, 'A Heterostructure Photoelectrode Based on Two-Dimensional Covalent Organic Framework Film Decorated TiO_2 Nanotube Arrays for Enhanced Photoelectrochemical Hydrogen Generation', *Molecules*, vol. 28, no. 2, p. 822, Jan. 2023, doi: 10.3390/molecules28020822.

[45] C. Ampelli, F. Tavella, C. Genovese, S. Perathoner, M. Favaro, and G. Centi, 'Analysis of the factors controlling performances of Au-modified TiO_2 nanotube array based photoanode in photo-electrocatalytic (PECa) cells', *Journal of Energy Chemistry*, vol. 26, no. 2, pp. 284–294, Mar. 2017, doi: 10.1016/j.jechem.2016.11.004.

[46] C. Ampelli, C. Genovese, R. Passalacqua, S. Perathoner, and G. Centi, 'A gas-phase reactor powered by solar energy and ethanol for H_2 production', *Appl Therm Eng*, vol. 70, no. 2, pp. 1270–1275, Sep. 2014, doi: 10.1016/j.applthermaleng.2014.04.013.

[47] M. Zukalova, M. Bousa, Z. Bastl, I. Jirka, and L. Kavan, 'Electrochemical Doping of Compact TiO_2 Thin Layers', *The Journal of Physical Chemistry C*, vol. 118, no. 45, pp. 25970–25977, Nov. 2014, doi: 10.1021/jp504457v.

[48] A. J. Bard and L. R. Faulkner, *Electrochemical Methods: Fundamentals and Applications, 2nd Edition*. Wiley, 2001.

[49] J. R. MacDonald, *Impedance Spectroscopy*. Wiley-Interscience, 1987.

[50] E. Barsoukov and J. R. MacDonald, *Impedance Spectroscopy: Theory, Experiment, and Applications (2nd ed.)*. Wiley-Interscience, 2005.

[51] S. Chandrasekaran, J. S. Chung, E. J. Kim, and S. H. Hur, 'Advanced Nano-Structured Materials for Photocatalytic Water Splitting', *Journal of Electrochemical Science and Technology*, vol. 7, no. 1, pp. 1–12, Mar. 2016, doi: 10.5229/JECST.2016.7.1.7.

[52] R. Passalacqua, C. Ampelli, S. Perathoner, and G. Centi, 'Anodically Formed TiO_2; Thin Films: Evidence for a Multiparameter Dependent Photocurrent-Structure Relationship', *Nanoscience and Nanotechnology Letters*, vol. 4, no. 2, pp. 142–148, Feb. 2012, doi: 10.1166/nnl.2012.1303.

[53] E. F. Douglass Jr., P. F. Driscoll, D. Liu, N. A. Burnham, C. R. Lambert, and W. G. McGimpsey, 'Effect of Electrode Roughness on the Capacitive Behavior of Self-Assembled Monolayers', *Anal Chem*, vol. 80, no. 20, pp. 7670–7677, Oct. 2008, doi: 10.1021/ac800521z.

[54] J. K. Eckhardt, S. Burkhardt, J. Zahnow, M. T. Elm, J. Janek, P. J. Klar, and C. Heiliger, 'Understanding the Impact of Microstructure on Charge Transport in Polycrystalline Materials Through Impedance Modelling', *J Electrochem Soc*, vol. 168, no. 9, p. 090516, Sep. 2021, doi: 10.1149/1945-7111/ac1cfe.

[55] Z. Kerner and T. Pajkossy, 'On the origin of capacitance dispersion of rough electrodes', *Electrochim Acta*, vol. 46, no. 2–3, pp. 207–211, Nov. 2000, doi: 10.1016/S0013-4686(00)00574-0.

[56] T. PAJKOSSY, ‘Impedance spectroscopy at interfaces of metals and aqueous solutions — Surface roughness, CPE and related issues’, *Solid State Ion*, vol. 176, no. 25–28, pp. 1997–2003, Aug. 2005, doi: 10.1016/j.ssi.2004.06.023.

[57] B. Dyatkin and Y. Gogotsi, ‘Effects of structural disorder and surface chemistry on electric conductivity and capacitance of porous carbon electrodes’, *Faraday Discuss.*, May 2014, doi: 10.1039/C4FD00048J.

[58] J. Vatamanu, Z. Hu, D. Bedrov, C. Perez, and Y. Gogotsi, ‘Increasing Energy Storage in Electrochemical Capacitors with Ionic Liquid Electrolytes and Nanostructured Carbon Electrodes’, *J Phys Chem Lett*, vol. 4, no. 17, pp. 2829–2837, Sep. 2013, doi: 10.1021/jz401472c.

[59] E. Paek, A. J. Pak, and G. S. Hwang, ‘Curvature Effects on the Interfacial Capacitance of Carbon Nanotubes in an Ionic Liquid’, *The Journal of Physical Chemistry C*, vol. 117, no. 45, pp. 23539–23546, Nov. 2013, doi: 10.1021/jp408085w.

[60] P. Gao, P. Metz, T. Hey, Y. Gong, D. Liu, D. D. Edwards, J. Y. Howe, R. Huang, and S. T. Misture, ‘The critical role of point defects in improving the specific capacitance of δ-MnO_2 nanosheets’, *Nat Commun*, vol. 8, no. 1, p. 14559, Feb. 2017, doi: 10.1038/ncomms14559.

2.7. Annex

2.7.1. Materials

Ti gauze 80mesh was purchased from Alfa Aesar.

All the chemicals used in the synthesis routes were purchased from Sigma-Aldrich and used without any further purification.

Nafion membrane was obtained from Ion power and was pre-treated before use.

2.7.2. Mathematical methods

- The potential values referred to the Ag/AgCl electrode are converted to RHE using the following formula:

$$E_{(RHE)} = E_{(Ag/AgCl)} + 0.059\ pH + 0.21$$

- The hydrogen production in the water-splitting tests is the following:

$$H_2\ production\ (\mu mol \cdot\ h^{-1}cm^{-2}) = \frac{[H_2](\%vol.) \cdot Q\ (L/min)}{V_m\ (L/mol)} \cdot \frac{1}{60\ \cdot A(cm^2)}\ 10^6$$

$[H_2]$ = % of hydrogen detected by the GC

Q = flow rate

V_m = molar volume of a gas at room temperature and pressure

A = active area of the catalyst

2.7.3. Results

Sample	Average photocurrent density (mA cm^{-2})			
	Full spectrum	AM1.5G filter	UV-C cut-off filter	UV-B/C cut-off filter
TG_1	0.543	0.123	0.426	0.166
TG_2	1.014	0.234	0.828	0.350
TG_3	1.190	0.293	0.940	0.407
TG_4	0.492	0.145	0.366	0.176
TG_5	0.146	0.045	0.118	0.055
TG_6	1.190	0.293	0.940	0.407
TG_7	0.595	0.147	0.470	0.204
TG_8	0.397	0.098	0.313	0.136
TG_11	0.186	0.032	0.143	0.049
TG_13	0.090	0.009	0.062	0.017
TG_14	0.119	0.033	0.104	0.046

Table A2.4 *Average photocurrent density in mA cm^{-2} of all samples with irradiation of the full spectrum of the lamp (300 W Xe-arc lamp) and with different filters applied on the lamp (AM1.5G, UV-C cut-off filter, UV-B/C cut off filter)*

DARK CONDITIONS								
	0.9 V vs. RHE		1.1 V vs. RHE		1.3 V vs. RHE		1.5 V vs. RHE	
	TiO_2NTs/Ti foil	TiO_2NTs/Ti mesh	TiO_2NTs/Ti foil	TiO_2NTs/Ti mesh	TiO_2NTs/Ti foil	TiO_2NTs/Ti mesh	TiO_2NTs/Ti foil	TiO_2NTs/Ti mesh
Rs (Ω)	3.83	3.47	3.57	3.34	3.47	3.28	3.34	3.23
Rct' (Ω)	521.0	98.0	376	84.5	98.1	85.3	84.5	84.9
CPE' (F)	2.57E-05	3.40E-05	2.11E-05	3.28E-05	3.41E-05	2.93E-05	3.27E-05	2.80E-05
Rct (Ω)	1.46E+05	5.35E+05	2.77E+05	6.27E+05	5.35E+05	3.16E+05	6.27E+05	1.28E+05
CPE (F)	9.46E-05	6.74E-05	6.79E-05	6.08E-05	6.76E-05	6.43E-05	6.11E-05	6.29E-05

Table A2.5 *EIS fitting circuit values of experimental data for TiO_2NTs/Ti foil and mesh without illumination at different applied potentials*

UNDER LIGHT ILLUMINATION								
	0.9 V vs. RHE		1.1 V vs. RHE		1.3 V vs. RHE		1.5 V vs. RHE	
	TiO_2NTs/Ti foil	TiO_2NTs/Ti mesh	TiO_2NTs/Ti foil	TiO_2NTs/Ti mesh	TiO_2NTs/Ti foil	TiO_2NTs/Ti mesh	TiO_2NTs/Ti foil	TiO_2NTs/Ti mesh
Rs (Ω)	3.87	3.53	3.57	3.52	3.58	3.44	3.57	3.35
Rct' (Ω)	436.8	91.6	271.7	70.9	251.3	81.0	236.6	94.8
CPE' (F)	1.74E-04	8.44E-05	5.71E-05	7.42E-05	5.76E-05	6.10E-05	4.36E-05	5.73E-05

Rct (Ω)	4.48E+04	2.53E+04	1.02E+05	6.22E+04	1.47E+05	6.66E+04	1.94E+05	6.53E+04
CPE (F)	3.73 E-04	3.04 E-04	3.38E-04	3.43E-04	3.79E-04	2.87E-04	4.15E-04	2.84E-04

Table A2.6 *EIS fitting circuit values of experimental data for TiO_2NTs/Ti foil and mesh with illumination at different applied potential*

3. Plasmonic metal enhanced TiO_2 nanotubes for H_2 production

3.1. Introduction and scope of the chapter

Titanium dioxide is a very versatile semiconductor material, but the fast charge carriers' recombination rate and the high band gap energy (3.18 eV for anatase, 3.03 eV for rutile), cause the absorption of only a small fraction of the solar spectrum in the ultraviolet (UV) light (3-4%), resulting in a poor overall catalytic efficiency [1, 2]

As mentioned in Chapter 1, the functionalization with noble metals (Au, Ag, Ru, Pd and Pt) and some transition metals (Ni, Fe, and Cu) is an effective method to extend the photoactivity to the visible range and decrease the charge carrier recombination[3, 4]. When a particular metal is coupled to a semiconductor, Schottky junctions form at the interface between them[5]. This phenomenon is defined as an electron flow from the semiconductor to the metal, causing the semiconductor's energy bands to bend. Due to the Schottky barrier formation, the metals could trap electrons, reducing the electron-hole pair recombination and as a consequence improve the photoactivity of metal-loaded TiO_2.

Some metals used as co-catalysts show significant absorption in the visible region, as well as scattering and local plasmon resonance phenomena (LSPR) strongly influenced by the size and nanostructure of the particles themselves[4]. LSPR is a well-known effect that consists in the coordinated and coherent oscillations of delocalized electrons within a spherical metal particle, induced by the electromagnetic field of incident light at the interface when the metal nanostructure is considerably smaller than both the electron mean free path and the wavelength of the incident light [6 11]

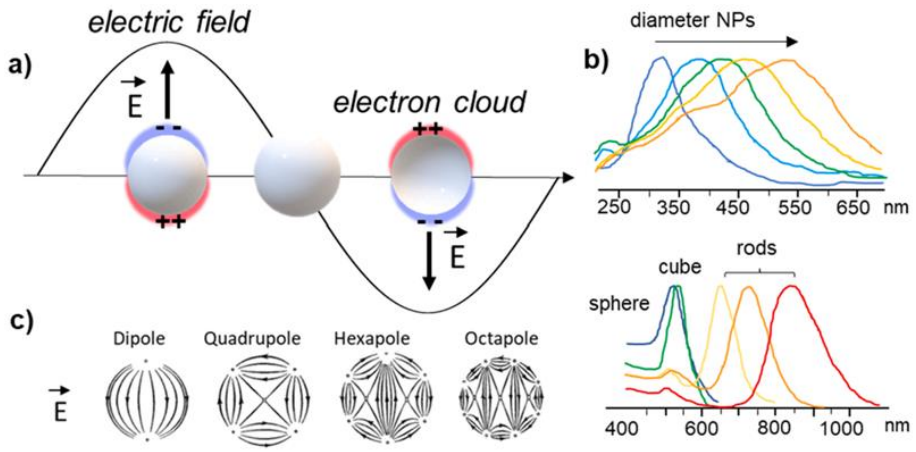

Figure 3.1 *(**a**) Localized surface plasmon resonance on spherical NPs, (**b**) depending on the absorption spectrum from the characteristics of metal nanoparticles (NPs), and (**c**) influence of the local field by the arrangement of the metal NPs. Reproduced with permission from ref.*[7]

The decay of these plasmonic oscillations gives rise to several effects and pathways associated with both non-radiative and radiative routes, evidenced in Figure 3.2[7].

Two primary decay mechanisms are evident: (a) photothermal localized heating and (b) activation of molecules at the (photo)catalyst surface via resonant-generated charge carriers, facilitated by both direct and indirect pathways. After the generation of local electric fields around a nanoparticle, energetic charge carriers, often referred to as "hot" carriers, are produced[3]. These carriers undergo evolution through processes like electron-electron scattering and electron-phonon scattering, with the latter contributing to the heating of the catalyst nanoparticles (NPs). Indirect transfer can occur if the excited electrons possess sufficient energy to reach the unoccupied energy levels of the adsorbate. An alternative mechanism involves the excitation of charge carriers from the metal NPs to the vacant orbitals of the adsorbate. Non-radiative damping, also known as *Landau* damping, results in a non-thermal distribution of hot carriers. This distribution can scatter charge carriers with appropriate energy along the indirect pathway through adsorbate states, leading to the generation of non-thermal vibrational excitation in a bond

within the adsorbate. In the direct transfer pathway instead, a localized surface plasmon resonance (LSPR)-induced electron excitation occurs, moving from occupied to unoccupied orbitals within the metal–molecule or metal–adsorbate complex[7]. Charge carriers excited by LSPR can actively participate in the activation of adsorbed molecules at the surface through either vibrational or electronic means.

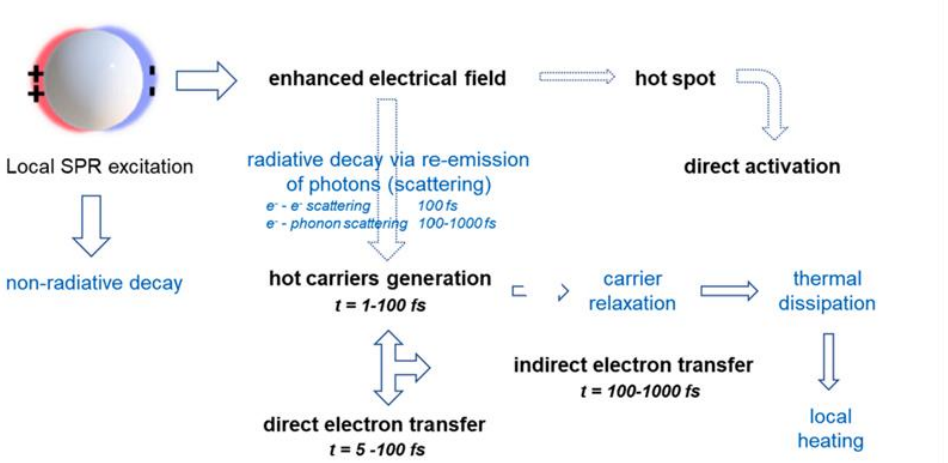

Figure 3.2 *Pathways of decay post-local SPR activation, indicating the significant factors related to (photo)catalytic activation and their corresponding time scale. Reproduced with permission from ref.* [7]

Figure 3.3 summarizes the different effects caused by the deposition of plasmonic metal NPs on titanium dioxide[6]. This method of material modification is a versatile strategy to significantly enhance the performances and expand the range of applications.

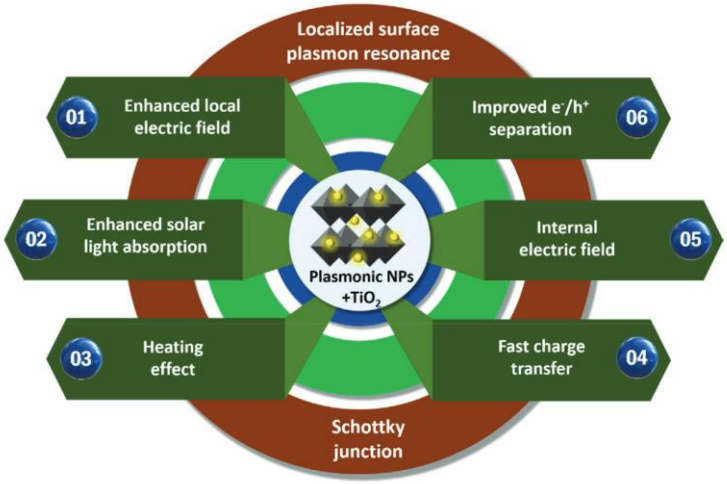

Figure 3.3 *Different effects given by the introduction of nanoparticles in the titanium dioxide substrate. Reproduced with permission from ref.*[6]

The aim of this chapter is thus the modification of the nanostructured titania through the incorporation of metal NPs with proven LSPR behaviour (Au, Ag, Cu, Pd) to understand how plasmonic metals may affect the performances in photocatalytic applications [8–10]. The chapter investigates the integration of these NPs in the 3D hierarchical nanostructure of TiO_2 mesh (prepared by optimized conditions) to study the synergy between the local SPR phenomenon with the structure of nanotubes in the mesh (that enhances both light harvesting and photogeneration of charge carriers, as widely discussed in cap.2). The photoelectrodes were prepared by using different methodologies and fully characterized. Then, the effect of the metal on the performances in two different key H_2 production reactions (water photo-electrolysis and ethanol photo-dehydrogenation) was studied. The ethanol photo-conversion is usually performed in a system based on slurry or batch liquid phase. So, to investigate how gas-phase conditions can influence the performances in terms of productivity and selectivity, two different configurations of the cell, gas-phase and liquid-phase, were employed in the tests and discussed.

3.2. Experimental Section

3.2.1. Synthesis of Metal-doped TiO_2 based materials

For the deposition of all metal NPs, if not expressly specified, TiO_2 nanotubes on Ti meshes (TiO_2NTs/Ti) prepared in optimized conditions, were used as substrates. All details about the synthesis procedure are described in Chapter 2.

3.2.1.1. Gold nanoparticles deposition

Photodeposition

In this method, the meshes were immersed in an aqueous precursor solution ($HAuCl_4 \cdot 3H_2O$) for 30 minutes, and subsequently subjected to light irradiation of a UV-visible lamp (Lot-Oriel 300 W Xe-Arc lamp) for variable times (1, 5, or 15 minutes) under N_2 gas flow [11]. The samples were then annealed for two hours at 200°C, with a heating rate of 2°C/min. The concentration of the $HAuCl_4 \cdot 3H_2O$ solution was calculated to obtain 0,5 wt% of Au NPs deposited on the titania substrate.

Table 3.1 summarizes the experimental conditions and the names of the as-prepared samples.

Sample	Irradiation time (min)	Annealing	Calculated wt% of Au NPs
Au 1	1	200°C for 2 h	0.5
Au 2	5	200°C for 2 h	0.5
Au 3	15	200°C for 2 h	0.5

Table 3.1 *Photodeposition experimental conditions for Au-based samples*

Electrodeposition

Au NPs were electrodeposited on the TiO_2NTs/Ti mesh using two distinct methods.

In the first electrodeposition technique[12] the TiO_2NTs/Ti mesh, acting as working electrode, was placed in a two-electrode cell made in Teflon with a standard Pt electrode as the counter. Using an aqueous solution of $HAuCl_4 \cdot 3H_2O$, 0.1 mM in deionized (DI) water, at room temperature, the electrodeposition was carried out by applying a potential of -70 V with an Agilent potentiostat (Agilent E3612A), at different electrodeposition times.

Four different samples were prepared: Au 4, Au 5, Au 6, and Au 7, with deposition times of 30, 15, 30 and 45 minutes, respectively.

Only the Au 4 sample was annealed in air at 450°C for 1 h (2°C/min), sonicated in acetone for 10 minutes and annealed again in air at 450 °C for 1 h (2°C/min), to determine the effect of an annealing treatment post electrodeposition. Table 3.2 provides a summary of the operating conditions.

Sample	Applied Voltage (V)	Time (min)	Annealing
Au 4	-70	30	Yes
Au 5	-70	15	No
Au 6	-70	30	No
Au 7	-70	45	No

Table 3.2 *Electro-deposition experimental conditions for Au-based samples*

The second electrodeposition method[13] has been performed in $HAuCl_4 \cdot 3H_2O$, 1 mM in deionized (DI) water, in a three-electrodes set-up, with the sample as the working electrode, a standard Ag/AgCl (KCl 3M) electrode as reference electrode, a Pt wire as the counter electrode, using a 2049 AMEL potentiostat-galvanostat. The Au NPs were deposited onto the TiO_2NTs/Ti mesh using a pulsed potential approach, with cathodic pulses of 50 ms and a short-circuit pulse of 100 ms at room temperature. These conditions have been used over three samples: Au 8, Au 9, and Au 10 with the respective cathodic bias of -1.613, -2.613, -3.613 V vs. RHE (-2 V, −3 V and -4 V vs. Ag/AgCl). The same number of on/off cycles have been applied to each sample (500). In Table 3.3 are reported the experimental conditions.

Sample	Applied Voltage (V vs. RHE)	Time ON (s)	Time OFF (s)	N. cycles
Au 8	-1.613	0.050	0.100	500
Au 9	-2.613	0.050	0.100	500
Au 10	-3.613	0.050	0.100	500

Table 3.3 *Electro-deposition experimental conditions for Au-based samples*

3.2.1.2. Silver nanoparticles deposition

Photodeposition

The photodeposition technique[2] has been conducted by dipping the sample for 30 minutes at room temperature, in a 1 M HCl solution, in distilled water, in a 0.1 M $AgNO_3$ solution and finally in distilled water. This cycle was performed three times. Afterwards, the sample was irradiated with a 300 W lamp for 10 minutes, to reduce Ag^+ ions to metallic Ag species. The details are reported in Table 3.4.

Sample	Time 1 (HCl 1 M)	Time 2 (Distilled water)	Time 3 ($AgNO_3$)	Time 4 (Distilled water)	Nr. Cycles	Irradiation time
Ag 2	30 min	30 min	30 min	30 min	3	10 min

Table 3.4 *Photodeposition experimental conditions for Ag-based samples*

Electrodeposition

The pulsed electrodeposition[14] has been performed using an $AgNO_3$ 1 mM and $NaNO_3$ 10 mM aqueous electrolyte, at room temperature, with a three-electrode cell configuration, using the sample as the working electrode, a Pt wire as counter electrode and a standard Ag/AgCl (KCl 3M) electrode as reference, and a 2049 AMEL as potentiostat-galvanostat. Two samples were synthesized using different current densities while the charge deposited on both samples was fixed at 600 $mC \cdot cm^{-2}$. Ag-deposition experimental conditions are summarized in Table 3.5.

Sample	Current ($mA \cdot cm^{-2} \cdot pulse^{-1}$)	Time On (s)	Time off (s)	Cycles	Total charge ($mC \cdot cm^{-2}$)
Ag 1	-15	0.1	0.3	400	600
Ag 3	-5	0.1	0.3	1200	600

Table 3.5 *Electro-deposition experimental conditions for Ag-based samples*

3.2.1.3. Copper-Copper (I) oxide nanoparticles electrodeposition

The Cu/Cu_2O NPs were deposited on the TiO_2NTs/Ti mesh substrate by electrodeposition[15] with the same three-electrode cell configuration used for the Ag electro-deposition. The electrolyte used was a solution of Cu(II) acetate 0.02 M and Na acetate 0.08 M, the pH was fixed at 5 by the addition of acetic acid. The deposition time was set at 30 minutes. Operating potential and temperature conditions are summarized in Table 3.6.

Sample	Applied Voltage (V vs RHE)	Time (min)	Temperature (°C)
Cu 1	+0.255	30	25
Cu 2	+0.38	30	60

Table 3.6 *Electrodeposition experimental conditions for Cu-based samples*

3.2.1.4. Palladium photodeposition

The deposition of Pd was carried out on the TiO_2NTs/Ti mesh not annealed (sample called Pd1) [16]. In detail, 0.5 mL of an aqueous solution of H_2PdCl_4 5 mM was added to 10 mL of distilled water. This solution was stirred using a magnetic stirrer. The sample was placed in the solution for 10 minutes with stirring and then irradiated for 10 minutes with a lamp (Lot Oriel, 300 W Xe arc lamp) using two filters, VIS-IR blocking filter and UVB/C blocking filter (LSZ177 and LSZ179), to obtain a total irradiance of the lamp of 0.9 $mW \cdot cm^{-2}$. After irradiation, the sample was washed with water and annealed at 450°C for 3 hours at a heating rate of 2°C/min.

3.2.2. Set-up for water photo-electrolysis

The PEC reactor used for water photo-electrolysis tests is the same described in detail in section 2.4, as well as the analytical system used for the H_2 production quantification.

The experiments were conducted for 90 minutes, under light irradiation, applying a potential of +2.623 V vs. RHE (+2 V vs. Ag/AgCl) and using as electrolyte Na_2SO_4 0.1 M in both anodic and cathodic compartments.

3.2.3. Set-up for ethanol photo-dehydrogenation: gas vs. liquid cell

The photo-electrochemical cell used for the catalytic tests was designed to be used in different configurations, nominally in gas-phase configuration (GP) and liquid-phase configuration (LP). It was made in plexiglass, with two separate compartments, anodic and cathodic, and incorporated a quartz window and several inlets and outlets for gases and/or liquids that could be easily replaced to work with the desired configuration (LP or GP) (see Figure 3.4). The main advantage of this design consisted in the possibility of using the cell in a two or three-electrode configuration, by simply operating on the different inlets/outlets. A picture of the cell during a gas phase test is shown in Figure 3.5: during these tests the cell was used in a two-electrode configuration, using a squared Pt foil with an area of 1 cm^2 as the counter-electrode, and the TiO_2NTs/Ti mesh – based photoanode in contact with a Pt wire as the working electrode.

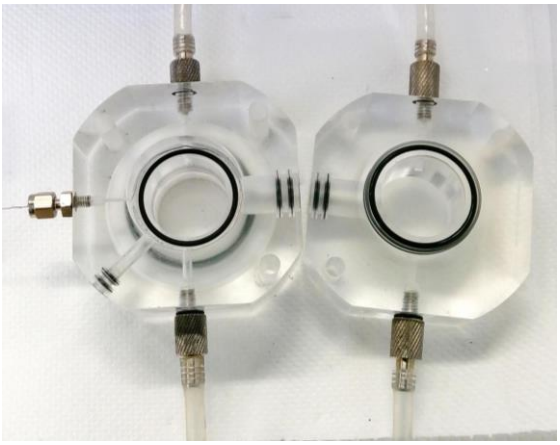

Figure 3.4 *View of the two compartments of the cell, the anodic compartment on the left, with the Pt wire to ensure the contact with the electrode, and the cathodic compartment on the right.*

Figure 3.5 *Side view of the cell, irradiated by the lamp, during a gas-phase test.*

A schematic picture of the entire GP setup is shown in Figure 3.6: a hot plate was used for heating a solution of ethanol in D.I. water (20% vol) at the constant temperature of 60°C. The temperature was monitored with a thermocouple. A nitrogen flow of 20 mL min^{-1} was used to push the headspace of the flask to the anode compartment of the cell. A solar simulator, (300 W Xe-Arc lamp Lot Oriel, Quantum design) irradiated the cell, and it was placed at 5 cm from the quartz window of the cell. A peristaltic pump and an external tank containing 40 mL of an aqueous solution of 0.050 M H_2SO_4 were used to circulate the electrolyte in the cathode chamber. An additional flow of 20 mL min^{-1} was used to send the H_2

produced in the cathode to a micro-GC for determination (Pollution micro-GC). The reacted vapours of the anodic compartment were then later collected in an absorber, containing 1 mL of an aqueous solution of 0.005 M H_2SO_4, placed inside an ice bath. The collected products were analysed with GC-MS (Thermo-Fisher Trace 1310) and with Ionic Chromatography (Metrohm 940 Vario).

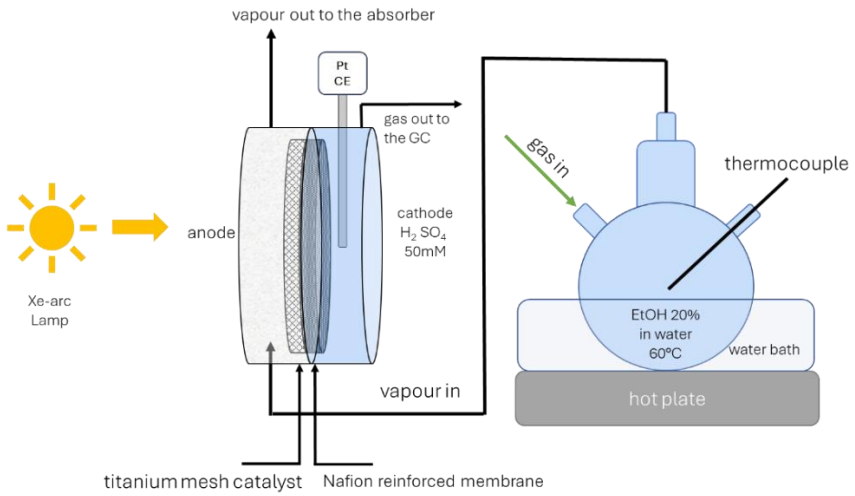

Figure 3.6 *Scheme of the gas-phase set-up*

In liquid-phase configuration (Figure 3.7) the solution of ethanol 20%, vol. in D.I. water, stored in a tank, was sent directly in liquid phase to the anode chamber through a peristaltic pump, without the use of the external hot plate to form the gas phase. The same peristaltic pump was also used for the circulation of the electrolyte (0.050 M H_2SO_4) in the cathode chamber. The cathode gas products were analysed using the micro-GC, whilst the anode products were sampled every 30 minutes, diluted 1:1 with ultrapure water and analysed using Ionic Chromatography and GC-MS.

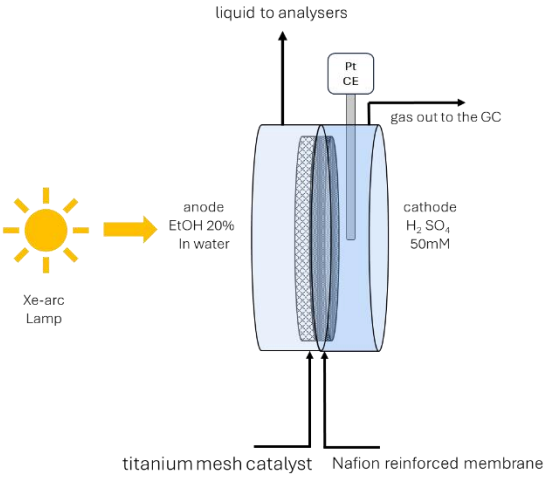

Figure 3.7 *Scheme of the liquid-phase set-up*

3.2.4. Assembly of the electrode for photo-dehydrogenation experiments

The assembly of the electrode materials was a critical step for the effective functioning of the electrocatalytic cell: it was important to ensure an optimal adherence of the distinct layers to facilitate mass transport and reduce electrical loss. The assembly procedure of the electrode was the same for both gas-phase and liquid-phase configurations.

Specifically, the photoanode and a Nafion® N324 membrane were cut into circular shapes with a diameter of 36 mm and subsequently brought into contact, positioning the "anodic" section of the membrane facing the photoanode. To apply additional pressure, a silicon disk of the same diameter was included in the assembly. The assembly, consisting of 1) the photoanode, 2) the membrane, and 3) the silicon disk, was enveloped in waxed paper and subjected to hot pressing at 130°C for 90 seconds. Subsequently, the silicon disk was easily removed, and

the resulting electrode (consisting of the photoanode and the membrane) was integrated into the electrocatalytic cell for subsequent testing.

3.3. Results and discussion

The following section will report the characterization and productivity results for the TiO_2 NTs/Ti mesh samples functionalized with Au, Ag and Cu, Pd using the methodologies summarized in Table 3.7. Henceforth these samples (Ag3, Au7, Cu2 and Pd1) will be named Ag/TiO_2, Au/TiO_2, Cu/TiO_2 and Pd/TiO_2 respectively.

Sample	Preparation method
Ag3	Pulsed electrodeposition
Au7	Electrodeposition
Cu2	Electrodeposition
Pd1	Photodeposition

Table 3.7 *List of the metal-modified catalysts, with the preparation method*

3.3.1. Characterization

The catalysts were characterized using different techniques to determine the optical, morphological, and structural properties by using the equipment already described in Chapter 2.

3.3.1.1. Structural and optical characterization

The optical properties were evaluated by UV-visible Diffuse Reflectance Spectroscopy and the spectra obtained for Ag/TiO_2, Au/TiO_2, Pd/TiO2 and Cu/TiO_2 are reported in Figures 3.8 and 3.9. The spectrum of TiO_2NTs/Ti mesh (in black) is also reported as a reference showing the typical peak in the UV range (below 400 nm), associated with the lowest energy charge transfer of O^{2-}/Ti^{4+} and a broad absorption peak in the visible region, attributed to the structure of the nanotube TiO_2 arrays. The incorporation of silver (green line) and gold (orange

line) nanoparticles was correlated with peaks in the visible region (see Figure 3.9) specifically centred at around 450 nm and linked to the LSPR phenomena[16].Copper modified sample spectrum (red line) was characterized by two bands in the visible region, between 400 nm and 600 nm, attributed to SPR with a series of small resonance bands present in the ultraviolet region. It is noteworthy that for Cu/TiO_2, the first observed peak was blue-shifted compared to Ag NPs (435 nm vs. 453 nm)[17], probably due to a different particle size of copper oxide with respect to silver. It is generally recognized that the position and the intensity of the SPR peak strongly depend on the size and concentration of metal nanoparticles[18–20]. For Pd/TiO_2, as well as Au/TiO_2 and Cu/TiO_2, there was a reduction in the band in the UV region, possibly due to the coverture of the surface. Metals on the surface can produce a shielding effect, causing a decrease in the UV band[21].

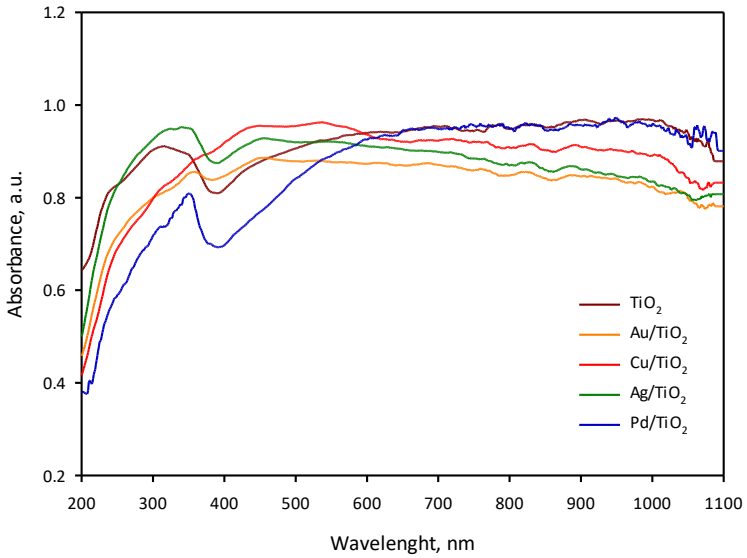

Figure 3.8 *UV-visible reflectance spectra of Cu/TiO_2, Ag/TiO_2, Au/TiO_2, and Pd/TiO_2 compared to bare TiO_2 (NTs on Ti mesh). The different samples are represented by the different line colours.*

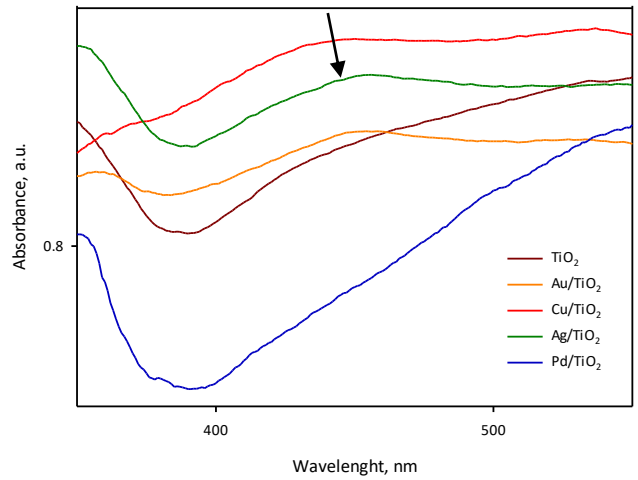

Figure 3.9 *Magnification of the UV-visible diffuse reflectance spectra, focusing on the peak at around 450 nm. The different samples are represented by the different line colours.*

The phase composition of the catalysts was analysed by XRD to exclude the presence of impurities and the diffractograms are reported in Figure 3.10. The peaks observed at 2θ values of 24.8 (101), 37.3 (103), 47.6 (200), 53.5 (105) and 55.1 (211) were assigned to the TiO_2 anatase phase (JCPDS Card no. 21-1272) and the peaks at 2θ values of 35(100), 38(002), 40.3(101) and 53.1(102) to metallic Ti (JCPDS Card no. 44-1294).

For the Ag/TiO_2 sample, the peaks at 2θ values of 38.1 (111) and 44.3 (200) were assigned to metallic Ag (JCPDS Card No. 04-0783) while the peak relative to Ag (111) was superimposed on the (002) plane of Ti and couldn't be distinguished.

For the Au/TiO_2 sample, the peaks at 2θ values of 38.3 and 44.5 could be assigned to the (111) and (200) plane of gold (JCPDS Card no. 04-0784), even if it was barely distinguishable from the background, probably related to the low concentration of gold.

In the case of the Cu/TiO_2 sample the presence of Cu (I) was confirmed, it was observed the presence of peaks at 2θ angles 36.4° and 42.3° assigned to Cu_2O

(JCPDS card No. 78–2076). No peaks ascribed to metallic Cu are observed (2θ angles of 43.9°, 51.0° JCPDS Card No. 003–1018). In the case of the Pd/TiO_2 XRD pattern, there are no peaks detected related to Pd nanoparticles (2θ = 40.1° (111) and 46.6° (200), JCPDS card no. 46-1043), consistent with the work from Liu et al.[16] that evidenced no Pd peaks in their catalysts, because of the small percentage of the metal.

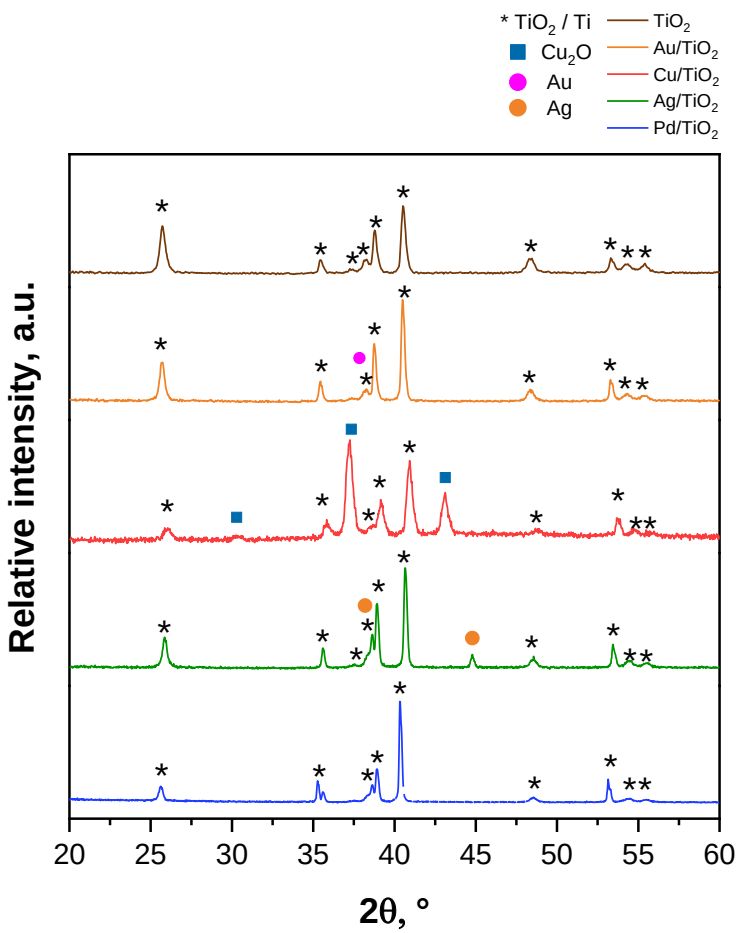

Figure 3.10 *XRD patterns of the metal-modified TiO_2 catalysts*

The morphology of the TiO_2-based catalysts was analysed by SEM-EDX, and the results are reported in Figures 3.11, 3.12 and 3.13 for Ag, Au, and Cu TiO_2

samples. Only titanium and oxygen atoms were detected together with the metal in all cases. EDX analysis showed a percentage of Ag and Au atoms of 1.8% and 3.8% respectively. The EDX analysis for the Cu/TiO_2 sample, revealed instead a high percentage of copper, 37.5%, probably due to the preparation method.

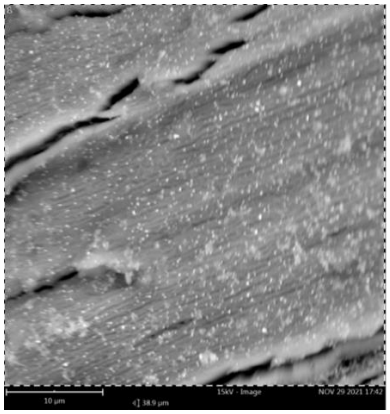

Element Number	Element Symbol	Element Name	Weight Concentration	Error
22	Ti	Titanium	60.1	0.3
8	O	Oxygen	38.1	1.5
47	Ag	Silver	1.8	2.3

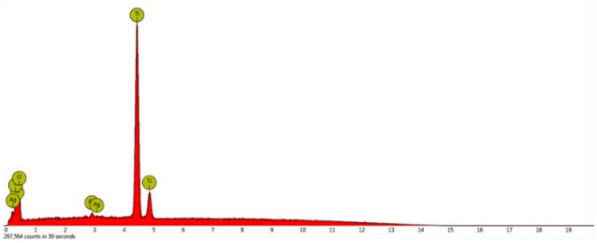

Figure 3.11 *SEM EDX analysis of Ag/TiO_2 sample.*

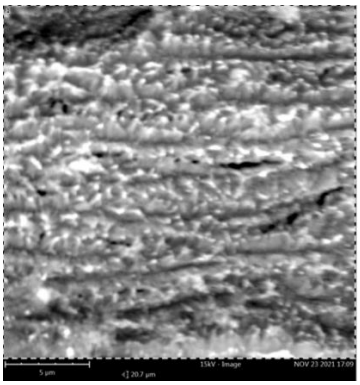

Element Number	Element Symbol	Element Name	Weight Concentration	Error
22	Ti	Titanium	42.2	0.3
8	O	Oxygen	53.4	0.8
79	Au	Gold	3.8	1.3

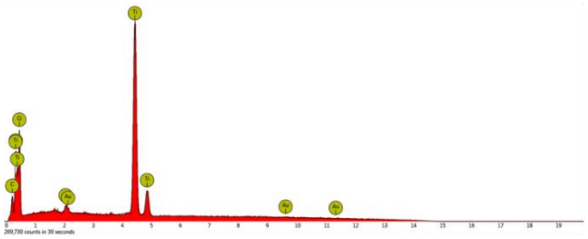

Figure 3.12 *SEM-EDX analysis of Au/TiO_2 sample.*

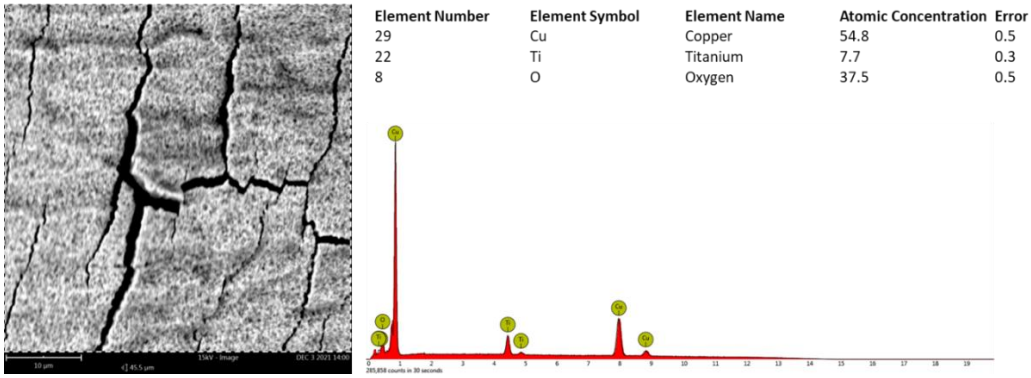

Figure 3.13 *SEM-EDX analysis of Cu/TiO_2 sample.*

3.3.1.2. Photo-electrochemical characterization

In Figure 3.14 are reported the chronoamperometric profiles, for Au, Ag and Cu TiO_2-based samples compared with bare titania nanotube arrays (TiO_2 NTs/Ti mesh) obtained at a potential of +1.136 V vs RHE (+0.1 V vs Ag/AgCl) in a solution of KOH 1 M. The tests were carried out by applying ON/OFF illumination cycles in the presence of cut-off light filters (i.e., AM1.5 G, UVC blocking filter, UVB/C blocking filter) in the cell described in paragraph 2.3.1.

The photocurrent was stable under several ON/OFF light cycles for all samples. In full spectrum, apart from the gold-modified catalyst that showed a photocurrent similar to TiO_2, a lowering of the signal was observed for copper and silver-modified samples probably due to the formation of larger particles. With the application of the AM1.5G filter, the photocurrent for Cu/TiO_2 and Ag/TiO_2 was still high in percentage with respect to the raw photocurrent (e.g. the photocurrent generated under the full spectrum irradiation). as evidenced by Table 3.8.

Sample	AM1.5G solar simulator filter	UVC blocking filter	UVC/B blocking filter
TiO_2	24.8%	76.6%	33.9%
Au/TiO_2	16.7%	71.9%	22.8%
Cu/TiO_2	64.5%	77.2%	17.6%

Ag/ TiO_2	33.6%	64.5%	41.3%
Pd/TiO_2	23.1%	81.2%	31.7%

Table 3.8 *Photocurrent density percentage with respect to the raw photocurrent generated under full spectrum irradiation for all tested photoelectrodes.*

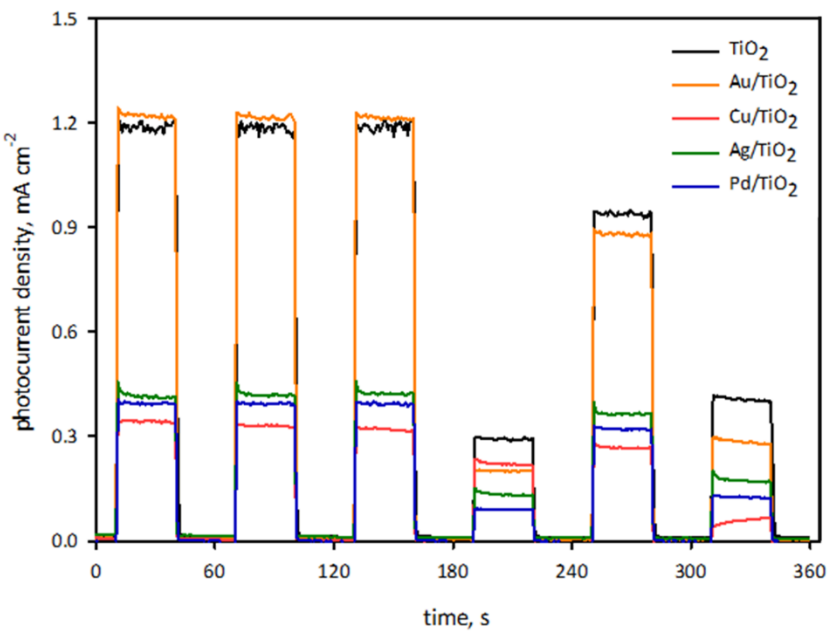

Figure 3.14 *Chronoamperometric measurements (+1.136 V vs RHE, KOH 1M electrolyte) for TiO_2, and Au, Cu, Ag and Pd on TiO_2NTs /Ti mesh samples.*

3.3.2. H_2 production in water photo-electrolysis

The results obtained for the TiO_2-modified electrodes in the water photo-electrolysis reaction are presented in Table 3.9 and compared with the TiO_2NTs/Ti mesh results.

Catalyst	**H_2 production ($\mu mol\ h^{-1}\ cm^{-2}$)**	**Average Current Density ($mA\ cm^{-2}$)**	**Faradaic Efficiency (%)**
TiO_2	24.4	5.08	33

Au/TiO_2	42.0	4.82	47
Ag/TiO_2	87.6	7.92	59
Cu/TiO_2	45.1	4.16	58

Table 3.9 *Hydrogen production and average current density for the samples tested in water photo-electrolysis*

The results showed strong improvements in the H_2 productivity values for all the catalysts modified with metal nanoparticles, confirming the role of NPs in the enhancement of the photoactivity of titania. By using Cu/TiO_2 sample, an increase in H_2 production of 85% but a 20% decrease in the photocurrent was observed, evidencing an indirect correlation between current and catalytic performances. A similar behaviour was noticed with the Au/TiO_2 catalyst, even if much less pronounced (the decrease in photocurrent is about 5%). This particular response has already been observed by Tavella et al.[22], who reported that the presence of Cu_2O/Cu NPs on titania nanotubes thin films did not promote the photocurrent generation, but enhanced the H_2 production, likely due to Cu NPs acting as electron trapping centres, thus no direct relationship could be observed between these two behaviours.

The H_2 production of the Ag/TiO_2 sample was more than three times higher (87.6 μmol h^{-1} $cm^{-2)}$ compared to the bare TiO_2, showing also the highest current density, probably as a consequence of the presence of small particles in lower amounts as evidenced from the SEM-EDX analysis. A general correlation between the amount of a co-catalyst and H_2 production has been observed, depending on the cocatalyst used. Normally, the activity increases as the loading of the cocatalyst increases, up to a certain point, beyond which increasing the cocatalyst amount will result in a decrease in photocatalytic activity due to the coverage of the active sites on the surface[23]. Some studies with Ag/TiO_2 catalysts reported the best PEC performance in H_2 generation with lower Ag concentration thus corroborating our hypothesis[24].

3.3.3. Ethanol photo-dehydrogenation in gas/liquid phase

In a light-assisted process such as water splitting, at the anode compartment, the parallel oxygen evolution reaction (OER) occurs. This process, due to the slow kinetics, reduces the efficiency of the whole process[25].

The possibility of obtaining, (together with H_2 at the cathode side) high-added-value products (such as aldehydes or organic acid) instead of oxygen is very appealing from an industrial point of view. Moreover, as already described in Chapter 1, the presence of an organic compound, even in a small amount, allows at the same time, a greater production of hydrogen, since the oxidation reaction of the organic compound has a greater efficiency than the oxidation reaction of water and this may represent an opportunity for the utilization of waste from biomass treatment. Thus, in this section, we studied the reaction of photo-dehydrogenation of ethanol, a process which is conventionally performed in the liquid phase. Operating in the gas phase could offer instead several potential advantages compared to traditional slurry photochemical reactors[26].

These advantages include:

(i) minimization of scattering phenomena, enhancing the efficiency of light absorption and utilization in the catalytic process.

(ii) good pattern of irradiation: gas-phase operation provides a more controlled and favourable pattern of irradiation. This controlled environment contributes to better precision in directing light onto the catalytic system, optimizing the photochemical reactions.

(iii) efficient transfer of power from sunlight to a conductive substrate: this is crucial for harnessing solar energy in electro-catalytic processes, leading to enhanced overall performance.

(iv) easier scale-up: this scalability is essential for transitioning laboratory-scale processes to industrial applications, ensuring practical viability and broader implementation.

(v) elimination of problems associated with metal-leaching, a common concern in slurry-based reactors: this contributes to the stability and longevity of the catalytic system, reducing potential environmental and operational challenges.

(vi) easier product recovery: the distinct phase separation allows for more straightforward isolation and collection of the desired products, streamlining downstream processing.

All these advantages contribute to enhancing the effectiveness and practicality of photochemical operations.

For this reason, Ag, Au and Pd deposited on TiO_2 NTs meshes electrodes, prepared as indicated in Table 3.7, were tested using the photo-electrochemical cell described in the experimental section, in both gas and liquid phase operations, to study the impact of the cell configuration in the photo dehydrogenation of ethanol. These metals are typically used in the reactions of organic alcohols oxidation[27, 28]. So, rather than on the cathodic production of H_2, we focused this study on understanding the effect of the nature of the cocatalyst deposited on the TiO_2 support on the anodic product selectivity, and their action mechanism in the oxidation reaction, an aspect scarcely investigated.

3.3.3.1. Photo-electrochemical characterization before the testing

The electrochemical behaviour of the electrodes was evaluated by cyclic voltammetry (CV) measurements and electrochemical impedance spectroscopy (EIS) analysis.

The CV curves were recorded in the exact conditions of the photo-electrocatalytic tests in a two electrodes cell, utilizing electrolyte 0.050 M H_2SO_4 at the cathode, under both gas and liquid phase configurations (see paragraph 3.2.3.). The

measurements were conducted with and without irradiation, at applied voltage from -0.25 V to +1.5 V, with a potential scan rate of 0.05 V · s^{-1}.

From the result reported in Figures from 3.15 to 3.17 (for Pd/TiO_2, Ag/TiO_2 and Au/TiO_2 samples), it was evident that the presence of light reduced the onset potential for the oxygen evolution reaction (OER), increasing at the same time the current, as expected from a photoactive material. In all CV profiles, the effect of the illumination was evident, with an enhancement in the oxidation reaction, both in the liquid and gas phases. In general terms, the metal oxidation peaks were more evident in the liquid phase, due to the presence of the electrolyte in the anodic compartment in direct contact with the photoelectrode. Analysing in detail the behaviour of the different metals in gas and liquid configurations, it was possible to notice that the process in the liquid phase was more efficient, in terms of current density, for the Pd/TiO_2, opposite for the Ag/TiO_2 sample. No substantial differences were instead shown with Au/TiO_2[29].

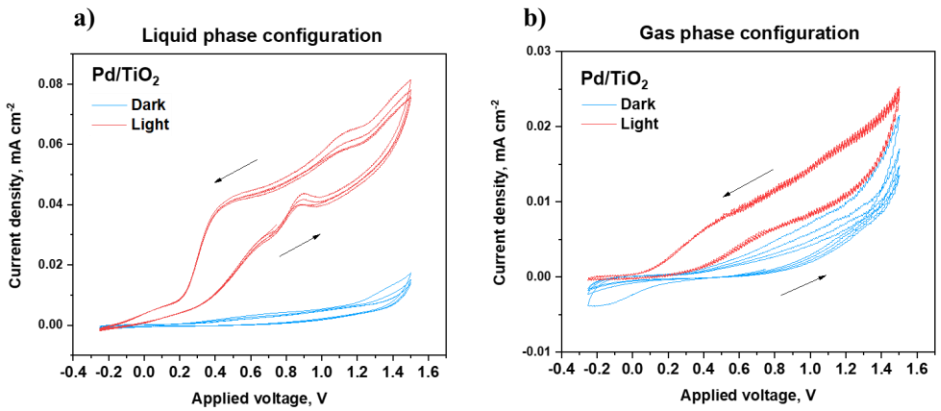

Figure 3.15 *Cyclic voltammetry profiles of Pd/TiO_2 sample performed in a) liquid-phase configuration and b) gas-phase configuration in dark and under light irradiation conditions. The arrow indicates the direction of the measurement.*

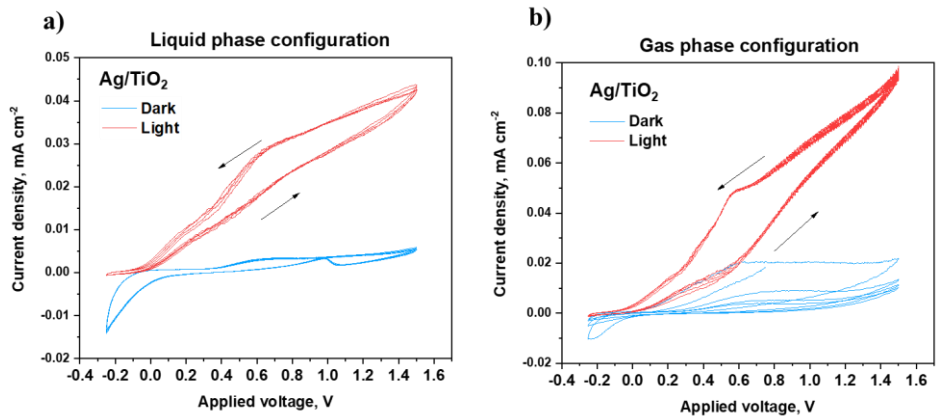

Figure 3.16 *Cyclic voltammetry profiles of Ag/TiO_2 sample performed in a) liquid-phase configuration and b) gas-phase configuration in dark and under light irradiation conditions. The arrow indicates the direction of the measurement.*

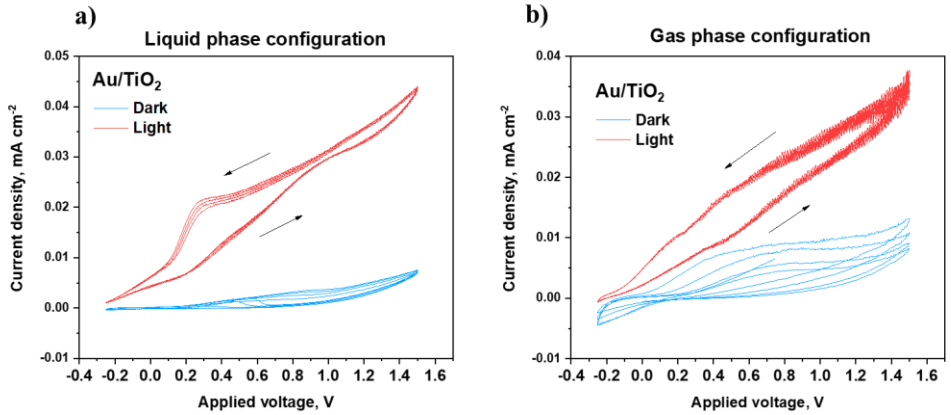

Figure 3.17 *Cyclic voltammetry profiles of Au/TiO_2 sample performed in a) liquid-phase configuration and b) gas-phase configuration in dark and under light irradiation conditions. The arrow indicates the direction of the measurement.*

To evaluate charge transfer phenomena, which can strongly influence the electrochemical behaviour of metal-modified TiO_2 samples, electrochemical impedance spectroscopy (EIS) analysis was performed, in both gas and liquid phase configurations, using the same cell (at two electrodes) and the same experimental conditions described for CV measurements[28,30].

EIS measurements were conducted at the fixed applied potential of +0.4 V, +0.8 V, +1.0 V, and +1.4 V, and the frequencies scanned from 10000 Hz to 0.1 Hz. The data were fitted with Zview® software, by using the one-constant and two-constant circuit models shown in Figure 3.18. More in detail, for gas-phase configuration the simple one-constant circuit model was used to fit the data, in both dark and under light irradiation, whereas for liquid-phase configuration was used the two-constant circuit model[31]. While Rs is correlated to electrical connections of the cell, Rct is the resistance associated with the electrochemical process, thus with the phenomena occurring at the electrode surface. Note that for a liquid-phase process, two charge transfer resistances are evaluated, Rct at low frequency and Rct' at high frequency, the latter is specifically related to the charge transfer in a liquid electrolyte.

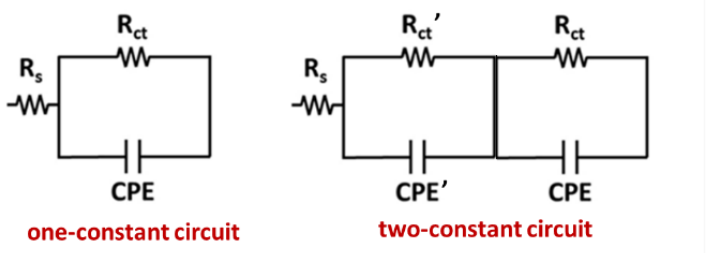

Figure 3.18 *One constant circuit and two constant circuit models used to fit EIS data*

Figures from 3.19 to 3.21 reported the Nyquist plots obtained for Pd, Au and Ag on TiO_2NTs/Ti mesh in dark and under light irradiation, in gas-phase configurations (i.e. with the electrode in contact with the gaseous stream of ethanol coming from the external task, see experimental part).

Figures from 3.22 to 3.24 show instead the Nyquist plots obtained in the conventional liquid-phase configuration with the electrode immersed in the electrolyte. All the bode plots in dark and under light irradiation at different applied potentials for all the tested photoelectrodes together with the tables with

the resulting equivalent electric circuit parameters from EIS fitting, are reported in the Annex at the end of the chapter.

In the plots, the experimental data are represented by points, while the lines indicate the fitting curves processed with the software.

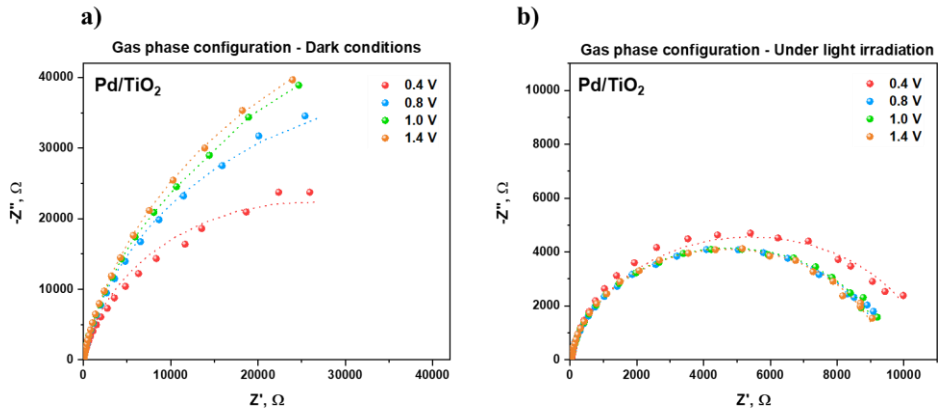

Figure 3.19 *Nyquist plots of Pd/TiO_2 in gas phase configuration in the dark (**a**) and under light irradiation (**b**) Filled symbols, experimental impedance data; lines, fitting by using the one-constant equivalent circuit model.*

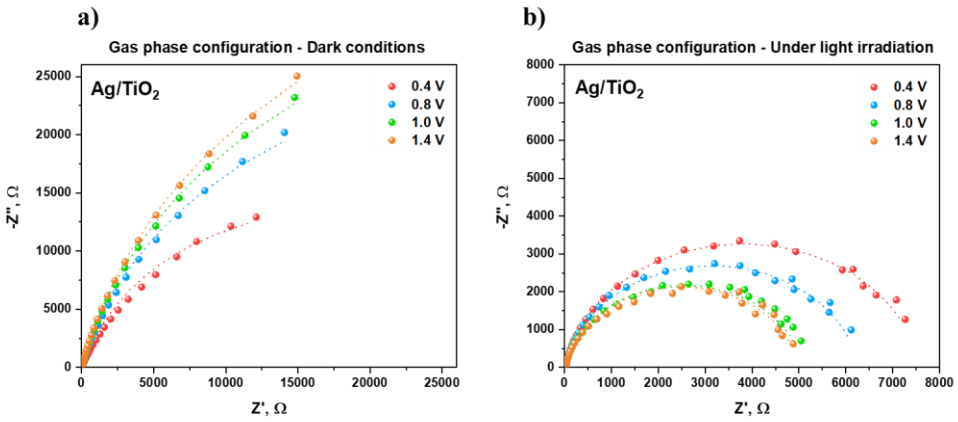

Figure 3.20 *Nyquist plots of Ag/TiO_2 in gas phase configuration in dark (**a**) and under light irradiation (**b**) Filled symbols, experimental impedance data; lines, fitting by using the one-constant equivalent circuit model.*

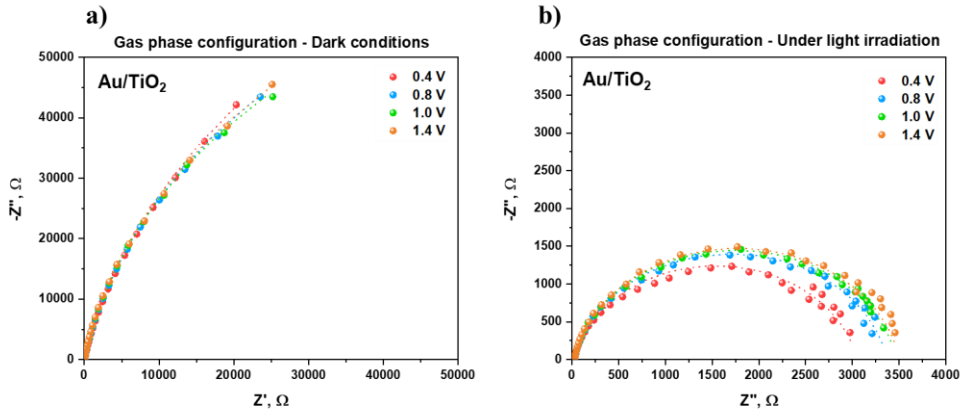

Figure 3.21 *Nyquist plots of Au/TiO_2 in gas phase configuration in dark (**a**) and under light irradiation (**b**) Filled symbols, experimental impedance data; lines, fitting by using the one-constant equivalent circuit model.*

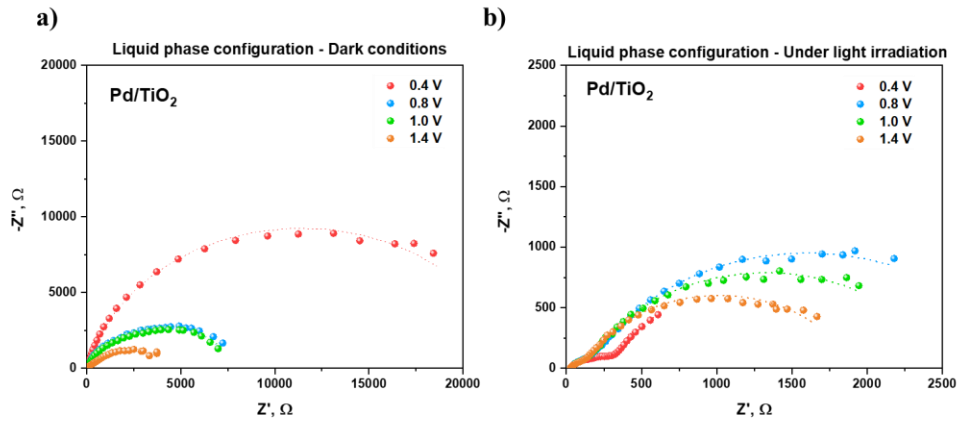

Figure 3.22 *Nyquist plots of Pd/TiO_2 in liquid phase configuration in dark (**a**) and under light irradiation (**b**) Filled symbols, experimental impedance data; lines, fitting by using the two-constant equivalent circuit model.*

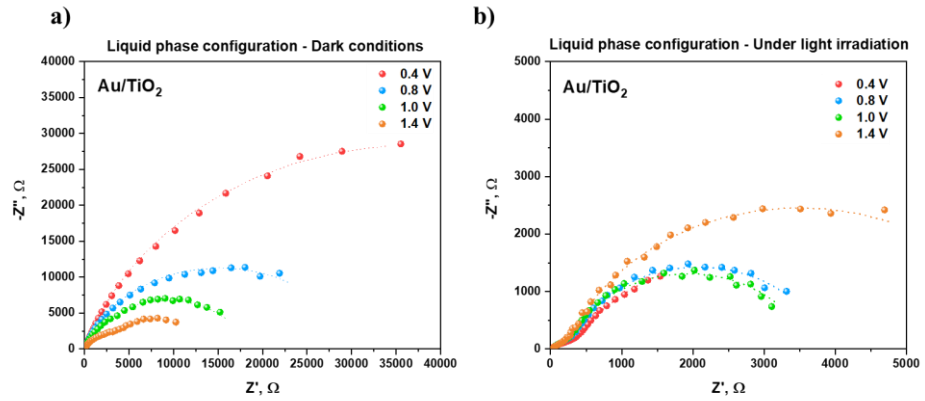

Figure 3.23 *Nyquist plots of Au/TiO_2 in liquid phase configuration in dark (**a**) and under light irradiation (**b**) Filled symbols, experimental impedance data; lines, fitting by using the two-constant equivalent circuit model.*

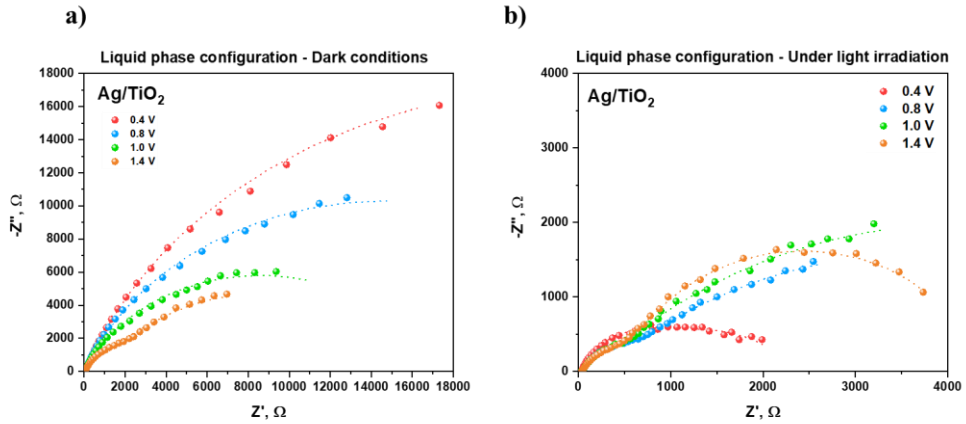

Figure 3.24 *Nyquist plots of Ag/TiO_2 in liquid phase configuration in dark (**a**) and under light irradiation (**b**) Filled symbols, experimental impedance data; lines, fitting by using the two-constant equivalent circuit model.*

Observing the Nyquist plots is possible to note that in both configurations (gas phase and liquid phase), Rct values (i.e. the diameter of the semicircle) with light irradiation were lower at all the applied potentials, as it was expected for a photoactive material, and in agreement with the results shown in chapter 2 for TiO_2NTs.

To make an easier comparison between the gas and liquid phases, we reported all the obtained values of the charge transfer resistance (Rct) under light in Table

3.10. The resistance values are in good agreement with the CV profiles, as Pd/TiO_2 showed a minor resistance in the liquid phase, (2395 Ω vs 9525 Ω at 1.0 V) opposite to Ag/TiO_2 (8100 Ω vs 5069 Ω at 1.0V), while for Au/TiO_2 no relevant differences were noticed passing from gas to liquid configuration. In general terms, the charge transfer resistance associated with an electrochemical process tends to be lower during gas-phase analysis, particularly at lower potentials [31]. In this case, instead, the role of the electrolyte was not so fundamental and the resistances in the gas phase were higher, probably due to the absorption phenomena on the surface of the electrode[31].

Sample	Applied potential	Liquid phase Rct (Ω)	Gas-phase Rct (Ω)
TiO_2	0.4 V	2604	6456
	0.8 V	2684	7692
	1.0 V	2875	8314
	1.4 V	2460	10869
Ag/TiO_2	0.4 V	1567	7564
	0.8 V	6721	6255
	1.0 V	8100	5069
	1.4 V	3486	4990
Pd/TiO_2	0.4 V	2441	10773
	0.8 V	2883	9485
	1.0 V	2395	9525
	1.4 V	1800	9392
Au/TiO_2	0.4 V	5297	3030
	0.8 V	3556	3346
	1.0 V	3366	3446
	1.4 V	6495	3479

Table 3.10 *Rct values acquired from EIS fitting under light irradiation in gas and liquid phase at different applied potentials*

3.3.3.2. Productivity in gas and liquid phase configurations

The results of the photo-electrocatalytic tests for Ag and Pd on TiO_2 NTs/Ti mesh are reported in Figure 3.25 and Figure 3.26 for gas and liquid phase configurations respectively, while for Au/TiO_2 samples the results are shown in Figure 3.27 and 3.28. It should be emphasized again that this study aims to evaluate the influence of a particular configuration of the cell on the performances in terms of the formation of valuable oxidation products, and not of hydrogen production which occurs parallel in the cathode side. All the productivity values (including hydrogen obtained at the cathode side) are reported in the annex at the end of the chapter. The adoption of liquid or gas phase conditions had a strong impact on the catalytic behaviour, particularly in terms of selectivity. In gas-phase operations, while the amount of acetaldehyde due to the reaction of photo-dehydrogenation of ethanol, was similar for all the samples tested, the presence of metal NPs (Pd and Ag) on TiO_2 catalysed the subsequent reaction of oxidation of acetaldehyde to acetic acid (the opposite of what happens with the liquid phase configuration, see Figure 3.26). No CO_2, CO or methane were detected during the tests. The absence of CO_2 may suggest that the reactions of ethanol (or acetaldehyde) photo-reforming was negligible. So, the presence of metal NPs on the TiO_2 surface influenced the distribution of the ethanol oxidation products, specifically in the gas phase.

The mechanism of formation of acetaldehyde on TiO_2-based material under UV light, has been widely studied[32, 33] and can be explained as follows: i) after UV irradiation, adsorbed ethanol molecules undergo O–H bond dissociation on Ti–O centres of TiO_2 to yield ethoxy species and hydroxyl groups, ii) hydroxyls by reacting with h^+ form OH radicals. iii) the OH radicals react with adsorbed ethoxy species to produce adsorbed acetaldehyde radicals iv) The acetaldehyde radicals desorb after the loss of one electron. Acetic acid may then be formed for further oxidation of acetaldehyde, but it is not generally detected[31].

The possibility to selectively oxidise acetaldehyde to acetic acid in gas-phase has recently been reported for Pd-Au-based catalysts[23]. A similar mechanism is possible also in our case, due specifically to the light and related to the presence of nanoparticles on the photoactive material[34].

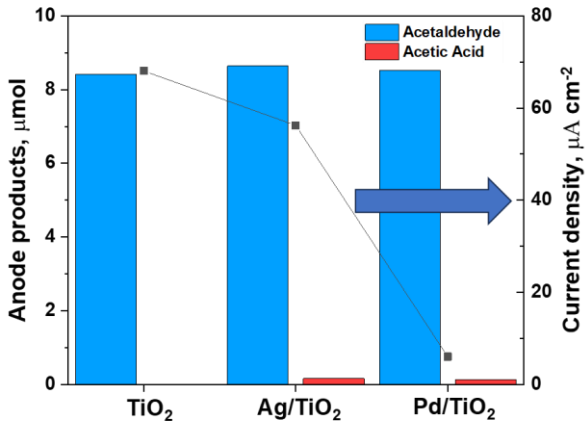

Figure 3.25 *Anode products and average current density for the tests in gas-phase configuration with TiO_2, Ag/TiO_2 and Pd/TiO_2*

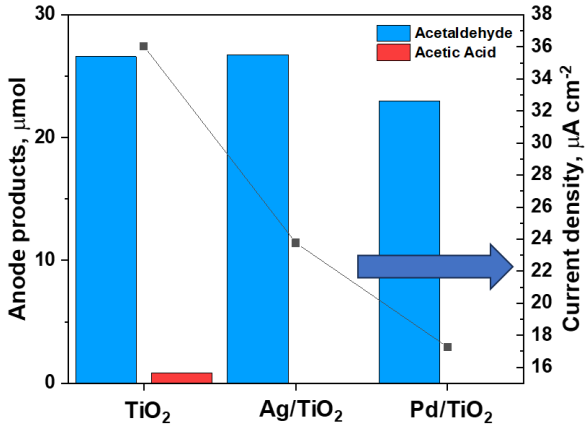

Figure 3.26 *Anode products and average current density for the tests in liquid-phase configuration with TiO_2, Ag/TiO_2 and Pd/TiO_2*

Also, for Au/TiO_2-based catalysts, it is quite well known that ethanol can be partially oxidized to acetaldehyde by photocatalysis and many studies, also

theoretical or kinetics were performed to elucidate the mechanism of this reaction on these catalysts[35–37]. No studies are reported on the contrary on the different configurations of the photo-electrochemical cell for ethanol dehydrogenation.

The behaviour of gold catalysts was the opposite of Pd and Ag catalysts, as in the gas phase configuration no acetic acid formation was observed (see Figure 3.27). In the liquid phase, the Au/TiO_2 sample exhibited in general superior productivity (compared to bare TiO_2 and Pd and Ag catalysts) and a change in the selectivity was also observed, although this may not be straightly related to the charge transfer resistances, as observed from EIS data.

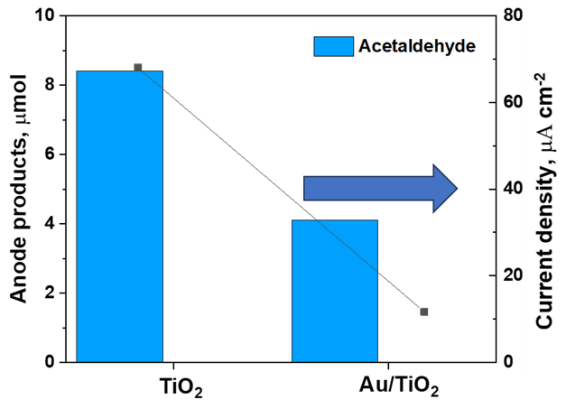

Figure 3.27 *Anode products and average current density for the tests in gas-phase configuration with TiO_2, and Au/TiO_2*

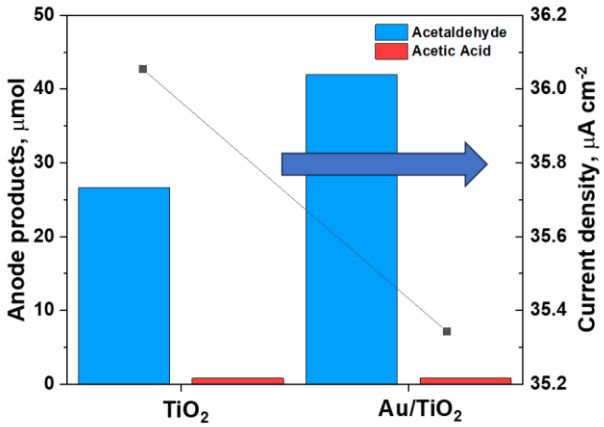

Figure 3.28 *Anode products and Average current density for the tests in liquid-phase configuration with TiO_2, and Au/TiO_2*

3.4. Conclusions

TiO_2 and metal loaded (Ag, Au, Cu, Pd)/TiO_2 samples were compared to study the effect of a co-catalyst on the optical and photo-electrical characteristics as well as on the catalytic performances in two different reactions: water photo-electrolysis and ethanol photo-dehydrogenation. Au, Pd, Cu and Ag were successfully deposited on the hierarchical 3D structure formed by the mesoporous array of nanotubes grown over a microporous Ti mesh.

Morphological, optical, and photo-electrical characterization were performed (including CV, CA, and EIS). The results obtained in the water photo-electrolysis in a PEC cell, were very promising as the metal-modified electrodes showed a notable enhancement in the performances compared to unmodified titanium dioxide substrate. The same materials were tested in the reaction of ethanol photo-conversion in two different cell configurations (liquid and gas phase) to investigate simultaneously two key factors: i) the role of metal nanoparticles and ii) the impact of the presence of an electrolyte on the oxidation products selectivity and photoactivity.

The choice of metal nanoparticles and the presence of an electrolyte influenced the type and quantity of products formed at the anode during the ethanol photo-conversion process in the gas phase. In fact, with Au, compared to Pd and Ag catalysts, no acetic acid formation was observed contrary to the liquid phase configuration. This behaviour is the opposite for Pd and Ag-modified catalysts.

The observation that by varying cell configurations, a distinct reaction pathway in ethanol photo-dehydrogenation and, consequently, different selectivity, was obtained adds an attractive dimension to this study. A further understanding of these aspects would be in any case necessary, to further optimize the photo-catalytic behaviour.

3.5. References

[1] D. Bahnemann, D. Bockelmann, and R. Goslich, “Mechanistic studies of water detoxification in illuminated TiO_2 suspensions,” *Solar Energy Materials*, vol. 24, no. 1–4, pp. 564–583, Dec. 1991, doi: 10.1016/0165-1633(91)90091-X.

[2] J. Yu, G. Dai, and B. Huang, “Fabrication and characterization of visible-light-driven plasmonic photocatalyst Ag/AgCl/TiO_2 nanotube arrays,” *Journal of Physical Chemistry C*, vol. 113, no. 37, pp. 16394–16401, Sep. 2009, doi: 10.1021/jp905247j.

[3] A. Gellé and A. Moores, “Water splitting catalyzed by titanium dioxide decorated with plasmonic nanoparticles,” *Pure and Applied Chemistry*, vol. 89, no. 12, pp. 1817–1827, Nov. 2017, doi: 10.1515/pac-2017-0711.

[4] J. Zhao, J. Wang, A. J. Brock, and H. Zhu, “Plasmonic heterogeneous catalysis for organic transformations,” *Journal of Photochemistry and Photobiology C: Photochemistry Reviews*, vol. 52, p. 100539, Sep. 2022, doi: 10.1016/j.jphotochemrev.2022.100539.

[5] Z. Sun and Y. Fang, “Electrical tuning effect for Schottky barrier and hot-electron harvest in a plasmonic Au/TiO_2 nanostructure,” *Sci Rep*, vol. 11, no. 1, p. 338, Jan. 2021, doi: 10.1038/s41598-020-79746-5.

[6] A. Kumar, P. Choudhary, A. Kumar, P. H. C. Camargo, and V. Krishnan, “Recent Advances in Plasmonic Photocatalysis Based on TiO_2 and Noble Metal Nanoparticles for Energy Conversion, Environmental Remediation, and Organic Synthesis,” *Small*, vol. 18, no. 1, Jan. 2022, doi: 10.1002/smll.202101638.

[7] A. Bogaerts, G. Centi, V. Hessel, and E. Rebrov, “Challenges in unconventional catalysis,” *Catal Today*, vol. 420, p. 114180, Aug. 2023, doi: 10.1016/j.cattod.2023.114180.

[8] S. Zhang, B. Peng, S. Yang, H. Wang, H. Yu, Y. Fang, and F. Peng, “Non-noble metal copper nanoparticles-decorated TiO_2 nanotube arrays with plasmon-enhanced photocatalytic hydrogen evolution under visible light,” *Int J Hydrogen Energy*, vol. 40, no. 1, pp. 303–310, Jan. 2015, doi: 10.1016/j.ijhydene.2014.10.122.

[9] Z. Jiang, Q. Ouyang, B. Peng, Y. Zhang, and L. Zan, “Ag size-dependent visible-light-responsive photoactivity of Ag–TiO_2 nanostructure based on surface plasmon resonance,” *J. Mater. Chem. A*, vol. 2, no. 46, pp. 19861–19866, 2014, doi: 10.1039/C4TA03831B.

[10] S. De Marchi, S. Núñez-Sánchez, G. Bodelón, J. Pérez-Juste, and I. Pastoriza-Santos, “Pd nanoparticles as a plasmonic material: synthesis, optical properties and applications,” *Nanoscale*, vol. 12, no. 46, pp. 23424–23443, 2020, doi: 10.1039/D0NR06270G.

[11] C. Ampelli, F. Tavella, C. Genovese, S. Perathoner, M. Favaro, and G. Centi, “Analysis of the factors controlling performances of Au-modified TiO_2 nanotube array based photoanode in photo-electrocatalytic (PECa) cells,” *Journal of Energy Chemistry*, vol. 26, no. 2, pp. 284–294, Mar. 2017, doi: 10.1016/j.jechem.2016.11.004.

[12] S. Noothongkaew, J. K. Han, Y. B. Lee, O. Thumthan, and K. S. An, “Au NPs decorated TiO_2 nanotubes array candidate for UV photodetectors,” *Progress in Natural Science: Materials International*, vol. 27, no. 6, pp. 641–646, Dec. 2017, doi: 10.1016/j.pnsc.2017.10.001.

[13] L. Wu, F. Li, Y. Xu, J. W. Zhang, D. Zhang, G. Li, and H. Li, “Plasmon-induced photoelectrocatalytic activity of Au nanoparticles enhanced TiO_2

nanotube arrays electrodes for environmental remediation," *Appl Catal B*, vol. 164, pp. 217–224, Mar. 2015, doi: 10.1016/j.apcatb.2014.09.029.

[14] Z. Lian, W. Wang, S. Xiao, X. Li, Y. Cui, D. Zhang, G. Li, and H. Li, "Plasmonic silver quantum dots coupled with hierarchical TiO_2 nanotube arrays photoelectrodes for efficient visible-light photoelectrocatalytic hydrogen evolution," *Sci Rep*, vol. 5, no. 1, p. 10461, Jun. 2015, doi: 10.1038/srep10461.

[15] D. Giusi, C. Ampelli, C. Genovese, S. Perathoner, and G. Centi, "A novel gas flow-through photocatalytic reactor based on copper-functionalized nanomembranes for the photoreduction of CO_2 to C1-C2 carboxylic acids and C1-C3 alcohols," *Chemical Engineering Journal*, vol. 408, p. 127250, Mar. 2021, doi: 10.1016/j.cej.2020.127250.

[16] P. Liu, Y. Zhao, R. Qin, S. Mo, G. Chen, L. Gu, D. M. Chevrier, P. Zhang, Q. Guo, D. Zang, B. Wu, G. Fu, and N. Zheng, "Photochemical route for synthesizing atomically dispersed palladium catalysts," *Science (1979)*, vol. 352, no. 6287, pp. 797–800, May 2016, doi: 10.1126/science.aaf5251.

[17] K. Syrek, J. Grudzień, A. Sennik-Kubiec, A. Brudzisz, and G. D. Sulka, "Anodic Titanium Oxide Layers Modified with Gold, Silver, and Copper Nanoparticles," *J Nanomater*, vol. 2019, pp. 1–10, Feb. 2019, doi: 10.1155/2019/9208734.

[18] K.-C. Lee, S.-J. Lin, C.-H. Lin, C.-S. Tsai, and Y.-J. Lu, "Size effect of Ag nanoparticles on surface plasmon resonance," *Surf Coat Technol*, vol. 202, no. 22–23, pp. 5339–5342, Aug. 2008, doi: 10.1016/j.surfcoat.2008.06.080.

[19] K. B. Mogensen and K. Kneipp, "Size-Dependent Shifts of Plasmon Resonance in Silver Nanoparticle Films Using Controlled Dissolution: Monitoring the Onset of Surface Screening Effects," *The Journal of*

Physical Chemistry C, vol. 118, no. 48, pp. 28075–28083, Dec. 2014, doi: 10.1021/jp505632n.

[20] X. Huang and M. A. El-Sayed, "Gold nanoparticles: Optical properties and implementations in cancer diagnosis and photothermal therapy," *J Adv Res*, vol. 1, no. 1, pp. 13–28, Jan. 2010, doi: 10.1016/j.jare.2010.02.002.

[21] F. Conte, I. Rossetti, G. Ramis, C. Vaulot, S. Hajjar-Garreau, and S. Bennici, "Low Metal Loading (Au, Ag, Pt, Pd) Photo-Catalysts Supported on TiO_2 for Renewable Processes" *Materials*, vol. 15, no. 8, pp. 2915, Apr. 2022, doi: 10.3390/ma15082915.

[22] F. Tavella, C. Ampelli, L. Frusteri, F. Frusteri, S. Perathoner, and G. Centi, "Development of photoanodes for photoelectrocatalytic solar cells based on copper-based nanoparticles on titania thin films of vertically aligned nanotubes," *Catal Today*, vol. 304, pp. 190–198, Apr. 2018, doi: 10.1016/j.cattod.2017.08.036.

[23] K. C. Christoforidis and P. Fornasiero, "Photocatalytic Hydrogen Production: A Rift into the Future Energy Supply," *ChemCatChem*, vol. 9, no. 9, pp. 1523–1544, May 2017, doi: 10.1002/cctc.201601659.

[24] N. Naseri, H. Kim, W. Choi, and A. Z. Moshfegh, "Optimal Ag concentration for H_2 production via Ag: TiO_2 nanocomposite thin film photoanode," *Int J Hydrogen Energy*, vol. 37, no. 4, pp. 3056–3065, Feb. 2012, doi: 10.1016/j.ijhydene.2011.11.041.

[25] K. Takanabe, "Photocatalytic Water Splitting: Quantitative Approaches toward Photocatalyst by Design," *ACS Catal*, vol. 7, no. 11, pp. 8006–8022, Nov. 2017, doi: 10.1021/acscatal.7b02662.

[26] C. Ampelli, R. Passalacqua, C. Genovese, S. Perathoner, G. Centi, T. Montini, V. Gombac, J. J. Delgado Jaen, and P. Fornasiero, "H_2 production by selective photo-dehydrogenation of ethanol in gas and liquid phase on

CuO_x/TiO_2 nanocomposites," *RSC Adv*, vol. 3, no. 44, p. 21776, 2013, doi: 10.1039/c3ra22804e.

[27] H. Bahruji, M. Bowker, P. R. Davies, and F. Pedrono, "New insights into the mechanism of photocatalytic reforming on Pd/TiO_2," *Appl Catal B*, vol. 107, no. 1–2, pp. 205–209, Aug. 2011, doi: 10.1016/j.apcatb.2011.07.015.

[28] D. I. Enache, J. K. Edwards, P. Landon, B. Solsona-Espriu, A. F. Carley, A. A. Herzing, M. Watanabe, C. J. Kiely, D. W. Knight, and G. J. Hutchings, "Solvent-Free Oxidation of Primary Alcohols to Aldehydes Using Au-Pd/TiO_2 Catalysts," *Science (1979)*, vol. 311, no. 5759, pp. 362–365, Jan. 2006, doi: 10.1126/science.1120560.

[29] A. J. Bard and L. R. Faulkner, *Electrochemical Methods: Fundamentals and Applications, 2nd Edition*. Wiley, 2001.

[30] J. R. MacDonald, *Impedance Spectroscopy*. Wiley-Interscience, 1987.

[31] D. Giusi, M. Miceli, C. Genovese, G. Centi, S. Perathoner, and C. Ampelli, "In situ electrochemical characterization of CuxO-based gas-diffusion electrodes (GDEs) for CO_2 electrocatalytic reduction in presence and absence of liquid electrolyte and relationship with C2+ products formation," *Appl Catal B*, vol. 318, Dec. 2022, doi: 10.1016/j.apcatb.2022.121845.

[32] T. Reztsova, C.-H. Chang, J. Koresh, and H. Idriss, "Dark- and Photoreactions of Ethanol and Acetaldehyde over TiO_2/Carbon Molecular Sieve Fibers," *J Catal*, vol. 185, no. 1, pp. 223–235, Jul. 1999, doi: 10.1006/jcat.1999.2520.

[33] A. K. Wahab, S. Bashir, Y. Al-Salik, and H. Idriss, "Ethanol photoreactions over Au–Pd/TiO_2," *Appl Petrochem Res*, vol. 4, no. 1, pp. 55–62, May 2014, doi: 10.1007/s13203-014-0051-4.

[34] S. Han, K. Shin, G. Henkelman, and C. B. Mullins, “Selective Oxidation of Acetaldehyde to Acetic Acid on Pd–Au Bimetallic Model Catalysts,” *ACS Catal*, vol. 9, no. 5, pp. 4360–4368, May 2019, doi: 10.1021/acscatal.9b00079.

[35] M. A. Nadeem, M. Murdoch, G. I. N. Waterhouse, J. B. Metson, M. A. Keane, J. Llorca, and H. Idriss, “Photoreaction of ethanol on Au/TiO_2 anatase: Comparing the micro to nanoparticle size activities of the support for hydrogen production,” *J Photochem Photobiol A Chem*, vol. 216, no. 2–3, pp. 250–255, Dec. 2010, doi: 10.1016/j.jphotochem.2010.07.007.

[36] E. Behravesh, M. M. Melander, J. Wärnå, T. Salmi, K. Honkala, and D. Yu. Murzin, “Oxidative dehydrogenation of ethanol on gold: Combination of kinetic experiments and computation approach to unravel the reaction mechanism,” *J Catal*, vol. 394, pp. 193–205, Feb. 2021, doi: 10.1016/j.jcat.2020.07.022.

[37] D. Sannino, V. Vaiano, P. Ciambelli, M. C. Hidalgo, J. J. Murcia, and J. A. Navío, “Oxidative Dehydrogenation of Ethanol over Au/TiO_2 Photocatalysts,” *Journal of Advanced Oxidation Technologies*, vol. 15, no. 2, Jan. 2012, doi: 10.1515/jaots-2012-0206.

3.6. Annex

3.6.1. Materials

Ti gauze 80mesh was purchased from Alfa Aesar.

The chemicals used in all synthesis routes were purchased from Sigma-Aldrich and used without any further purification.

Nafion membrane was obtained from Ion power and was pre-treated before use.

3.6.2. Mathematical methods

- The voltage values were converted to RHE using the following formula.

$$E_{(RHE)} = E_{(Ag/AgCl)} + 0.059\,pH + 0.21$$

- The formula used to calculate the H_2 production was the following:

$$H_2\,production\ (\mu mol \cdot\ h^{-1}cm^{-2}) = \frac{[H_2](\%vol.) \cdot Q\ (L/min)}{V_m\ (L/mol)} \cdot \frac{1}{60\ \cdot A(cm^2)}\ 10^6$$

$[H_2]$ = % of hydrogen detected by the GC

Q = flow rate

V_m = molar volume of a gas at room temperature and pressure

A = active area of the catalyst

3.6.3. CV characterization

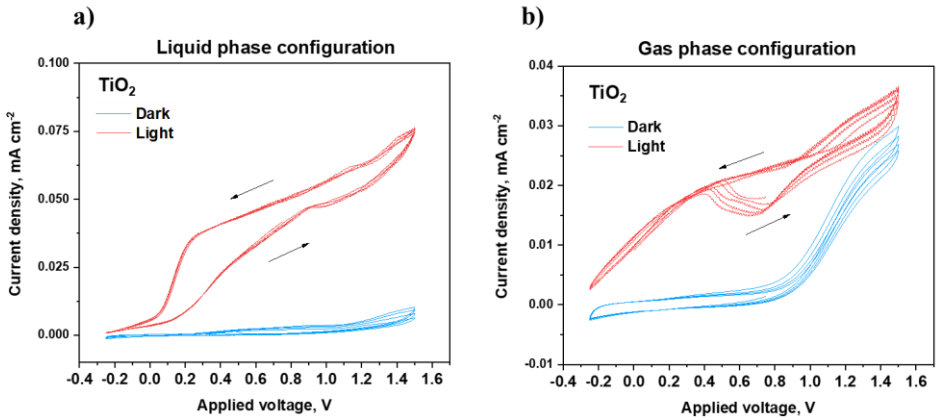

Figure A3.29 *Cyclic voltammetry profiles of TiO_2 sample performed in a) liquid-phase configuration and b) gas-phase configuration in dark and light irradiation conditions. The arrow indicates the direction of the measurement.*

3.6.4. EIS characterization

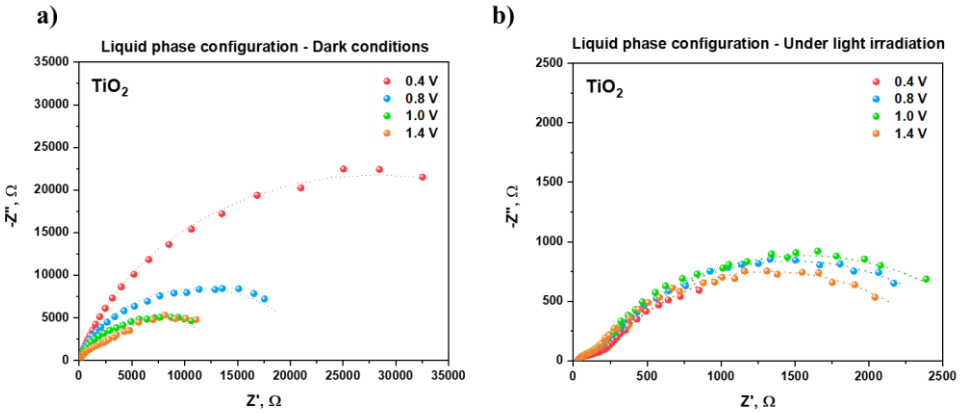

Figure A3.30 *Nyquist plots of TiO_2 in liquid phase configuration in dark (**a**) and under light irradiation (**b**) Filled symbols, experimental impedance data; lines, fitting by using the one- and two-constant equivalent circuit model.*

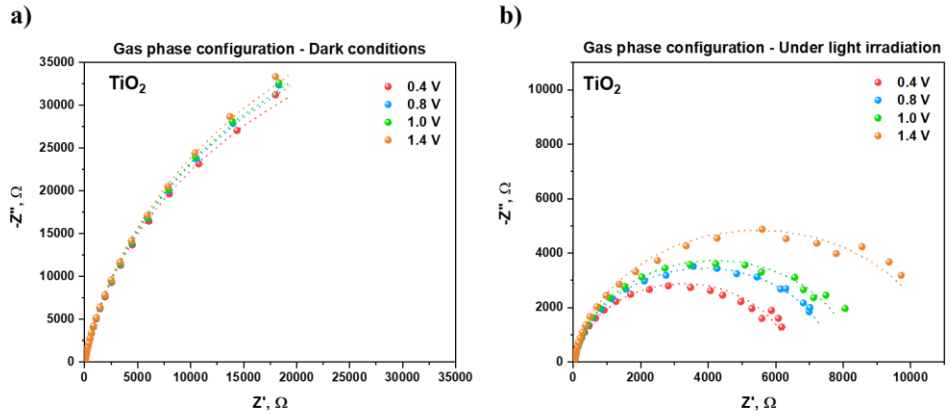

Figure A3.31 *Nyquist plots of TiO_2 in gas phase configuration in dark (**a**) and under light irradiation (**b**) Filled symbols, experimental impedance data; lines, fitting by using the one- and two-constant equivalent circuit model.*

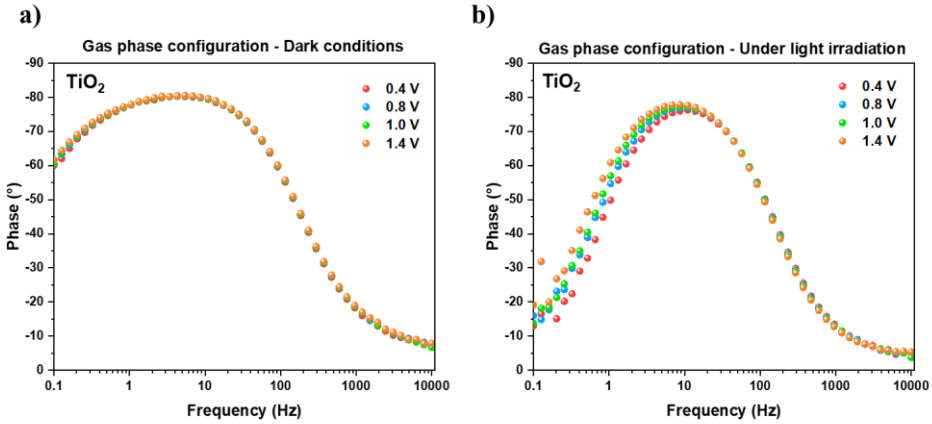

Figure A3.32 *Bode plot of TiO_2 in gas phase configuration, in (**a**) dark conditions, and (**b**) under light irradiation*

.

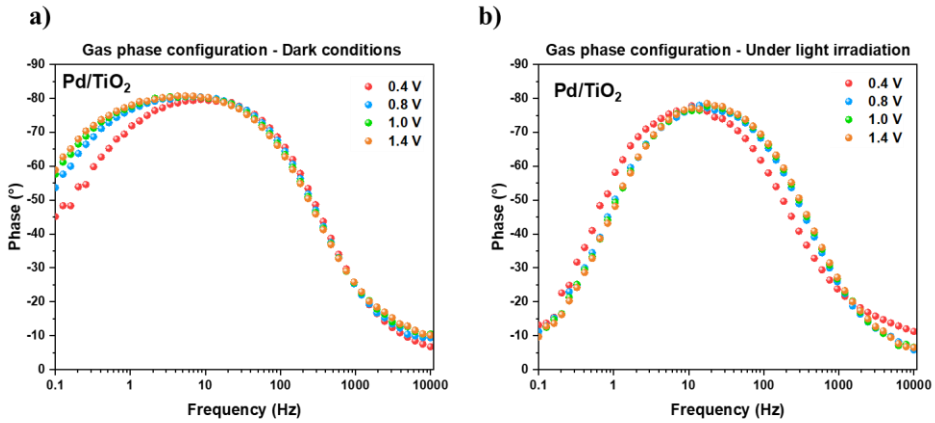

Figure A3.33 *Bode plot of Pd/TiO_2 in gas phase configuration, in (**a**) dark conditions, and (**b**) under light irradiation*

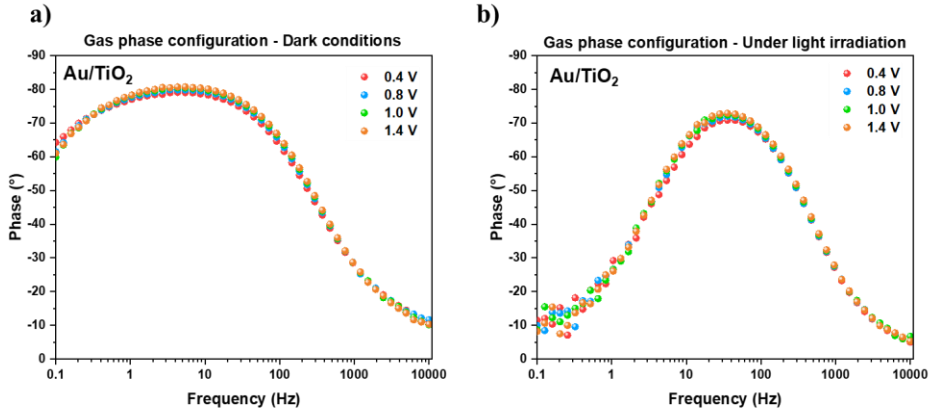

Figure A3.34 *Bode plot of Au/TiO_2 in gas phase configuration, in (**a**) dark conditions, and (**b**) under light irradiation.*

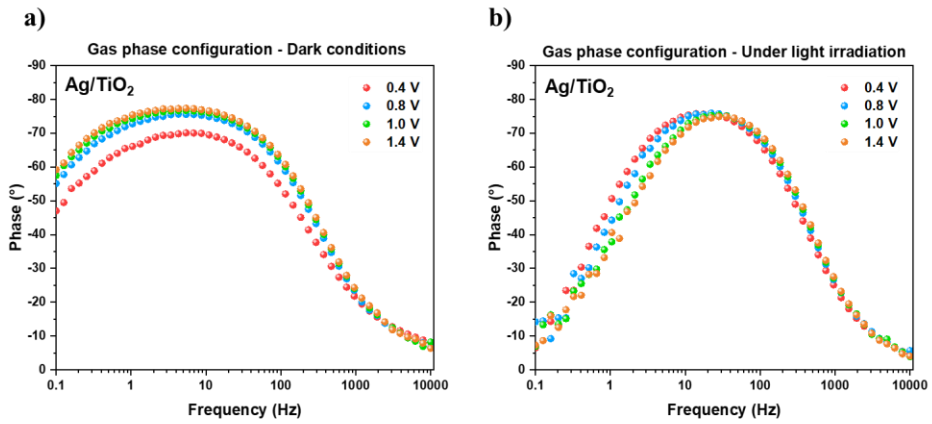

Figure A3.35 *Bode plot of Ag/TiO_2 in gas phase configuration, in (**a**) dark conditions, and (**b**) under light irradiation.*

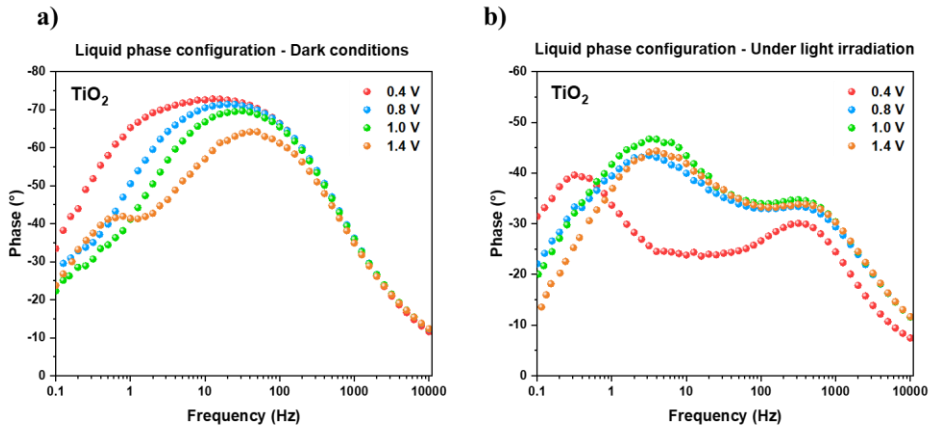

Figure A3.36 *Bode plots of TiO_2 in liquid phase configuration, in (**a**) dark conditions, and (**b**) under light irradiation.*

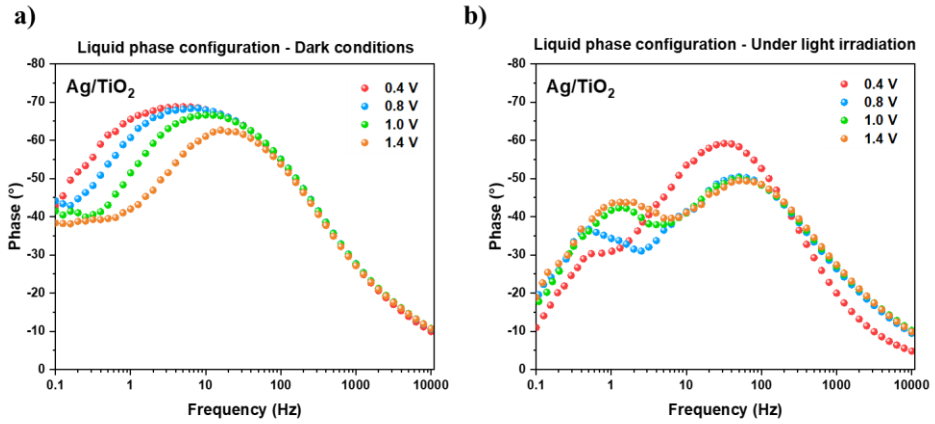

Figure A3.37 *Bode plots of Ag/TiO_2 in liquid phase configuration, in (**a**) dark conditions, and (**b**) under light irradiation.*

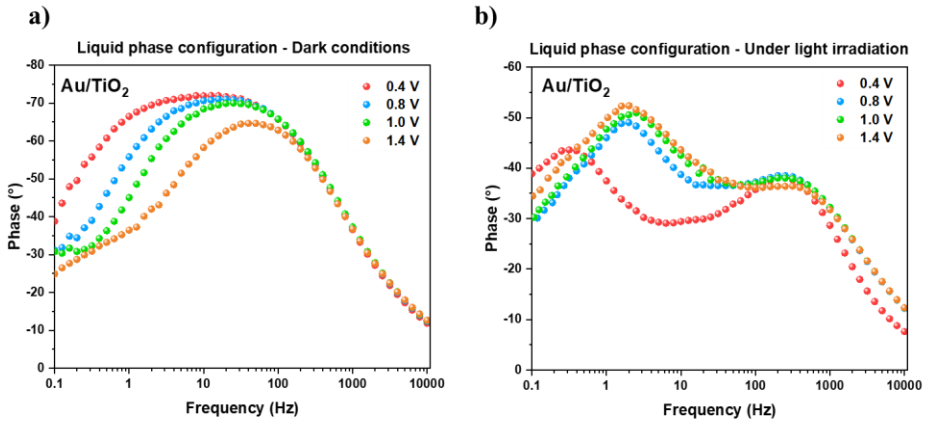

Figure A3.38 *Bode plots of Au/TiO_2 in liquid phase configuration, in (**a**) dark conditions, and (**b**) under light irradiation.*

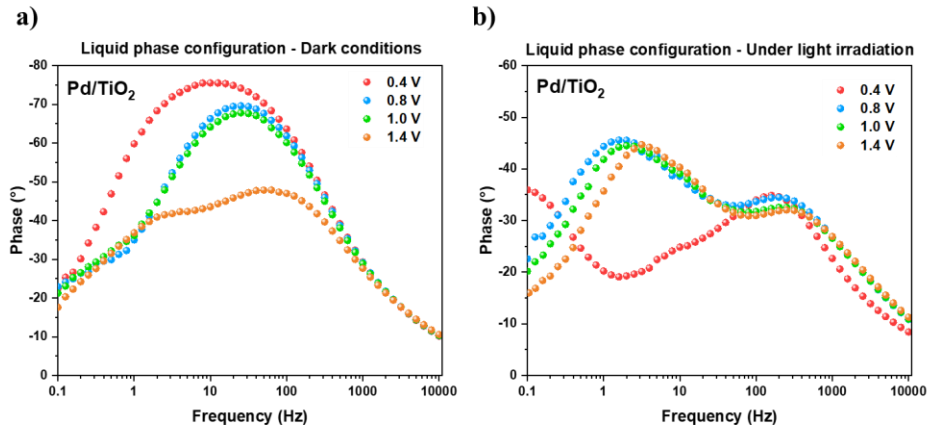

Figure A3.39 *Bode plots of Pd/TiO_2 in liquid phase configuration, in (**a**) dark conditions, and (**b**) under light irradiation.*

DARK CONDITIONS				
Sample	Applied potential	Rs (Ω)	Rct (Ω)	CPE (F)
TiO_2	0.4 V	35.04	91312	4.03E-05
	0.8 V	34.9	97737	4.02E-05
	1.0 V	34.75	99937	3.98E-05
	1.4 V	34.69	105230	3.97E-05
Ag/TiO_2	0.4 V	24.17	34268	7.74E-05
	0.8 V	22.89	59305	6.18E-05
	1.0 V	22.74	73241	5.73E-05
	1.4 V	22.66	82839	5.46E-05
Pd/TiO_2	0.4 V	25.18	51704	2.92E-05
	0.8 V	27.2	86788	3.07E-05
	1.0 V	28.07	109720	3.17E-05

	1.4 V	28.79	123130	3.23E-05
Au/TiO₂	0.4 V	28.65	179330	3.77E-05
	0.8 V	28.18	157120	3.37E-05
	1.0 V	27.91	147590	3.17E-05
	1.4 V	27.66	151590	3.10E-05

Table A3.11 *EIS fitting resulting parameters for gas phase configuration in dark conditions for all samples.*

UNDER LIGHT IRRADIATION				
Sample	Applied potential	Rs (Ω)	Rct (Ω)	CPE (F)
TiO₂	0.4 V	35.9	6456	3.64E-05
	0.8 V	36.08	7692	3.72E-05
	1.0 V	36.28	8314	3.74E-05
	1.4 V	36.75	10869	3.92E-05
Ag/TiO₂	0.4 V	20.31	7564	3.16E-05
	0.8 V	20.1	6255	2.89E-05
	1.0 V	19.78	5069	2.79E-05
	1.4 V	19.63	4990	2.75E-05
Pd/TiO₂	0.4 V	32.03	10773	3E-05
	0.8 V	24.92	9485	2.49E-05
	1.0 V	24.48	9525	2.38E-05
	1.4 V	24.29	9392	2.31E-05
Au/TiO₂	0.4 V	21.99	3030	2.58E-05
	0.8 V	24.08	3346	2.3E-05
	1.0 V	24.18	3446	2.22E-05
	1.4 V	24.03	3479	2.16E-05

Table A3.12 *EIS fitting resulting parameters for gas phase configuration under light irradiation for all samples.*

DARK CONDITIONS						
Sample	Applied potential	Rs (Ω)	Rct' (Ω)	CPE' (F)	Rct (Ω)	CPE (F)
	0.4 V	32.14	56547	2.25E-05	-	-

TiO_2	0.8 V	31.37	22467	2.03E-05	-	-
	1.0 V	31.07	13812	1.97E-05	-	-
	1.4 V	29.81	15090	6.86E-05	955.6	2.97E-05
Ag/TiO_2	0.4 V	34.82	47958	5.79E-05	-	-
	0.8 V	34.18	29399	5.39E-05	-	-
	1.0 V	32.91	17141	5.42E-05	-	-
	1.4 V	33.57	1326	5.45E-05	14911	0.000169
Pd/TiO_2	0.4 V	31.99	22769	2.37E-05	-	-
	0.8 V	29.34	7750	2.85E-05	-	-
	1.0 V	29.34	7907	3.23E-05	-	-
	1.4 V	27.56	815.5	4.00E-05	3006	0.000144
Au/TiO_2	0.4 V	32.9	75163	2.46E-05	-	-
	0.8 V	32.42	30290	2.09E-05	-	-
	1.0 V	31.53	18508	2.00E-05	-	-
	1.4 V	31.82	2094	2.13E-05	11811	8.29E-05

Table A3.13 *EIS fitting resulting parameters for liquid phase configuration in dark conditions for all samples.*

UNDER LIGHT IRRADIATION						
Sample	Applied potential	Rs (Ω)	Rct' (Ω)	CPE' (F)	Rct (Ω)	CPE (F)
TiO_2	0.4 V	26.89	140.8	1.9E-05	2604	1.95E-03
	0.8 V	28.5	119	1.12E-05	2684	1.72E-04
	1.0 V	29.98	96.39	9.56E-06	2875	1.44E-04
	1.4 V	30.28	80.79	8.75E-06	2460	1.25E-04
Ag/TiO_2	0.4 V	28.18	739.7	4.8264E-05	1567	2.42E-04
	0.8 V	29.11	297.3	3.97407E-05	6721	6.15E-04
	1.0 V	28.32	161.7	5.04424E-05	8100	3.81E-04
	1.4 V	32.04	746.8	2.61812E-05	3486	1.51E-04
Pd/TiO_2	0.4 V	25.99	274.1	3.41E-05	2441	4.55E-03
	0.8 V	26.1	136.5	1.68E-05	2883	2.57E-04
	1.0 V	26.13	108	1.39E-05	2395	2.19E-04
	1.4 V	26.59	92.63	1.12E-05	1800	1.67E-04
Au/TiO_2	0.4 V	27.38	236.6	1.87E-05	5297	1.01E-03

	0.8 V	27.84	287.7	1.34E-05	3556	1.28E-04
	1.0 V	28.51	236.6	1.16E-05	3366	1.08E-04
	1.4 V	26.16	233.8	1.47E-05	6495	1.31E-04

Table A3.14 *EIS fitting resulting parameters for liquid phase configuration under light irradiation for all samples.*

3.6.5. Productivity

	Anode products (µmol)				**Cathode products (µmol)**	
	Acetaldehyde		**Acetic Acid**		**Hydrogen**	
Sample	*Gas phase configuration*	*Liquid phase configuration*	*Gas phase configuration*	*Liquid phase configuration*	*Gas phase configuration*	*Liquid phase configuration*
TiO_2	8.41	26.61	0.0004	0.8127	22.21	12.91
Au/TiO_2	4.11	41.97	0.0007	0.8153	15.35	11.57
Ag/TiO_2	8.64	26.77	0.1593	0.0000	8.69	7.91
Pd/TiO_2	8.53	23.01	0.1346	0.0000	6.63	19.75

Table A3.15 *Anodic and cathodic products obtained in gas phase and liquid phase configurations*

4. Plasma-assisted non-oxidative methane coupling (NOCM) in planar and cylindric DBD reactors

4.1 Introduction and scope of the chapter

The conversion of methane to obtain H_2 and high value-added hydrocarbons, has become, in recent years, more and more relevant, and many studies reported the development of alternative technologies to overcome the issue due to the strong bond energy of C–H in methane (434 kJ/mol) that requires high temperatures to be activated[1–4]. One of the most promising technologies is plasma-assisted methane conversion, as in the plasma zone, accelerated high-energy electrons may activate the methane molecules at mild temperatures, through the creation of very active species (radicals, ions, etc.)[5, 6]. The plasma-assisted reaction could lead to a high methane conversion, depending on the experimental conditions, such as plasma power, reactor design, and feed gas composition, but at the same time, the selectivity is still not optimized, with a high formation of undesired carbonaceous byproducts [6–9]. Combining plasma and catalysis could be a good approach to enhance the conversion, modulate the selectivity, and reduce the carbon deposits[10], even if the presence of a catalyst leads to the modification of many reaction parameters (i.e. the local linear velocity and residence time, the local electrical field, the discharge type, etc). Most studied in-plasma catalytic CH_4 coupling used packed beds DBD reactors with catalytic materials in pellets acting also as dielectric[11–13].

The work reported in this chapter was instead focused on the study of the effect of a macro/meso nanostructured catalyst in the form of a thin film (in synergy with plasma) in the reaction of non-oxidative coupling of methane (NOCM). Therefore, titanium oxide nanotubes array-based meshes (TiO_2Nts/Ti mesh), were tested in two different reactors: a conventional tubular DBD plasma reactor and

in a planar DBD reactor. In addition, the effect of light irradiation was investigated. The TiO_2 materials can be excited by external light radiation to generate localized charges on the surface which, positively interacting with the radicals generated in plasma, may increase the selectivity; a specific ordered nanostructure favours the transport of the photo-generated charges and enhances the performances in term of photoactivity. For this reason, this work was focused on an in-plasma catalytic system, because it provided a direct synergistic effect on the reaction.

The first part of the chapter deals with the tests carried out in the conventional tubular DBD plasma reactor (with and without light irradiation), with different morphological parameters of the catalysts, such as the presence of nanostructures and the different sizes of macropores. These experiments were carried out during an abroad period of six months at the Eindhoven University of Technology (TU/e) under the supervision of Prof. F. Gallucci and Dr. S. Li, as part of the PhD ACCESS exchange program. The second part of the chapter is focused on the tests carried out at the CASPE laboratory of the University of Messina, in a new concept of planar DBD reactor built to study the synergy between the confined generation of plasma within the semiconductor and photocatalysis. In addition, the metal nanoparticles (Au, Ag) modified TiO_2 meshes were tested in both DBD reactors (tubular and planar), to understand the role of a co-catalyst deposited on a photoactive material in combination with plasma in pushing the methane non-oxidative coupling.

4.2 Plasma-assisted non-oxidative methane coupling in cylindric DBD reactor

4.2.1 Reactor set-up

Two cylindrical coaxial DBD reactors were used for NOCM tested with two different shells: an alumina tube, with a length of 25 cm, a thickness of 0.265 cm, and an external and internal diameter of respectively 1.23 cm and 0.70 cm (Figure 4.1 a) and a quartz tube with a thickness of 0.1 cm, a length of 25 cm, an external and internal diameter of respectively 0.93 and 0.73 cm (Figure 4.1 b).

In the case of the alumina reactor, the outer electrode was an aluminium foil with a length of 4 cm, and the inner electrode was made of stainless steel with a diameter of 0.16 cm, and it was confined, with the aid of two ceramics rings, to be 4 cm long. In the alumina reactor, the discharge gap was 0.19 cm and the actual plasma volume generated was 1.22 cm^3.

In the case of the quartz tube, the external electrode was a stainless-steel mesh, with a length of 4 cm, and the inner electrode was made of stainless steel with a diameter of 0.16 cm, confined, as in the case of the alumina reactor, using two ceramics rings. In the quartz reactor, the discharge gap was 0.205 cm, and the actual plasma volume was 1.36 cm^3. The TiO_2 mesh catalysts were introduced inside the reactor to cover the length of the external electrode, as shown in Figure 4.2, in which a scheme of side view of the reactor is reported. The TiO_2 pellets were introduced in the same volume as the meshes, with the two ceramic rings at both ends and the insertion of quartz wool in contact with rings, to ensure that the pellets stayed in place.

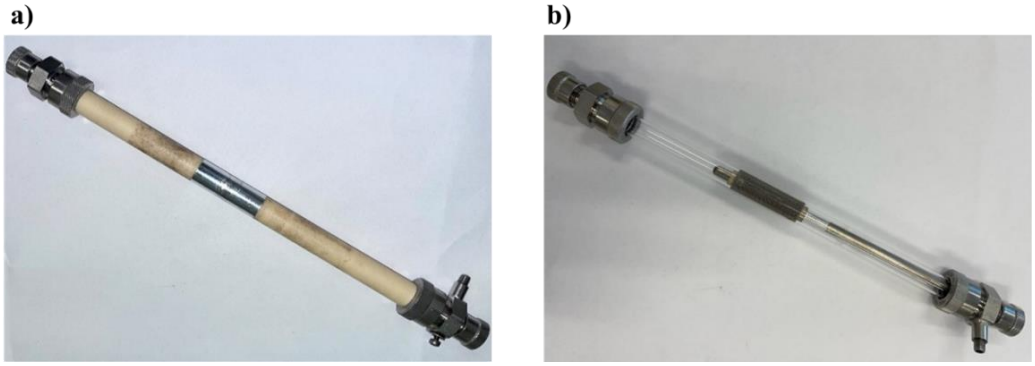

Figure 4.1 *Cylindric DBD reactor used for the tests. In (**a**) alumina tube reactor and in (**b**) quartz tube reactor*

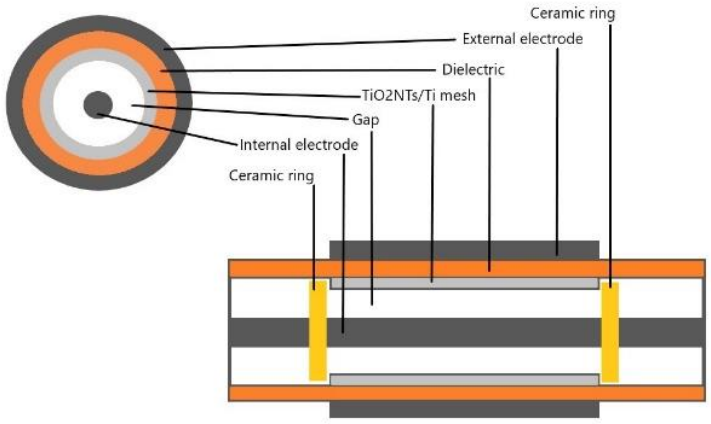

Figure 4.2 *Schematic view of the cylindric DBD reactor*

The outer electrode was connected to the ground via an external capacitor of 100 nF, while the inner electrode, made of stainless steel (0.32 cm diameter, 20 cm length) was connected to the AC high-voltage generator, AFS G05S-150k. The applied voltage was measured by a high-voltage probe and the electrical signals were recorded with a digital oscilloscope (Picoscope 3000 series) (see Figure 4.3). The gas products were analysed by a gas chromatographer (GC Thermo scientific, trace 1310 gas chromatograph) equipped with a flame ionization detector (FID)

and two thermal conductivity detectors (TCD). The reactor was placed inside a Faraday cage to avoid electromagnetic interference.

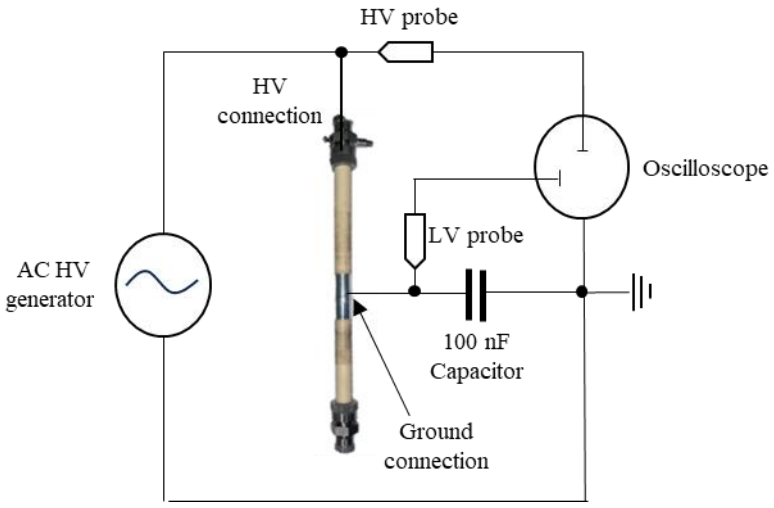

Figure 4.3 *Electrical scheme of the set-up*

To study the effect of light, the plasma set-up was modified with the addition of two 25 W UV B lamps for the illumination of the catalysts, through the stainless-steel mesh (a picture of the experimental set-up is shown in Figure 4.4).

Figure 4.4 *Plasma photocatalysis set-up*

4.2.2 Catalyst preparation

4.2.2.1 Synthesis of TiO_2 nanotubes array on Ti mesh (TiO_2 NTs/Ti)

The synthesis of TiO_2 nanotubes (NTs) on the metallic titanium mesh substrate, was carried out through controlled anodic oxidation, (see Chapter 2 for details), over a Ti gauze with different mesh sizes:

- 60 mesh woven from 0.2 mm diameter
- 80 mesh woven from 0.13 mm diameter

4.2.2.2 Preparation of TiO_2 pellets

Commercial TiO_2 powder was used to produce pellets with 2 cm of diameter. The pellets were smashed in a mortar and sieved with different stainless-steel sieves. Pellets with a diameter between 425 and 630 μm were separated and collected.

4.2.2.3 Au nanoparticles photodeposition

The photodeposition technique was performed to deposit gold on the TiO_2 samples (mesh or pellets), it is a variation of the synthesis reported in chapter 3. The TiO_2NTs mesh samples were dipped in an aqueous solution of the precursor ($HauCl_4 \cdot 3H_2O$) for 30 minutes and then exposed to the radiation of a UV-C lamp for 1 minute. The concentration of the $HAuCl_4 \cdot 3H_2O$ solution was calculated to obtain 0,5 wt% of Au NPs deposited on the substrate.

The TiO_2 pellets were instead dipped in the aqueous solution of the precursor ($HAuCl_4 \cdot 3H_2O$) for 1 minute, then dried and exposed to the radiation of a UV-C lamp for 1 minute.

4.2.2.4 Ag nanoparticles photodeposition

The photodeposition of silver nanoparticles, specified in Chapter 3, has been conducted by dipping the TiO_2NTs mesh samples in a 0.5 M HCl solution, in distilled water, in a 0.1 M $AgNO_3$ solution and finally again in distilled water for

30min (in each solution) at room temperature. This cycle was performed three times. Afterwards, the samples were irradiated with a UV-C lamp for 10 minutes, to reduce Ag^+ ions to metallic Ag species.

The photodeposition of silver nanoparticles on TiO_2 pellets was performed by dipping the pellets in a 0.1 M $AgNO_3$ solution for 1 minute, then the pellets were dried and exposed to the UV-C light for 10 minutes.

All the catalysts were fully characterized before and after the tests, by XRD, and SEM-EDX analysis, to study the effect of the plasma reaction on the morphologies and the surfaces of used catalysts.

4.2.3 Results and discussion

The calculations of the plasma power were made with MATLAB (MATLAB R2021b, The MathWorks, Inc. USA) and a specifically developed script, using the Lissajous method, developed first by Manley[14]. All the equations used for the calculation of methane conversion, hydrogen and hydrocarbon selectivity, specific energy input (SEI) and the carbon balance are reported in the annex.

4.2.3.1. Tests with empty reactor

To estimate the influence of gas mixture composition on the methane conversion and selectivity of the reaction, some NOCM preliminary tests were carried out for 60 minutes, with the empty alumina reactor, using a gas mixture of methane and argon with different volume percentages of methane, at a frequency of 42.4 kHz, varying the peak-to-peak voltage in the range 6.7-7.5 kV to maintain the plasma power at 18.5 ± 1 W. In Table 4.1 the summary of the experimental conditions used is reported.

Test	Flow rate (mL/min)	Vol% CH_4 in Ar	Frequency (kHz)	Time (min)
1	300	20	42.4	60
2	300	25	42.4	60
3	300	30	42.4	60

Table 4.1 *Experimental conditions used for tests with the empty cylindric DBD reactor*

The resulting methane conversion and hydrocarbon selectivity as a function of the volumetric percentage of methane in argon, are displayed in Figure 4.5. It is reported that in DBD plasma systems as the dilution of a gas mixture increases, the conversion also increases, due to the *Penning ionization* and *Penning dissociation*, which are energy transfer reactions from an excited atom or molecule to an atom or molecule in ground state, resulting in the formation of ions or radicals [15–17]. In this specific case, co-feeding Argon with CH_4 can modify the activation mechanism of the reaction, creating excited Ar* species that act as energy carriers, hence enhancing the conversion. The methane conversion increase from 9.3% to 11.5%, as the percentage of Ar increases, thus confirming this effect (Figure 4.5).

The product distribution also slightly changes depending on the amount of methane present in the system[15], with the highest ethane selectivity obtained in the test with 25 vol% of methane. Based on these results, the volume percentage of methane in argon was set at 25%, as a good compromise between methane conversion, ethane selectivity, and the SEI. In Table 4.2 a summary of the results obtained in NOCM tests with empty reactor, including the calculated plasma power and the SEI.

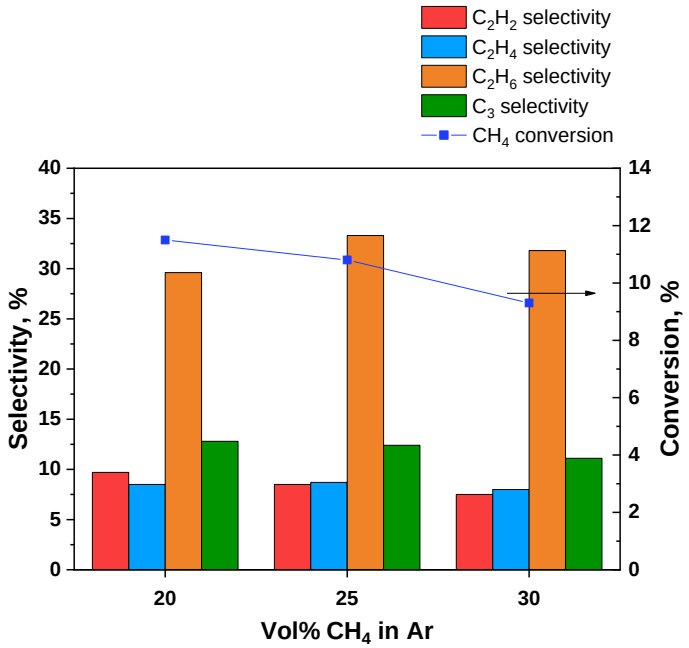

Figure 4.5 *Effect of vol% of CH_4 in Ar on hydrocarbons selectivity (%) and methane conversion (%) in cylindric DBD reactor. The CH_4/Ar mixture flow rate was kept constant at 300mL/min*

Test	CH_4 conv. (%)	H_2 sel. (%)	C_2H_2 sel. (%)	C_2H_4 sel. (%)	C_2H_6 sel. (%)	C_3 sel. (%)	CB (%)	Power (W)	SEI (J/mL)
1	11.5	37.9	9.7	8.5	29.6	12.8	95.5	19.1	3.83
2	10.8	37.6	8.5	8.7	33.3	12.4	96	18.1	3.63
3	9.3	33.6	7.5	8.0	31.8	11.1	96.1	18.2	3.63

Table 4.2 *Effect of vol % of CH_4 on plasma-assisted NOCM reaction with empty reactor. Methane conversion, hydrogen and hydrocarbons selectivity, carbon balance, power and SEI are specified for each test.*

4.2.3.2. The effect of catalysts

The tests of NOCM with different TiO_2-based catalysts (pellets or meshes also loaded with Au or Ag) were carried out using a mixture of 25% of methane in Argon for 60 minutes at a frequency of 42.4 kHz, maintaining the plasma power

at 18.5 ± 1 W. As the catalyst changes the local linear velocity and thus the residence time, the flow rate was set to have the same residence time as the empty reactor test (0.24 s). The input peak-to-peak voltage was varied (in the range of 7.4-8.1 kV) to operate at the same discharge power in all experiments to have comparable results. The experimental parameters used in the tests are summarized in the following table (Table 4.3).

Test	Catalyst	Catalyst Amount (g)	Flow rate (mL/min)	%vol CH_4 in Ar	Frequency (kHz)	Time (min)
2	None	0	300	25	42.4	60
4	TiO_2NTs/Ti 60 mesh	0.6	270	25	42.4	60
5	TiO_2NTs/Ti 80 mesh	0.6	280	25	42.4	60
6	TiO_2 pellets (425-630 μm)	1.5	187	25	42.4	60
7	Au/ TiO_2NTs/Ti 60 mesh	0.6	270	25	42.4	60
8	Ag/ TiO_2NTs/Ti 60 mesh	0.6	270	25	42.4	60
9	Au/ TiO_2NTs/Ti 80 mesh	0.6	280	25	42.4	60
10	Ag/ TiO_2NTs/Ti 80 mesh	0.6	280	25	42.4	60
11	Au/TiO_2 pellets (425-630 μm)	1.5	187	25	42.4	60
12	Ag/TiO_2 pellets (425-630 μm)	1.5	187	25	42.4	60

Table 4.3 *Experimental conditions used for the tests with the catalysts in cylindric DBD reactor*

The introduction of the catalyst in the system produced different Lissajous figure shapes (strictly related to the electrical circuit equivalent to the system[23]) since the presence of a material in a DBD plasma influences the local electrical field changing the electron energy distribution and the chemistry taking place in the plasma[18].

In particular, the shape change is attributed to the combination of surface discharges, formed across the packed bed, and the filamentary discharges, which are the only ones present when the reactor is empty [19–22].

In our case, with the packed-bed reactor, the Lissajous figure had an oval shape in good agreement with the literature [23], due to the catalyst pellets presence (see Figure 4.6 b) while the mesh generated a Lissajous figure shape, intermediate between oval and rectangular (Figure 4.6 c), caused by the physical changes that the catalyst made inside the system.

In Figure 4.6 (a) the typical parallelogram shape of the empty reactor is also reported[23].

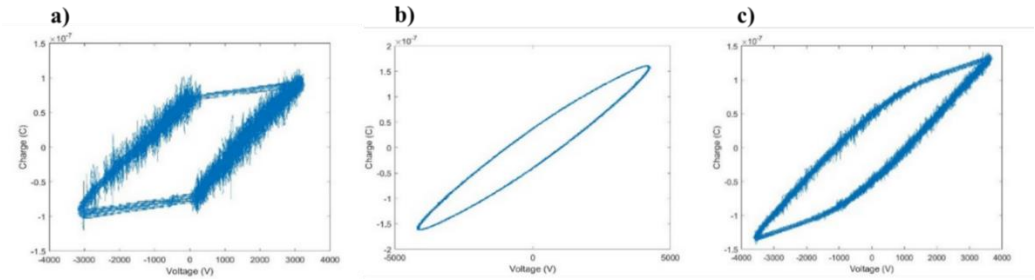

Figure 4.6 *Lissajous figure produced with the empty reactor (**a**), the reactor packed with TiO_2 pellets (**b**), and the reactor packed with the TiO_2 mesh (**c**)*

The methane conversion and selectivity towards C2 and C3 hydrocarbons, obtained using different kinds of TiO_2 catalysts, are reported in Figure 4.7. In detail, figure 4.7 a reports the performances obtained with bare TiO_2NTs on Ti meshes (60 and 80 mesh) compared with TiO_2 pellets, to have useful information about the effect of a different catalyst geometry on the performances. The values with the empty reactor are also reported as a comparison. Observing Figure 4.8 a, it is possible to notice the beneficial role of the mesh that allowed to enhance the conversion compared to TiO_2 pellets, probably due to the presence of the specific nanostructure.

There were no effects related to the presence of a catalyst on the conversion since the highest conversion value (10.8%) was found with the empty reactor, but this was probably due to hydrogenation reactions of the methyl ions on the catalyst surface, as reported also by Garcia-Moncada et al. [24]. Moreover, was already observed by fluid modelling studies that material with higher dielectric constants in this kind of reactor, caused a reduction of electron density decreasing the conversion rate[25].

In addition, Au and Ag/TiO_2NTs/Ti meshes were tested to study the influence of a co-catalyst with specific plasmonic behaviour in NOCM reaction, and the results are reported in Figure 4.7 b (60 mesh) and c (80 mesh). The introduction of the metals on TiO_2NTs/Ti 60 and 80 mesh substrates had a negligible effect on the conversion. Figure 4.8 d compares instead the performances of Au and Ag/TiO_2 pellets with the bare TiO_2 support, to investigate the effect of a specific metal without the presence of ordered nanostructured meso/macroporous TiO_2 thin film. The deposition of the metal nanoparticles on the TiO_2 pellets increased the methane conversion and the silver-modified catalysts allowed to double the conversion value (4.6% vs.8.2%).

When the selectivity was investigated, several effects due to the introduction of the catalysts in the reactor could be observed. As reported in many papers, ethane is the main product in plasma-assisted NOCM, with a low energy input [26, 27]. In all the tests, the presence of a catalyst (pellets or meshes) inside the reactor changed the distribution of products compared to the empty reactor, increasing C_2H_2 selectivity, as shown in Figure 4.7, even if ethane is always the most abundant product[28]. A different behaviour was noticed with bare TiO_2 pellets. In this case, there was a slightly higher selectivity towards acetylene compared to ethane (13.3% of C_2H_2 selectivity vs. 12.2% of C_2H_6 selectivity). As regards the effect of TiO_2NTs/Ti mesh-based catalysts, it was possible to observe a higher selectivity towards C_2H_6 and C3 hydrocarbons (see Figure 4.7 a) with respect to

the reactor filled with the TiO_2 pellets. Probably the presence of TiO_2 pellets enhanced the probability of the collision between dehydrogenated species with the subsequent formation of unsaturated C2 species, reducing the formation of higher chain hydrocarbons[29]. Regarding the presence of metal nanoparticles on the catalysts, it was evident that metals changed the selectivity towards all the products, compared to the bare TiO_2 samples and especially the silver-modified catalysts (pellets or meshes) showed a higher ethane selectivity compared to gold-modified samples. An explanation of this behaviour could be the SPR effect of the metal nanoparticles, more significant with silver, that leads to the direct coupling of methane through the collision of molecules with high energy electrons[30].

A summary of all the results obtained in the NOCM tests with different catalysts, including carbon balance, calculated plasma power and SEI, is reported in Table 4.4.

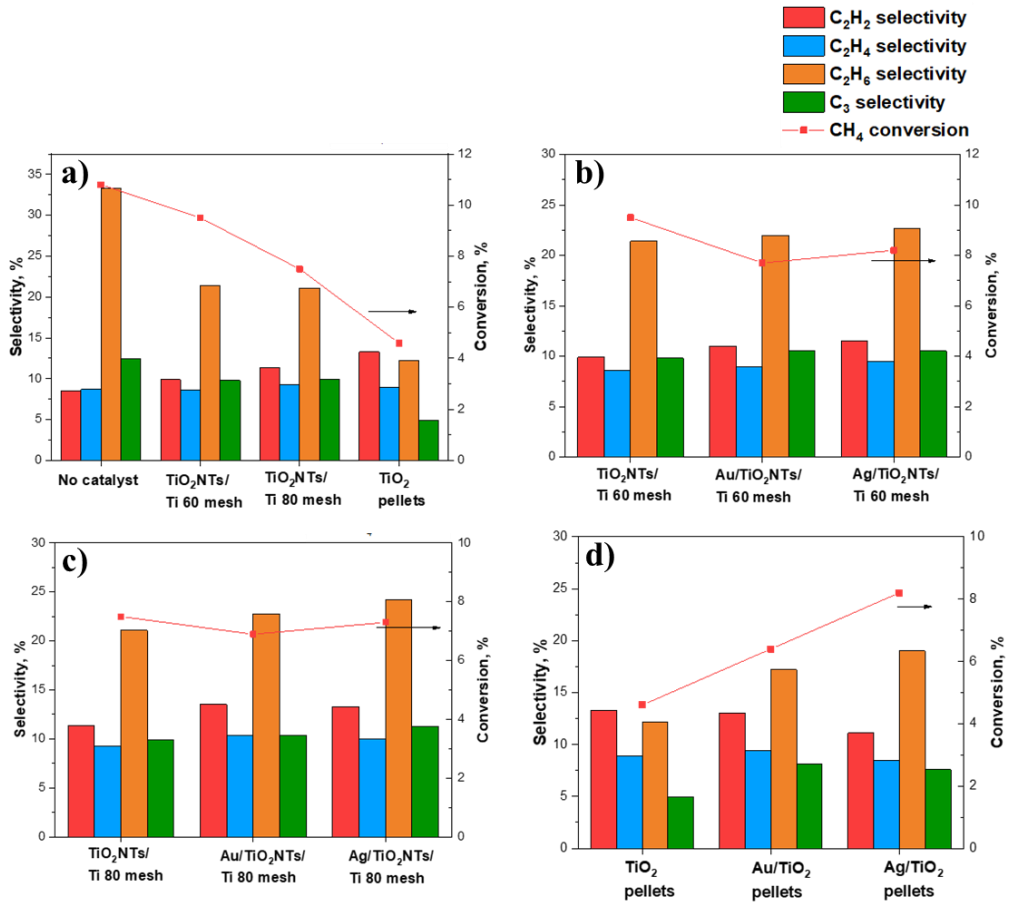

Figure 4.7 *Methane conversion % and hydrocarbons selectivity %. for tests with TiO_2-based bare supports (pellets and meshes) in a), and the comparison with Ag, Au metal supported catalysts in b), c) and d) in the cylindric DBD reactor*

Catalyst	CH_4 conv. (%)	H_2 sel. (%)	C_2H_2 sel. (%)	C_2H_4 sel. (%)	C_2H_6 sel. (%)	C_3 sel. (%)	CB (%)	Power (W)	SEI (J/mL)
None	10.8	37.9	8.5	8.7	33.3	12.4	96	18.1	3.63
TiO_2NTs/Ti 60 mesh	9.5	37.6	9.9	8.6	21.4	9.8	95.2	16.9	3.75
TiO_2NTs/Ti 80 mesh	7.5	39.3	11.4	9.3	21.1	9.9	96.4	18.5	3.96
TiO_2 pellets	4.6	32.1	13.3	8.9	12.2	4.9	97.2	18.0	5.77
Au/TiO_2NT	7.7	40	11	8.9	22	10.5	96.3	18.5	4.11

s/Ti 60 mesh									
Ag/ TiO_2NTs/Ti 60 mesh	8.2	40.9	11.5	9.5	22.7	10.5	96.2	18.5	4.11
Au/ TiO_2NTs/Ti 80 mesh	6.9	44	13.5	10.4	22.8	10.4	97	16.2	3.47
Ag/ TiO_2NTs/Ti 80 mesh	7.3	44.5	13.3	10	24.2	11.3	97	16.9	3.62
Au/TiO_2 pellets	6.4	38.3	13	9.4	17.2	8.1	96.7	18.2	5.83
Ag/TiO_2 pellets	8.2	34.9	11.1	8.5	19	7.6	95.6	21	6.74

Table 4.4 *Effect of the catalysts on the performances in plasma-assisted NOCM reaction in cylindric DBD reactor. Methane conversion, hydrogen and hydrocarbons selectivity, carbon balance, power and SEI are specified for each test.*

4.2.3.3. Carbon deposition

During the plasma activation of methane, it is generally reported the formation of carbonaceous deposits that mostly increases with the conversion [24]. In fact, after the tests, it was noticed a carbon deposition on the reactor and on the stainless-steel inner electrode. Figure 4.8 a shows the plasma formation zone of the stainless-steel electrode completely covered with carbon after the reaction carried out with the empty reactor. Furthermore, some carbon filaments can be seen in the internal part of the alumina tube (Figure 4.9). Combining plasma and catalysis seems to be a promising approach in which the catalyst can decrease the formation of deposits [6]. As expected, the introduction of the catalysts helped to prevent the carbon deposition on the inner electrode and on the tube, but with a different behaviour depending on the type of catalyst used. By using TiO_2NTs mesh, just a little part of the electrode was covered with carbon as can be seen in Figure 4.8 b probably due to the particular way in which the mesh was located around the electrode. The deposition of carbon on TiO_2NTs mesh was confirmed by SEM-EDX performed before and after the reaction (Figure 4.10 and Figure 4.11).

Meanwhile, by using the TiO_2 pellets, there was no evidence of carbon deposition on the stainless-steel electrode (Figure 4.8 c).

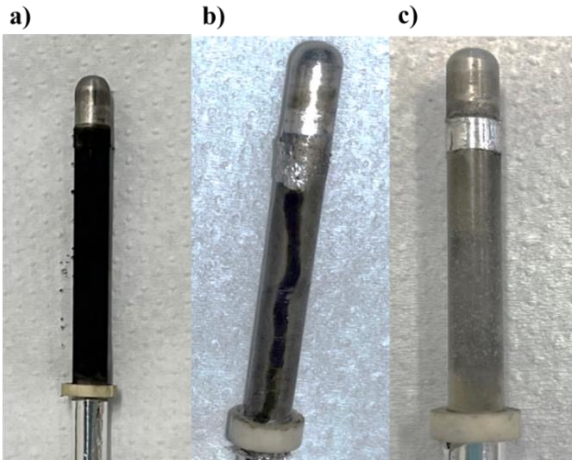

Figure 4.8 *Inner SS electrode after the reaction without catalysts (**a**), mesh-based catalysts (**b**), with particles-based catalysts (**c**)*

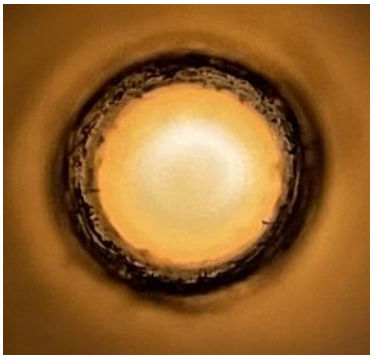

Figure 4.9 *Internal part of the alumina tube after the reaction with an empty reactor*

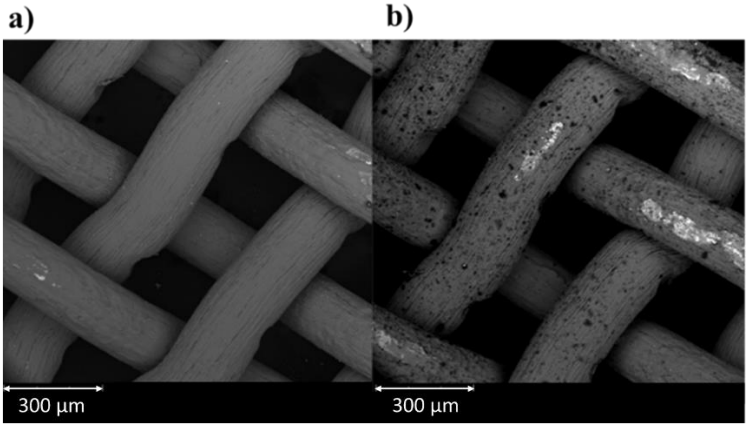

Figure 4.10 *SEM images of the TiO_2NTs/Ti 60 mesh before (**a**) and after the test (**b**)*

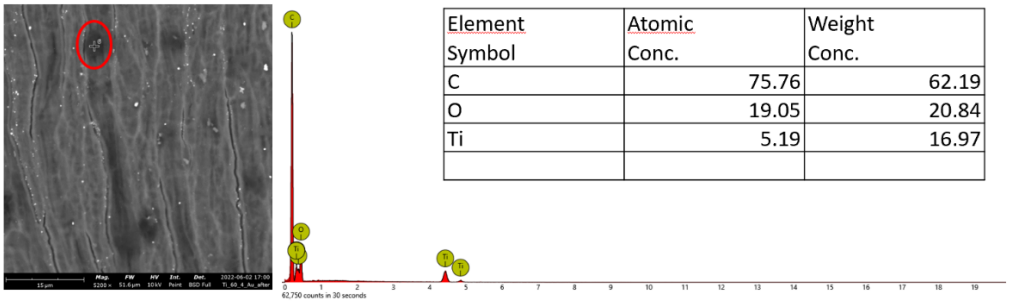

Element Symbol	Atomic Conc.	Weight Conc.
C	75.76	62.19
O	19.05	20.84
Ti	5.19	16.97

Figure 4.11 *EDX point analysis (red circle) of the sample TiO_2NTs/Ti 60 mesh after the test. On the right is the table with the atomic and weight percentages of the elements.*

4.2.3.4. Plasma photocatalytic tests

To study the effect of coupling plasma and photocatalysis, tests using external lamps in combination with plasma were also performed. Some preliminary tests using only light (without generating a plasma) were performed to understand better the role of TiO_2 photocatalytic materials in the NOCM reaction. All the tests were carried out in the experimental conditions reported in the following table, varying the peak-to-peak voltage (7-7.5 kV) to maintain the power in the range of 16-18.5 W throughout the tests (Table 4.5). Using only light, no hydrogen and other products were detected with all the tested photocatalysts. This is probably due to the low irradiance and power of the UV B lamps used (25 W each, with an irradiance value of 218 μW cm^{-2}) not sufficient to activate the TiO_2 photo responsive materials.

Test	Catalyst	Condition	Quantity of catalyst (g)	Flow rate (mL/min)	%vol CH4 in Ar	Frequency (kHz)	Time (min)
1	no	Plasma	0	300	25	42.4	60
2	TiO_2/Ti 60 mesh	Plasma	0.6	270	25	42.4	60
3	TiO_2/Ti 60 mesh	Plasma+light	0.6	270	25	42.4	60
4	Au/TiO_2NTs/Ti 60 mesh	Plasma+light	0.6	270	25	42.4	60
5	Au/TiO_2NTs/Ti 60 mesh	Plasma	0.6	270	25	42.4	60

6	Ag/TiO_2NTs/Ti 60 mesh	Plasma+light	0.6	270	25	42.4	60
7	Ag/TiO_2NTs/Ti 60 mesh	plasma	0.6	270	25	42.4	60

Table 4.5 *Experimental conditions used for the tests with catalysts and light irradiation in cylindric DBD reactor*

The CH_4 conversion and selectivity obtained in the plasma photocatalytic tests, as well as the carbon balance, calculated plasma power and SEI, are reported in Table 4.6.

Figure 4.13 shows the conversion and the selectivity (%) towards ethane for TiO_2NTs/Ti 60 mesh and Au and Ag modified TiO_2NTs/Ti (60 mesh). The use of light in combination with plasma allowed to increase in the conversion of methane for the bare TiO_2NTs/Ti 60 mesh and for Au/TiO_2NTs/Ti 80 mesh. No differences were observed for silver.

Light irradiation had instead a strong effect in changing the selectivity towards ethane with all photocatalysts. The highest ethane selectivity was observed with Au-modified photocatalyst, and this could be related to the presence of this particular metal. Lang et al. [31] working on photocatalytic NOCM found that Au/TiO_2 among other metal-modified TiO_2 catalysts, lead to the highest yield. In their work, the mechanism of the formation of ethane was also evaluated, which involves the adsorption of methane on the Au surface and the formation of methyl anion and a subsequent methyl radical formation, shown in Figure 4.12.

$$2CH_4 \xrightarrow{\text{adsorption}} 2^*CH_4 \xrightarrow{e^-} \begin{cases} 2CH_3^- \xrightarrow{h^+} 2^\bullet CH_3 \rightarrow C_2H_6 \\ 2H^\bullet \rightarrow H_2 \end{cases}$$

Figure 4.12 *Photocatalytic non-oxidative coupling of methane on gold, involving a methyl anion-radical mechanism. Reproduced with permission from ref.* [31]

In DBD plasma the main reaction pathway that led to the formation of ethane also involves two methyl radicals, which are generated by the electron impact dissociation of methane[26]. This mechanism could be enhanced by the electrons provided by the photocatalyst excited through the light irradiation in a photocatalytic system. The same effect was noticed also towards C3 products, suggesting a similar effect of the plasma and photoactivation coupling (see Table 4.6).

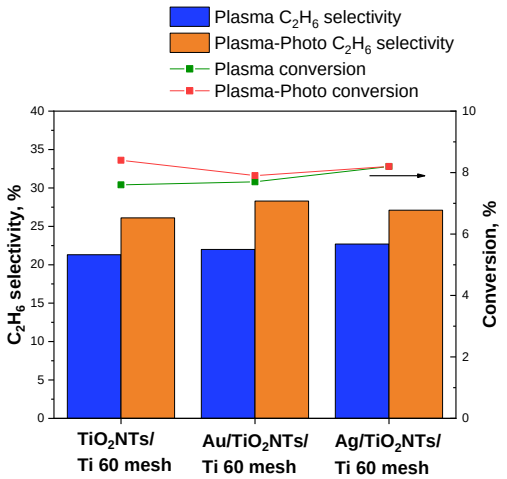

Figure 4.13 *Effect of light irradiation on ethane selectivity (%) and methane conversion for TiO_2NTs/Ti mesh, Au/TiO_2Nts/Ti mesh, and Ag/TiO_2Nts/Ti mesh in cylindric DBD reactor*

Catalyst	Condition	CH_4 conversion (%)	H_2 selectivity (%)	C_2H_2 selectivity (%)	C_2H_4 selectivity (%)	C_2H_6 selectivity (%)	C_3 selectivity (%)	Carbon balance (%)	Power (W)	SEI (J/mL)
no	Plasma	14.8	37.4	6.2	5.1	30.5	14.8	93.6	18.1	3.62
TiO_2/Ti 60 mesh	Plasma	7.6	39.6	11.6	9.3	21.3	9.9	96.3	16	3.19
TiO_2/Ti 60 mesh	Plasma+light	8.4	43.6	10.9	7.9	26.1	13.9	96.6	16.6	3.68
Au/TiO_2NTs/Ti 60 mesh	Plasma	7.7	40	11	8.9	22	10.5	96.3	17.1	3.8
Au/TiO_2NTs/Ti 60 mesh	Plasma+light	7.9	47.4	12.2	8.6	28.3	14.9	97.1	18.5	4.11
Ag/TiO_2NTs/Ti 60 mesh	Plasma	8.2	40.9	11.5	9.5	22.7	11.5	96.2	17.3	3.84

Ag/TiO_2NTs/Ti 60 mesh	Plasma+light	8.2	44.2	11.8	8.1	27.1	15.1	96.9	18.5	4.11

Table 4.6 *Effect of the light irradiation on plasma-assisted NOCM reaction with different catalysts in cylindric DBD reactor. Methane conversion, hydrogen and hydrocarbons selectivity, carbon balance, power and SEI are specified for each test.*

4.3 Plasma-assisted non-oxidative methane coupling in planar DBD reactor

4.3.1 Reactor design

TiO_2NTs on Ti meshes (also modified with metal), were then tested in NOCM reaction using a home-made planar DBD reactor with no gap between the dielectric material and the electrodes.

From the first prototype (scheme in Figure 4.14), the reactor was substantially upgraded with many design adjustments to ensure system inertness and prevent short circuits, assuring a good stabilization of plasma during the process. The first prototype was made of Macor®, a machinable glass ceramic material. The core of this reactor was a two-planar mesh-type electrode system through which the gas flows, with one of the two electrodes reconstructed in the form of a thin TiO_2NTs array (connected to the ground) and an alumina porous, thin disk between the two-mesh acting as a dielectric barrier. The other electrode, a stainless steel (SS) mesh, was connected to the high voltage. The reactor configuration allowed the illumination of the photoactive electrode (based on TiO_2 NTs array) by a quartz window to create the synergies between light illumination and (micro)plasma to be investigated. During the first experiments, some technical problems occurred and short-circuit currents were directly observed, damaging the alumina membrane and Ti mesh due to the specific geometrical configuration of the reactor.

To address these issues, a new reactor with a very compact design and a more homogeneous distribution of the gas was designed and constructed. A picture during a test is reported in Figure 4.16. In this case within the plasma zone, it was used alumina instead of Macor®, with a "cap-like" geometry to lengthen the electron path and prevent short-circuits effectively. The dielectric strength of alumina is more stable and less dependent on temperature variations with respect to Macor®. Essentially, the current version of the reactor consists of two parts (schematized in Figure 4.15): 1) a section made in Macor with the quartz window for the illumination of the catalyst (consenting to study the interaction between light and non-thermal plasma), the gas inlet and outlet, and a SS wire in contact with the electrode as ground 2) an alumina section (plasma zone), where the catalyst is placed, with a SS disc acting as High Voltage (HV), directly connected to the AC power supply.

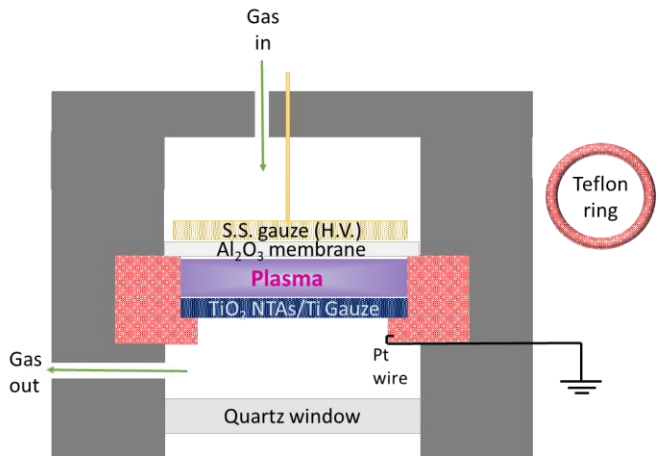

Figure 4.14 *Scheme of the first prototype of the DBD planar reactor*

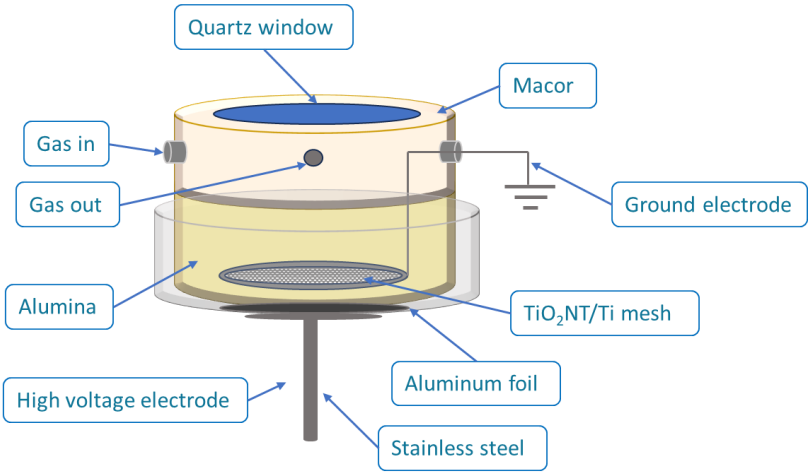

Figure 4.15 *Scheme of the home-made DBD plasma-photocatalytic reactor*

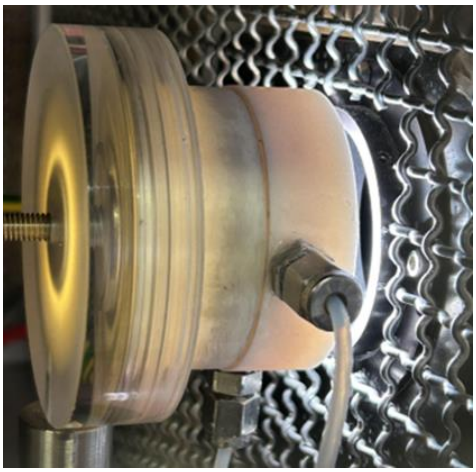

Figure 4.16 *Side view of the plasma-photocatalytic reactor, during a plasma-photocatalytic test*

The setup is illustrated in Figure 4.17. In detail, the TiO_2NTs/Ti mesh electrode was connected to the ground, while the stainless-steel electrode was connected to the high-voltage generator (RedLine Technologies-G2000). The applied voltage was measured by a high-voltage probe and the current with a Rogowski coil, and all the electrical signals were recorded with a digital oscilloscope (Picoscope 6402D). The products were detected and quantified with a Gas Chromatographer (Agilent 8890, Agilent Technologies Italia Spa) equipped with TCD and FID detectors for the quantification of the hydrogen and hydrocarbons. The reactor

was placed inside a Faraday cage to avoid electromagnetic interference. The light irradiation was carried out through the reactor quartz window using a 300W Xe arc lamp (Lot Oriel).

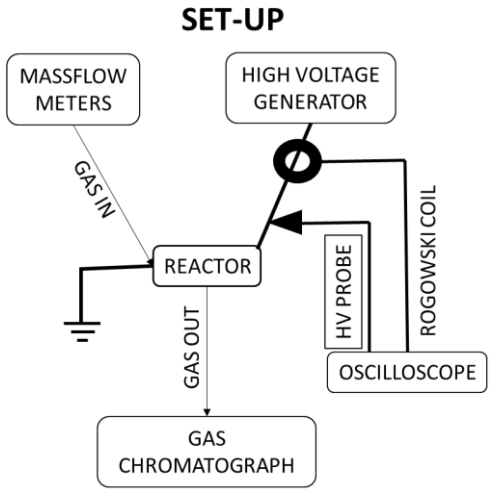

Figure 4.17 *Scheme of the experimental set-up*

4.3.2 Catalyst preparation

4.3.2.1 Synthesis of TiO_2 nanotubes array on Ti mesh (TiO_2NTs/Ti)

The synthesis of TiO_2 nanotubes (NTs) on the metallic titanium mesh substrate, was carried out through controlled anodic oxidation, over a Ti gauze 80 mesh woven from 0.13 mm diameter.

4.3.2.2 Au nanoparticles electrodeposition

The gold nanoparticles electrodeposition, described in Chapter 3, was performed in a two-electrode cell made in Teflon, using the sample as the working electrode and a standard Pt electrode as the counter electrode. The potential applied was -70 V for 45 minutes, in an aqueous solution of gold precursor ($HAuCl_4$ $3H_2O$, 0.1 mM).

4.3.3 Results and discussion

The power dissipated by the plasma, due to the high voltage generator, was calculated using the high voltage and current measurements, with MATLAB (MATLAB R2021b, The MathWorks, Inc. USA) and a specifically developed script.

Methane conversion, hydrogen and hydrocarbon selectivity and the SEI (Specific energy input) were calculated with the equations reported in the annex.

Non-oxidative coupling of methane (NOCM) has been performed using the TiO_2 nanotubes on Ti mesh electrodes (also modified with gold) in dark conditions and under light irradiation. The tests were carried out for 30 minutes with a mixture of 10 vol% of methane in argon with a flow rate of 10 mL/min. The frequency was set at 22.07 kHz for all the experiments.

4.3.3.1 The effect of plasma power

Initially, the bare TiO_2NTs/Ti mesh in the absence of light has been tested, varying the intermediate voltage of the generator to produce different calculated plasma power values, ranging from 2.6 to 4.2 W. All the experimental parameters are listed in Table 4.7.

Sample	Intermediate voltage (V)	Power (W)	Flowrate (mL/min)	Vol% CH_4 in Ar	Frequency (kHz)
TiO_2NTs/Ti mesh	75	2.6	10	10	22.07
TiO_2NTs/Ti mesh	100	3.3	10	10	22.07
TiO_2NTs/Ti mesh	125	3.8	10	10	22.07
TiO_2NTs/Ti mesh	150	4.2	10	10	22.07

Table 4.7 *Experimental conditions used for tests with TiO_2NTs/Ti mesh (80 mesh) at different plasma power in DBD planar reactor*

As the power increased, the conversion of methane also increased, as can be noticed in Figure 4.18. The product ratio also shifted, notably a reduction in

ethylene selectivity was observed thus plasma power has a specific influence on the reactions which take place inside the plasma, and this can result in different product selectivity [26]. In Table 4.8 a summary of all the results obtained at different plasma power, in a planar DBB reactor, including the specific energy input, is reported.

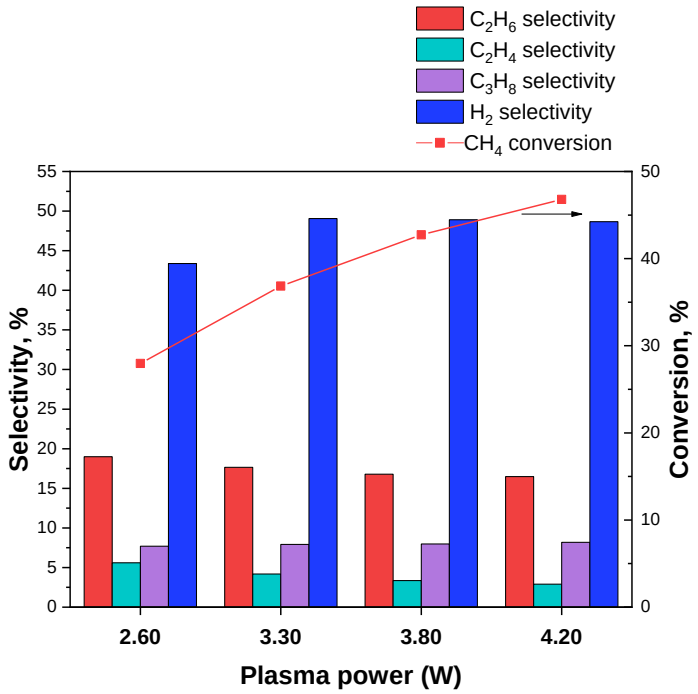

Figure 4.18 *The effect of plasma power on the methane conversion % and selectivity% (to H_2 and C2 C3 hydrocarbons) for TiO_2NTs/Ti 80 mesh in DBD planar reactor*

Sample	Power (W)	SEI (J/mL)	Methane Conv.(%)	Ethane sel.(%)	Ethylene sel. (%)	Propane sel. (%)	Hydrogen sel. (%)
TiO_2NTs/Ti mesh	2.6	15.7	28.0	19.0	5.6	7.7	43.4
TiO_2NTs/Ti mesh	3.3	19.7	36.8	17.7	4.2	7.9	49.0
TiO_2NTs/Ti mesh	3.8	22.8	42.7	16.8	3.4	7.8	48.9
TiO_2NTs/Ti mesh	4.2	25.4	46.8	16.5	2.9	8.2	48.7

Table 4.8 *The effect of plasma power and SEI on the plasma-assisted NOCM reaction in the DBD planar reactor for TiO_2NTs/Ti 80 mesh*

4.3.3.2 The effect of catalysts in plasma-photocatalytic tests

To investigate the impact of gold nanoparticles on plasma-assisted NOCM reaction, tests were conducted with the TiO_2NTs/Ti mesh and the Au/TiO_2NTs/Ti mesh, in dark conditions, at the same plasma power. Finally, experiments in the presence of light irradiation were carried out with Au/TiO_2NTs/Ti mesh to study the effect of the combination of plasmonic metal, plasma, and light. The experimental conditions used are summarized in Table 4.9.

Sample	Light	Flow rate (L/min)	Frequency (kHz)	Vol% CH_4 in Ar
TiO_2NTs/Ti mesh	OFF	0.010	22.07	10
Au/TiO_2NTs/Ti mesh	OFF	0.010	22.07	10
Au/TiO_2NTs/Ti mesh	ON	0.010	22.07	10

Table 4.9 *Experimental conditions used for tests with TiO_2NTs/Ti mesh and Au/TiO2NTs/Ti mesh in dark and under light irradiation in a DBD planar reactor*

Observing the results obtained in dark conditions, (see Figure 4.18) it is evident the beneficial role of gold in plasma-assisted NOCM reaction. The gold-modified sample in fact, strongly enhanced the methane conversion that reached a value of almost 43%, with a modulation also in the selectivity, pushing towards the ethylene production. No carbon deposits were detected in all the experiments, so confirming the importance of a microdischarge zone.

Figure 4.19 instead reported the influence of light irradiation in the methane conversion and selectivity for the Au/TiO_2Nts/Ti mesh photocatalyst. The exposition of the Au-based catalyst to light, resulted in a further increase of the conversion of methane, with modification in the selectivity towards ethane and propane, which showed an increment as well. The combination of local surface plasma resonance (SPR) effect localized on Au and ultraviolet-light-induced effect on TiO_2, (combined with non-thermal plasma) enhanced the photocatalytic activity due to a combination of photogenerated holes (on the support) with the

hot electrons (on Au), with higher capability to activate the CH_4 molecules. This behaviour is similar to that recently evidenced for Ag/TiO_2 photocatalyst in the oxidative coupling of methane reaction, so corroborating this hypothesis[32].

All the results obtained in the tests in dark and under light irradiation in DBD planar reactor are summarized in Table 4.10.

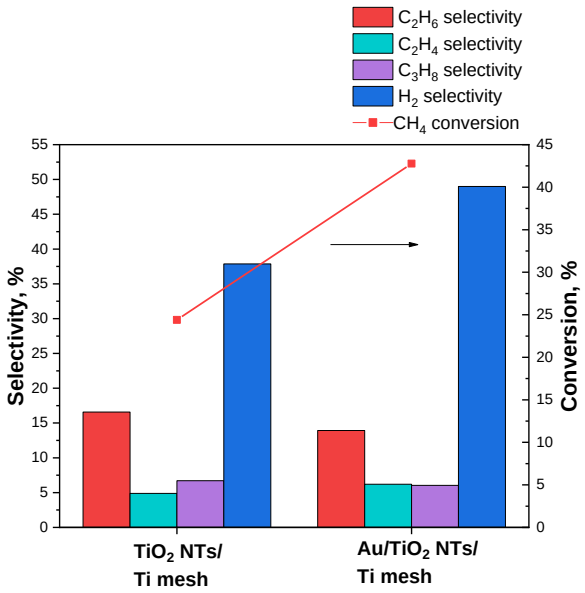

Figure 4.18 *The effect of gold on the methane conversion % and selectivity% (to H_2 and C2 C3 hydrocarbons) in DBD planar reactor in dark conditions*

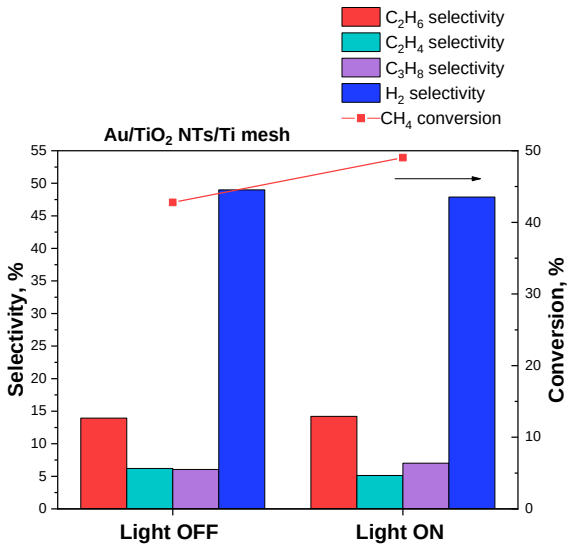

Figure 4.19 *Effect of the light irradiation on methane conversion % and selectivity % (to H_2 and C2 C3 hydrocarbons) for the Au/TiO_2NTs/Ti mesh in DBD planar reactor*

Sample	Light	SEI (J/mL)	Power (W)	Methane Conversion (%)	Ethane Selectivity (%)	Ethylene Selectivity (%)	Propane Selectivity (%)	Hydrogen Selectivity (%)
TiO_2NTs/ Ti mesh	OFF	13.6	2.27	24.4	16.6	4.9	6.7	37.9
Au/TiO_2NTs/ Ti mesh	OFF	13.6	2.27	42.8	13.9	6.2	6.1	49.0
Au/TiO_2NTs/ Ti mesh	ON	13.6	2.27	49.0	14.2	5.1	7.0	47.9

Table 4.10 *Effect of the light irradiation on plasma-assisted NOCM reaction with TiO_2Nts/Ti mesh and Au/ TiO_2Nts/Ti mesh catalyst*

4.4 Conclusions

Plasma-assisted non-oxidative coupling of methane (NOCM) with titanium dioxide nanotube-based catalysts, was performed using two different plasma reactor configurations, a cylindric DBD reactor and a planar DBD reactor. Both these configurations allowed the irradiation of the sample, to further test the effect

of a combination between photo and plasma catalysis. Generally, the observed CH_4 conversion was essentially initiated by the plasma discharge and not by a specific catalytic effect of materials used as electrodes, differently from the product distribution.

By using the conventional cylindric DBD plasma reactor, the presence of catalysts reduced the deposition of carbon on the reactor and strongly changed the selectivity. Among all the catalysts the TiO_2Nts/Ti 60 mesh showed the highest methane conversion, with a greater selectivity towards C_2H_6 and C_3 products. TiO_2 pellets, on the contrary, showed a higher C_2H_2 selectivity compared to the empty reactor and to the other catalysts. The presence of a metal, Ag in particular, allowed to push further the selectivity for both meshes and pellets catalysts.

The effect of light was evident in observing the selectivity. Light irradiation affected modulation of the selectivity, in particular towards ethane, with an improvement with all the tested catalysts (TiO_2NTs/Ti mesh and metal-modified TiO_2NTs catalysts).

Analysing the results obtained with the planar DBD reactor, it is evident the beneficial role of gold in plasma-assisted NOCM reaction. The gold-modified sample in fact, strongly enhanced the methane conversion that reached a value of almost 43%, with a change also in the selectivity, pushing towards the ethylene production and this effect was even more marked under light irradiation. The influence of the light is thus very dependent on the geometry of the reactor.

The results obtained in this study demonstrated that the use of non-thermal plasma (combined with catalysis) is an attractive possibility to convert methane at low temperatures and obtain different products. This process is a rather complex reaction, and many different parameters influence the mechanism, particularly if photo and plasma catalytic effects are combined.

The use of a porous meso/macro 3D hierarchical structure, as the titanium dioxide nanotubes on a titanium mesh, can be beneficial in terms of both conversion and

selectivity, and the integration of metal plasmonic NPs can further enhance the performances. The use of light in combination with plasma may further influence the selectivity and the conversion in the NOCM reaction, due to the combination of a local SPR effect on the metal and the photoelectric effect induced from irradiation on TiO_2-based material, and this is strongly dependent on the specific geometry of the plasma reactor.

4.5 References

[1] J. R. H. Ross, A. N. J. van Keulen, M. E. S. Hegarty, and K. Seshan, 'The catalytic conversion of natural gas to useful products', *Catal Today*, vol. 30, no. 1–3, pp. 193–199, Jun. 1996, doi: 10.1016/0920-5861(96)00035-1.

[2] X. Tao, M. Bai, X. Li, H. Long, S. Shang, Y. Yin, and X. Dai, 'CH_4–CO_2 reforming by plasma – challenges and opportunities', *Prog Energy Combust Sci*, vol. 37, no. 2, pp. 113–124, Apr. 2011, doi: 10.1016/j.pecs.2010.05.001.

[3] S. M. Sadrameli, 'Thermal/catalytic cracking of hydrocarbons for the production of olefins: A state-of-the-art review I: Thermal cracking review', *Fuel*, vol. 140, pp. 102–115, Jan. 2015, doi: 10.1016/j.fuel.2014.09.034.

[4] L. Chen, X.-W. Zhang, L. Huang, and L.-C. Lei, 'Partial oxidation of methane with air for methanol production in a post-plasma catalytic system', *Chemical Engineering and Processing: Process*

Intensification, vol. 48, no. 8, pp. 1333–1340, Aug. 2009, doi: 10.1016/j.cep.2009.06.007.

[5] X. Tu, J. C. Whitehead, and T. Nozaki, Eds., *Plasma Catalysis*, vol. 106. Cham: Springer International Publishing, 2019. doi: 10.1007/978-3-030-05189-1.

[6] N. García-Moncada, T. Cents, G. van Rooij, and L. Lefferts, 'Minimizing carbon deposition in plasma-induced methane coupling with structured hydrogenation catalysts', *Journal of Energy Chemistry*, vol. 58, pp. 271–279, Jul. 2021, doi: 10.1016/j.jechem.2020.09.006.

[7] S. K. Kundu, E. M. Kennedy, V. V. Gaikwad, T. S. Molloy, and B. Z. Dlugogorski, 'Experimental investigation of alumina and quartz as dielectrics for a cylindrical double dielectric barrier discharge reactor in argon diluted methane plasma', *Chemical Engineering Journal*, vol. 180, pp. 178–189, Jan. 2012, doi: 10.1016/j.cej.2011.11.039.

[8] S. Jo, D. Hoon Lee, and Y.-H. Song, 'Product analysis of methane activation using noble gases in a non-thermal plasma', *Chem Eng Sci*, vol. 130, pp. 101–108, Jul. 2015, doi: 10.1016/j.ces.2015.03.019.

[9] S. Zhang, Y. Gao, H. Sun, H. Bai, R. Wang, and T. Shao, 'Time-resolved characteristics and chemical kinetics of non-oxidative methane conversion in repetitively pulsed dielectric barrier discharge plasmas', *J Phys D Appl Phys*, vol. 51, no. 27, p. 274005, Jul. 2018, doi: 10.1088/1361-6463/aac5ad.

[10] T. Nozaki and K. Okazaki, 'Non-thermal plasma catalysis of methane: Principles, energy efficiency, and applications', *Catal*

Today, vol. 211, pp. 29–38, Aug. 2013, doi: 10.1016/j.cattod.2013.04.002.

[11] K. Van Laer and A. Bogaerts, 'Influence of Gap Size and Dielectric Constant of the Packing Material on the Plasma Behaviour in a Packed Bed DBD Reactor: A Fluid Modelling Study', *Plasma Processes and Polymers*, vol. 14, no. 4–5, Apr. 2017, doi: 10.1002/ppap.201600129.

[12] S. Jo, D. Hoon Lee, W. Seok Kang, and Y.-H. Song, 'Effect of packing material on methane activation in a dielectric barrier discharge reactor', *Phys Plasmas*, vol. 20, no. 12, Dec. 2013, doi: 10.1063/1.4843875.

[13] W. Wang, H.-H. Kim, K. Van Laer, and A. Bogaerts, 'Streamer propagation in a packed bed plasma reactor for plasma catalysis applications', *Chemical Engineering Journal*, vol. 334, pp. 2467–2479, Feb. 2018, doi: 10.1016/j.cej.2017.11.139.

[14] T. C. Manley, 'The Electric Characteristics of the Ozonator Discharge', *Transactions of The Electrochemical Society*, vol. 84, no. 1, p. 83, 1943, doi: 10.1149/1.3071556.

[15] V. Goujard, J.-M. Tatibouët, and C. Batiot-Dupeyrat, 'Carbon Dioxide Reforming of Methane Using a Dielectric Barrier Discharge Reactor: Effect of Helium Dilution and Kinetic Model', *Plasma Chemistry and Plasma Processing*, vol. 31, no. 2, pp. 315–325, Apr. 2011, doi: 10.1007/s11090-010-9283-y.

[16] A. Fridman, *Plasma Chemistry*. Cambridge University Press, 2008. doi: 10.1017/CBO9780511546075.

[17] F. M. Penning, 'Die glimmentladung bei niedrigem druck zwischen koaxialen zylindern in einem axialen magnetfeld', *Physica*, vol. 3,

no. 9, pp. 873–894, Nov. 1936, doi: 10.1016/S0031-8914(36)80313-9.

[18] J. C. Whitehead, ‘Plasma–catalysis: the known knowns, the known unknowns and the unknown unknowns’, *J Phys D Appl Phys*, vol. 49, no. 24, p. 243001, Jun. 2016, doi: 10.1088/0022-3727/49/24/243001.

[19] M. Taheraslani and H. Gardeniers, ‘Coupling of CH_4 to C_2 Hydrocarbons in a Packed Bed DBD Plasma Reactor: The Effect of Dielectric Constant and Porosity of the Packing’, *Energies (Basel)*, vol. 13, no. 2, p. 468, Jan. 2020, doi: 10.3390/en13020468.

[20] F. J. J. Peeters and M. C. M. van de Sanden, ‘The influence of partial surface discharging on the electrical characterization of DBDs’, *Plasma Sources Sci Technol*, vol. 24, no. 1, p. 015016, Dec. 2014, doi: 10.1088/0963-0252/24/1/015016.

[21] X. Tu, H. J. Gallon, M. V Twigg, P. A. Gorry, and J. C. Whitehead, ‘Dry reforming of methane over a Ni/Al_2O_3 catalyst in a coaxial dielectric barrier discharge reactor’, *J Phys D Appl Phys*, vol. 44, no. 27, p. 274007, Jul. 2011, doi: 10.1088/0022-3727/44/27/274007.

[22] T. Butterworth, R. Elder, and R. Allen, ‘Effects of particle size on CO_2 reduction and discharge characteristics in a packed bed plasma reactor’, *Chemical Engineering Journal*, vol. 293, pp. 55–67, Jun. 2016, doi: 10.1016/j.cej.2016.02.047.

[23] X. Tu, H. J. Gallon, M. V. Twigg, P. A. Gorry, and J. C. Whitehead, ‘Dry reforming of methane over a Ni/Al_2O_3 catalyst in a coaxial dielectric barrier discharge reactor’, *J Phys D Appl Phys*, vol. 44, no. 27, Jul. 2011, doi: 10.1088/0022-3727/44/27/274007.

[24] N. García-Moncada, G. van Rooij, T. Cents, and L. Lefferts, ‘Catalyst-assisted DBD plasma for coupling of methane: Minimizing carbon-deposits by structured reactors’, *Catal Today*, vol. 369, pp. 210–220, Jun. 2021, doi: 10.1016/j.cattod.2020.04.028.

[25] K. Van Laer and A. Bogaerts, ‘Influence of Gap Size and Dielectric Constant of the Packing Material on the Plasma Behaviour in a Packed Bed DBD Reactor: A Fluid Modelling Study’, *Plasma Processes and Polymers*, vol. 14, no. 4–5, Apr. 2017, doi: 10.1002/ppap.201600129.

[26] S. Y. Liu, D. H. Mei, Z. Shen, and X. Tu, ‘Nonoxidative conversion of methane in a dielectric barrier discharge reactor: Prediction of reaction performance based on neural network model’, *Journal of Physical Chemistry C*, vol. 118, no. 20, pp. 10686–10693, May 2014, doi: 10.1021/jp502557s.

[27] Y. Yang, ‘Direct Non-oxidative Methane Conversion by Non-thermal Plasma: Modeling Study’, *Plasma Chemistry and Plasma Processing*, vol. 23, no. 2, pp. 327–346, 2003, doi: 10.1023/A:1022924220062.

[28] D. H. Lee, Y. H. Song, K. T. Kim, and J. O. Lee, ‘Comparative study of methane activation process by different plasma sources’, *Plasma Chemistry and Plasma Processing*, vol. 33, no. 4, pp. 647–661, Aug. 2013, doi: 10.1007/s11090-013-9456-6.

[29] J. Kim, J. Jeoung, J. Jeon, J. Kim. Y. S. Mok, and K.-S. Ha, ‘Effects of dielectric particles on non-oxidative coupling of methane in a dielectric barrier discharge plasma reactor’, *Chemical Engineering*

Journal, vol. 377, pp.: 119896, Dec. 2019, doi: 10.1016/j.cej.2018.09.057

[30] R. Liu, D. Zhan, D. Wang, C. Han, Q. Fu, H. Zhu, Z. Mao, and Z.-Q. Liu, 'Surface Plasmon Resonance Effect of Noble Metal (Ag and Au) Nanoparticles on $BiVO_4$ for Photoelectrochemical Water Splitting', *Inorganics*, vol. 11, no. 5, pp. 206, May 2023, doi: 10.3390/inorganics11050206.

[31] J. Lang, Y. Ma, X. Wu, Y. Jiang, and Y. H. Hu, 'Highly efficient light-driven methane coupling under ambient conditions based on an integrated design of a photocatalytic system', *Green Chemistry*, vol. 22, no. 14, pp. 4669–4675, 2020, doi: 10.1039/D0GC01608J.

[32] N. Li, R. Jiang, Y. Li, J. Zhou, Q. Ma, S. Shen, and M. Liu, 'Plasma-Assisted Photocatalysis of CH_4 and CO_2 into Ethylene', *ACS Sustain Chem Eng*, vol. 7, no. 13, pp. 11455–11463, Jul. 2019, doi: 10.1021/acssuschemeng.9b01284.

4.6 Annex

4.6.1 Materials

Ti gauzes 60 and 80 mesh, were purchased from Alfa Aesar. Commercial TiO_2 powder, $AgNO_3$, HCl, $HAuCl_4 \cdot 3H_2O$, were provided by Sigma-Aldrich.

4.6.2 Mathematical methods

- The residence time was calculated with the following formula:

$$\tau = \frac{V}{\tilde{V}}$$

$$V = \text{volume } (m^3)$$

$$\tilde{V} = \text{volumetric flow rate } (m^3 s^{-1})$$

- The discharge power in the tubular DBD reactor (paragraph 4.2) was calculated using the Q-V Lissajous method multiplying the area contained by the Lissajous figure, with the frequency of the applied voltage using the following formula:

$$P = f \cdot E$$

$$E = area\ contained\ by\ the\ Lissajous\ figure$$

$$f = frequency\ of\ the\ applied\ voltage\ signal$$

- The discharge power in Planar DBD reactor (paragraph 4.3) was calculated using the following formula:

$$P(W) = fpul \int_{Tpul} u \times i\, dt$$

- Knowing the plasma power and the gas flow rate in the reactor, the Specific Energy Input (SEI) was calculated, using the following formula:

$$SEI\ (Specific\ Energy\ Input)\ (J/mL) = \ Calculated\ Plasma\ Power\ /\ Gas\ flow\ rate$$

- The methane conversion and the selectivity towards the products are calculated using the following equations:

$$CH_4\ conversion = \frac{\{Input[CH_4] - Output[CH_4]\}}{\{Input[CH_4]\}} \times 100\ (\%)$$

$$H_2\ selectivity = \frac{\{Output\ [H_2]\}}{\{Input[CH_4] - Output\ [CH_4]\} \times 2} \times 100\ (\%)$$

$$C_2H_2\ selectivity = \frac{\{Output\ [C_2H_2]\} \times 2}{\{Input[CH_4] - Output\ [CH_4]\}} \times 100\ (\%)$$

$$C_2H_4\ selectivity = \frac{\{Output\ [C_2H_4]\} \times 2}{\{Input[CH_4] - Output\ [CH_4]\}} \times 100\ (\%)$$

$$C_2H_6\ selectivity = \frac{\{Output\ [C_2H_6]\} \times 2}{\{Input[CH_4] - Output\ [CH_4]\}} \times 100\ (\%)$$

$$C_3\ selectivity = \frac{\{Output\ [C_3]\} \times 3}{\{Input[CH_4] - Output\ [CH_4]\}} \times 100\ (\%)$$

$$Carbon\ balance\ (\%) =$$

$$\frac{\{Output\ [C_3]\ \times 3\} + \{Output\ [C_2H_4] \times 2\} + \{Output[C_2H_6]\ \times 2\} + \{Output[C_2H_2] \times 2\} + \{Output\ [CH_4]\}}{Input\ [CH_4]} \times 100$$

5. General conclusions

In this PhD thesis, novel photocatalysts based on a 3D hierarchical array of TiO_2 nanotubes on a Ti mesh as support (TiO_2NTs/Ti mesh), also modified with different metal nanoparticles, have been efficiently developed and studied in different catalytic processes for the activation of small molecules. This particular choice brought about the coupling of a hierarchy of porous systems, the mesoporous nanotubes and the macroporous mesh. These materials, serving as both electrodes and catalysts, were tested in photo-electrocatalytic reactions to produce hydrogen and valuable chemicals (water splitting and ethanol photo-conversion), as well as in plasma-assisted non-oxidative methane coupling to form hydrocarbons and hydrogen. The TiO_2NTs on Ti meshes were prepared by anodic oxidation procedure, a versatile method that allows the modulation of the morphology of the titania nanostructured film, changing properly the experimental conditions. The first part of this work was dedicated to the optimization of the synthesis parameters to maximize the photoactivity of the samples. The best results in terms of optical and photo-electrical properties were obtained with an anodization potential of 50 V maintained for 1 hour in an ethylene glycol-based electrolyte.

An extensive study was then performed to analyse the impact of the peculiar substrate geometry of the catalyst (titanium mesh or foil) on the photocatalytic performances in water photo-electrolysis reaction. For this purpose, electrochemical impedance spectroscopy (EIS), combined with other electrochemical techniques (CV and CA) under both dark and illuminated conditions, was successfully used. EIS is a useful methodology to evaluate charge transfer phenomena occurring at the interface of electrodes and electrolytes. It was observed a good correspondence between EIS and photocatalytic results in water splitting reaction, indicating that the structure of the support has a strong impact on the behaviour of the TiO_2 nanotubes array. The more complex

hierarchical macro/meso porous structure of the nanotubes in the mesh enhancing light absorption and facilitating faster electron transport along the nanotubes, significantly influenced the catalytic performance under illumination, increasing over three times the production of H_2 and the current density in water photo-electrolysis, in comparison with the foil substrate.

Then the effect of the modification of the TiO_2NTs/Ti mesh with metal with proven LSPR (localized surface plasmon resonance) behaviour was investigated. Au, Ag, Cu, and Pd nanoparticles were deposited on the TiO_2NTs/Ti mesh substrate, using photodeposition and electro-deposition methods, and the as-prepared samples, fully characterized, were tested in two different reactions: water photo-electrolysis and ethanol photo-dehydrogenation. The results obtained in water photo-electrolysis were very promising, as the metal-modified electrodes showed strong improvements in the performances compared to unmodified titanium dioxide substrate, thus confirming the role of NPs in the enhancement of photoactivity of titania. Specifically, by using Cu/TiO_2NTs/Ti sample, an increase in H_2 production of 85% but a 20% decrease in the photocurrent was observed, evidencing an indirect correlation between current and catalytic performances. A similar behaviour was noticed with Au/TiO_2NTs/Ti catalyst, even if much less pronounced. The H_2 production of the Ag/TiO_2NTs/Ti sample was more than three times higher compared to the bare TiO_2NTs/Ti mesh, showing also the highest current density, probably because of the presence of small particles in lower amounts (as evidenced by the SEM-EDX analysis). A general correlation between the amount of a co-catalyst and H_2 production has been observed, depending on the cocatalyst used.

Subsequently, experimental tests were aimed at understanding the role of the operating configuration of the photoreactor on the activity in the ethanol photo-dehydrogenation reaction. This process is very appealing from an industrial point of view, due to the possibility of obtaining, (together with H_2 at the cathode side) high-added-value products (such as aldehydes or organic acid) at the anode

instead of oxygen. This reaction is conventionally performed in the liquid phase but operating in the gas phase could offer instead several potential advantages (easy scale-up, minimization of scattering phenomena, no metal-leaching etc). Thus, TiO_2NTs/Ti mesh modified with metals were tested in the reaction of ethanol photo-conversion in two different cell configurations (liquid and gas phase) to investigate simultaneously two key factors: i) the role of metal nanoparticles on the anodic products selectivity and their action mechanism, and ii) the impact of the presence of an electrolyte on the selectivity and photoactivity. From the obtained results, it was possible to conclude that the adoption of liquid or gas phase conditions and the choice of metal nanoparticles had a strong impact on the catalytic behaviour, particularly in terms of selectivity, thus the presence of an electrolyte influenced the type and quantity of products formed at the anode. In fact, in the gas phase, by using Au modified sample, compared to Pd and Ag catalysts, no acetic acid formation was observed, in contrast with the liquid phase configuration. This behaviour was the opposite for Pd and Ag-modified samples that catalysed the subsequent reaction of oxidation of acetaldehyde to acetic acid. In conclusion, by varying the cell configuration, a distinct reaction pathway in ethanol photo-dehydrogenation and, consequently, different selectivity, was obtained and this adds an attractive dimension to this study for future applications.

The last part of the thesis investigated the effect of the 3D macro/meso nanostructure present in the TiO_2NTs on Ti mesh, in the reaction of plasma-assisted non-oxidative coupling of methane (NOCM) using two different plasma reactor configurations: a conventional cylindric DBD reactor and a novel planar DBD reactor. Both these configurations allowed the irradiation of the sample, to further test the effect of the combination between photo- and plasma catalysis. By using the conventional cylindric DBD plasma reactor, the presence of catalysts reduced the deposition of carbon on the reactor and strongly changed the selectivity. Among all the catalysts the TiO_2NTs/Ti 60 mesh showed the highest methane conversion, with a greater selectivity towards C_2H_6 and C3 products. The

presence of a metal, Ag in particular, allowed to push further the selectivity. Generally, the observed CH_4 conversion was essentially initiated by the plasma discharge and not by a specific catalytic effect of materials used as electrodes, differently from the product distribution. The effect of light was evident in observing the selectivity. Light irradiation affected modulation of the selectivity, in particular towards ethane, with an improvement with all the tested catalysts (TiO_2NTs/Ti mesh and metal-modified TiO_2NTs catalysts).

Then, the work was dedicated to the design of a new concept DBD planar reactor. Many adjustments had been necessary to ensure system inertness and prevent short circuits, assuring a good stabilization of plasma during the process. In the end, a very compact reactor with no gap between the dielectric material and the electrodes, equipped with a quartz window for illumination, was constructed to study the synergies between photocatalysis and localized microplasma. The TiO_2NTs/Ti mesh and metal-modified catalysts were tested using this DBD planar reactor in plasma-assisted NOCM reaction and, analysing the results obtained, it was evident the beneficial role of gold. The gold-modified sample in fact, strongly enhanced the methane conversion that reached a value of almost 43%, with a modulation also in the selectivity, pushing towards the ethylene production and this effect was even more marked under light irradiation. The influence of the light is thus very dependent on the geometry of the reactor. This process is a rather complex reaction, and many different parameters influence the mechanism, particularly if photo- and plasma-catalytic effects are combined. In conclusion, the use of a porous meso/macro 3D hierarchical structure, as the titanium dioxide nanotubes on a titanium mesh, was beneficial in terms of both conversion and selectivity, and the integration of metal plasmonic NPs could further enhance the performances.

List of the activities carried out

Research period abroad

At the TU/e (Eindhoven University of Technology), in Eindhoven (NL), from 01/02/2022 to 31/07/2022, in the Sustainable Process Engineering research group of Prof. Fausto Gallucci and the supervision of Dr. Sirui Li. The research was focused on the non-oxidative coupling of methane in a tubular DBD plasma reactor.

Attended webinar/workshop

- Oral presentation at ERC Synergy SCOPE online meeting - “Initial developments to set-up a new membrane reactor for plasma-photocatalysis”, 18/02/21
- ERC Synergy SCOPE online meeting, 18/03/21
- ERC Synergy SCOPE online meeting, 06/07/21
- ERC Synergy SCOPE online meeting, 31/08/21
- Webinar “Horizon Europe: scenario e prospettive del nuovo programma europeo per la ricerca e l'innovazione”, 25/02/21
- Panel discussion COST ACTIONS - Operational Issues, 16/04/21
- SunCOChem Project Webinar conference on "Photocatalytic synthesis for a carbon-neutral production of fuels and chemicals", 28/04/21
- Webinar “Towards Zero Pollution in the Production of Green Fuels and Chemicals”, 04/06/21
- Laboratorio Partecipativo “La tutela dell’ambiente per il futuro dell’Europa” virtual event, 15/06/21
- A-leaf 54M meeting, 30/06/21
- 3rd Course - International School of Water and Water Systems in “Advances in Functional Materials: Fundamentals, Technology and Sustainable Energy Production” virtual event, 06-07/07/21
- 3° Workshop on Innovative materials for Energy, 30/09/21 – 01/10/21
- Solvay Workshop on "Plasma Technology and Other Green Methods for Nitrogen Fixation", 15-17/11/2021
- Casale mini symposium, 16/11/2021

- Casale mini symposium, 24/11/2021
- Corso di formazione in materia di salute e sicurezza sui luoghi di lavoro – art. 37 del DLgs 81/08 e s.m.i., 21/02/2022,
- eCCU³ Workshop, 30/03/2022
- SOLAR2CHEM X SEAFUEL Symposium, 01/04/2022 online
- NMR course, 09-10-12/05/2022, TU/e, Eindhoven (Netherland)
- Radiation Protection Training Analytical x-ray equipment, 10/05/22, TU/e, Eindhoven.
- Mini Symposium Chemical Engineering and Chemistry with Klavs Jensen, 11/05/2022, TU/e, Eindhoven (Netherland)
- SunCoChem Towards the implementation of the EU Green Deal through the production of sustainable fuels and chemicals, 31/05/2022 online
- Seminar: "Brevetti per invenzioni industriali: strumenti per la tutela delle invenzioni nascenti dalla ricerca universitaria" Dr. Paolo Patanè U. OP. Tutela proprietà Industriale, 07/06/2022, University of Messina (Italy)
- Oral presentation at SCOPE project annual meeting, "Plasma-assisted catalytic coupling of methane". 23/09/2022- Leamington Spa, (the UK)
- Oral presentation in SCOPE project annual meeting, "TiO_2 nanotubes-based electrodes for plasma-assisted catalytic coupling of methane", 23/09/2022, Antwerp, (Belgium).

Papers (in ISI Web of Science/Scopus)

Luana De Pasquale, Francesco Tavella, Victor Longo, Marco Favaro, Siglinda Perathoner, Gabriele Centi, Claudio Ampelli, Chiara Genovese. The Role of Substrate Surface Geometry in the Photo-Electrochemical Behaviour of Supported TiO_2 Nanotube Arrays: A Study Using Electrochemical Impedance Spectroscopy (EIS), *Molecules* 2023, 28 (issue 8), 3378; Published: 11 April 2023 https://doi.org/10.3390/molecules28083378 gold open access

To be submitted

Luana De Pasquale, Francesco Tavella, Siglinda Perathoner, Gabriele Centi, Claudio Ampelli, Chiara Genovese. 3D-type meso/macro porous structured

photoanodes based on Ti mesh doped with metal nanoparticles: a comparison between gas and liquid-phase in ethanol upgrading process.

Victor Longo, **Luana De Pasquale**, Siglinda Perathoner, Gabriele Centi, Claudio Ampelli, Chiara Genovese . Efficient solar driven non oxidative coupling of methane to ethane over Pd decorated TiO_2 nanomembranes in a continuous flow reactor.

Abstracts in national and international conferences

Francesco Tavella, Daniele Giusi, Matteo Miceli, **Luana De Pasquale**, Veronica Costantino, Angela Mercedes. Ronsisvalle, Chiara Genovese, Siglinda Perathoner, Gabriele Centi, Claudio Ampelli. Cell and Electrode Engineering in Green H_2 Production via Photo-Electro-Catalytic (PEC) Approach, *International Symposium on Chemical Reaction Engineering 2024* (ISCRE 28), Turku/Åbo (Finland), 16-19 June 2024, submitted for oral presentation.

Luana De Pasquale, Victor Longo, Lavanya Veerapuram, Siglinda Perathoner, Gabriele Centi, Chiara Genovese. Synergistic effect of a non-thermal plasma–catalysis system on methane activation *8th International Congress on Catalysis (ICC 2024)*, Lyon (France) July 14-19, 2024, submitted for oral presentation.

Victor Longo, **Luana De Pasquale**, Claudio Ampelli, Siglinda Perathoner, Gabriele Centi, Chiara Genovese. Efficient solar-driven non-oxidative coupling of methane to ethane over Pd decorated TiO_2 nanomembranes *8th International Congress on Catalysis (ICC2024)*, Lyon (France) July 14-19, 2024, submitted for oral presentation.

.

Victor Longo, **Luana De Pasquale**, Claudio Ampelli, Siglinda Perathoner, Gabriele Centi, Chiara Genovese. Highly- effective metal-decorated TiO_2 based catalysts for photocatalytic methane coupling in a novel flow reactor. *Jahrestreffen Deutscher Katalytiker* March 13. – 15, 2024 Weimar (Germany) accepted as oral presentation

Victor Longo, **Luana De Pasquale**, Francesco Tavella, Siglinda Perathoner, Gabriele Centi, Claudio Ampelli, Chiara Genovese. Role of metal nanoparticles in non-oxidative methane coupling to ethane using a novel gas flow-through

photocatalytic reactor. *15th European Congress on Catalysis (EuropaCat2023)*, August 28 - September 2, 2023 Prague (rep. Czech) Book of Abstract 340

Victor Longo, **Luana De Pasquale**, Siglinda Perathoner, Gabriele Centi, Chiara Genovese. A new Plasma-assisted Catalytic Reactor for coupling of methane. *UCRA2022 – International Conference on Unconventional Catalysis, Reactors and Applications,* Leamington Spa, (the UK) September 21-23, 2022, Book of Abstract

Attendance in national and international conferences/schools

1) "Functionalization of TiO_2 nanotubes-based electrodes with metal nanoparticles to improve the catalytic performances in small molecules conversion", Scuola di Chimica Industriale 2023, Turin (Italy) 28/05/2023 – 01/06/2023, Oral presentation
2) "A new Plasma-assisted Catalytic Reactor for coupling of methane. UCRA2022 – International Conference on Unconventional Catalysis, Reactors and Applications", Leamington Spa, (the UK), September 21-23, 2022, poster presentation

Acknowledgements

I want to thank Prof. Gabriele Centi, my tutor, and Prof. Siglinda Perathoner for giving me the opportunity to work in their research group for the past three years. My gratitude goes to my tutor Prof. Chiara Genovese for all the support and guidance she gave me in this research period and to Prof. Claudio Ampelli for his help. I thank all my colleagues of the Messina research group, for the support, help and laughs we shared in these years. I'm grateful to Prof. Fausto Gallucci, Dr. Sirui Li, and all the people of the SPE research group for their hospitality in TU/e. I thank my boyfriend Marco, my family, my friends, all the friends from UMANA and my friends from the O'Sheas group for always having my back and every experience we shared in these years.